Reply to Reviewer Report 1

In the following the comments of the reviewer are presented (black) alongside with our replies (in blue) and changes made to the manuscript (in red).

General statement: The authors present an analysis of net O3 production calculated from ship-borne trace gas measurements obtained during the AQABA campaign, mostly in July and August 2017. In the Oman Gulf, the Northern Red Sea, and the Arabian Gulf the authors found the highest values ranging from 14 ppb day-1 to 28 ppb day-1. Based on HCHO/NO2 ratios, in most areas O3 formation was NOx limited apart from the Northern Red Sea, which was located in the VOC-NOx limitation transition zone. The Arabian Sea and Arabian Gulf areas showed maximum HCHO/NO2 values, clearly indicating NOx limitation. This paper shows some interesting data from an area, which often lacks robust air quality data, but which is also an area with significant (and increasing) anthropogenic emissions, mostly related to oil and gas exploration. The paper is well-written and deserves publication. However, I was hoping the authors could address some of my concerns.

Dear reviewer, thank you very much for reviewing our manuscript and for the insightful comments. Below we provide detailed responses to your comments. Please find revised graphs at the end of the document, which were compiled based on your comments.

Comment 1: Page 1 L22-24: According to Fig 10 net O3 formation actually mostly occurs in NOx limitation regimes, not in the transition regime, as the authors mention here. Also, it seems Fig 10 does not support the findings by Pfannerstill et al. (2019) as stated by the authors on page 25 (L509-511). All, but one median, is above the threshold of HCHO/NO2 > 2. I also doubt that a HCHO/NO2 median of 2.2 (for OG) would signify a tendency towards VOC limitation (L511-512).

Indeed a median HCHO/NO_2-ratio of 2.2 does not fall within plain VOC limitation as deduced by Duncan et al. (2010), which needs to be re-written. Although Pfannerstill et al. (2019) highlight the scatter in the attribution of ozone production to NO_x- and VOC-limitation, their study shows that ozone production over the Arabian Sea over the Arabian Gulf is rather NO_x-limited, whereas the Gulf of Suez is characterized by a strong VOC-limitation (page 11516 and page 11517, Figure 9 [Pfannerstill et al., 2019]). We have revised Page 1 L21-24 to: Constrained by HCHO/NO_2-ratios, our photochemistry calculations show that net ozone production in the MBL around the Arabian Peninsula occurs mostly in NO_x-limitation regimes with a significant share of ozone production occurring in the tranisition regime between NO_x- and VOC-limitation over the Mediterranean and more significantly over the Northern Red Sea and Oman Gulf.

Comment 2: Page 3, L58-59: The reference Zhou et al (2014) shows up a couple of times in this paper. While I agree that it makes sense to compare the authors' Middle East study area with the Houston area (e.g. some similar emissions; similar latitude) there are better publications for the Houston case which include direct measurements of OH, HO2, and also O3 production itself among many other measurements (e.g. Chen et al., 2010; Mao et al, 2010; Ren et al. 2013).Also, I doubt that the term marine environment shows up in Zhou et al.

We have removed the term "marine environment" in the context of Zhou et al. (2014) and we have revised the manuscript as suggested on Page 2, L55-56 to: Measurements performed in the Houston Ship Channel revealed NOPR of the order of several tens of ppb h^{-1} (Chen et al., 2010; Mao et al., 2010; Ren et al., 2013).

Comment 3: Page 3, L80-86: This explanation is confusing. It seems there is a main sampling inlet (not sure what instruments were connected), but for HCHO and NOx sampling was done via a 1/2" PFA tubing (not sure how long the tube was), and for the other trace gas measurements (what were those?) it was done in a different way. May be a chart showing the experimental design would be helpful.

Please note that air was drawn from the stainless steel common inlet into each measurement container via bypass systems. NO_x (CLD measurements) and HCHO measurements were located in one lab container (both sampling air from the same bypass) and NO_2 (CRDS measurements) and O_3 in another lab container. We have revised Page 3, L78-84 to: A 6 m high, 20 cm diameter cylindrical stainless steel common inlet was installed on the front deck of the vessel to sample air at a total mass flow rate of 10,000 SLM. NO and NO_2 chemiluminescence measurements were obtained at a total bypass flow rate of 28.5 SLM sampling air from the common inlet with a residence time in the tubing of ~3 s. HCHO, NO_2 cavity ring-down spectroscopy and O_3 measurements were obtained with similar bypass systems sampling air from the common inlet. H_2O vapor was measured on the top of the ship mast in the front.

Comment 4: Page 6, L144: What was the flow of the calibration gas into the zero air?
The NO calibration flow into the zero air was 4.5 sccm. We have revised the manuscript. Now it says on Page 6, L 140-142: Zero air measurements and NO calibrations were performed with a total mass flow of 3.44 SLM achieving an overflow of 0.44 SLM to guarantee ambient air free standard measurements. The calibration gas was added at 4.5 sccm to the zero air flow.

Comment 5: Page 6, L157: What do the authors mean by "notably high"?
Alkenes can react with ozone to produce a chemiluminescent signal which will bias NO measurement obtained by chemiluminescence. To subtract such interferences, the CLD has been equipped with a prechamber to which the sampled air can be directed during prechamber measurements. As the reaction of ozone with alkenes will be much slower than the reaction of NO and with ozone, the CLD will be measuring only the signal from the reaction of alkenes during prechamber measurements. It should be noted that the signal from the reaction of alkenes with ozone observed during a prechamber measurement will also slightly decrease. Regions where alkenes are strongly varying in time and magnitude might be plagued by a measurement offset. We have revised Page 6, L148-150: However, in regions where alkene concentrations are strongly varying in time and magnitude, the CLD is prone to enhanced backgrounds due to the interference of alkenes with ozone in the instrument.

Comment 6: Page 11, L259: I guess the authors mean Lu et al. (2010) here.
Thank you very much for noticing this typo. Now it says Lu et al. (2010) instead of Lu et al. (2016) on page 11, L260.

Comment 7: Page 12, L276-277: The loss mechanism through H2O is important. Also, it seems to vary a lot. Some parts of the ship cruising legs might have already been exposed high humidity due to the Indian monsoon system. It would be good to see the absolute humidity variation along the legs similar to Figs 3 and S4.
Figures showing the absolute variation along both legs have been added to the supplement. On P13 L328 now it says: Supplementary Figure S5 shows the variation of the absolute humidity around the Arabian Peninsula.

Comment 8: Page 12, L281-282: At least, the authors want to include an estimate for the potential contribution of halogens.
Based on oxidative pairs, Bourtsoukidis et al. found that the majority of the samples they collected during AQABA were characterized by a OH/Cl-ratio of ~ 200:1 (Bourtsoukidis et al., 2019, Non-methane hydrocarbon (C_2-C_8) sources and sinks around the Arabian Peninsula, doi:10.5194/acp-19-7209-2019). Measured daytime OH concentrations were of the order of $5 \cdot 10^6$ molec cm^{-3}, hence the Cl radical concentration can be estimated at $2.5 \cdot 10^4$ molec cm^{-3}. Incorporating an ozone loss due to the reaction of O_3 with Cl (at Cl concentrations of $2.5 \cdot 10^4$ molec cm^{-3}) into the NOPR (Eq. 7) would decrease the diurnal net ozone production rates by roughly 0.2

ppb_v day^{-1} over the Arabian Sea and at most 0.6 ppb_v day^{-1} over the other regions. We have revised the manuscript as follows on page 12, L285-289: Based on oxidative pairs, Bourtsoukidis et al. (2019) have classified the majority of their samples collected during AQABA by an OH/Cl-ratio of 200:1. As measured daytime OH concentrations were of the order of $5 \cdot 10^6$ molecule cm^{-3}, the estimate would yield a Cl concentration of $2.5 \cdot 10^4$ molecule cm^{-3}, which would decrease the estimated diurnal net ozone production rates by roughly 0.2 ppb_v day^{-1} over the Arabian Sea and at most 0.6 ppb_v day^{-1} over the other regions, which does not substantially alter the here presented findings. The noontime chemical ozone loss rate can be summarized by

Comment 9: Page 12, Eq. 7 and Fig 9: It would be nice to see a break-down of the different terms in Eq. 7 for different legs as shown in Fig. 9 to evaluate what processes might be most relevant/different in those different legs.

We have included regional box-whisker plots (according to Figure 9) of the four terms of Eq. 7 in the supplements. We have revised the manuscript on Page 21, L460-461: A break-down of the different terms of Eq. 7 in the six regions is included in the supplementary Figures S10 – S13.

Comment 10: Page 13, L310: Authors mention NOx values of several hundred ppbs. Where do they show up in Figs. 3, S2, and S3? What were the megacities along the cruising legs? I could think about Cairo, but according to Fig 3 NOx values do not show extremely high values.

Values of up to several hundred of ppb_v NO_x were observed when measuring own ship stack, stack of bypassing ships or when being at anchor in the direct vicinity of Jeddah or Kuwait City. Data measured during these time periods have been removed from the final data set as contamination by the ship exhaust itself could not be excluded for these period. Megacities along the cruising legs generally include Cairo, Kuwait City, megacities in the UAE and Jeddah (Saudi Arabia).

Comment 11: Page 13, L311-312: During the first leg very high O3 values are found in the Arabian Gulf and potentially in the area of the Suez Canal. In the second leg those high O3 values are pretty much gone. I doubt emissions have changed. I also doubt that weather conditions have changed drastically. What were the reasons for those distinct changes?

Based on back trajectories, previous studies (Pfannerstill et al., 2019) also already highlighted different air mass origins during the two legs for the air sampled e.g. over the Arabian Gulf. While during the first leg northwestern wind from Kuwait/Iraq was encountered, northeastern winds from Iran were encountered during the second leg over the Arabian Gulf. For the area of Suez, data coverage during the first leg (due to instrumental mal function and applied stack filter) is not as exhaustive as during the second leg. We would classify these changes of concentrations in the Suez region as insignificant (see also Figure S2 and the data coverage for the Suez region before July 06th 2017). We have revised the manuscript on Page 16, L351-355 as follows: However, a significantly larger whisker-interval of observed ozone of 31.4 ppb_v over the Gulf of Oman indicates increasing amounts of pollution and advection from the Arabian Gulf where extreme events of ozone were observed several times during the campaign with maximum mixing ratios of up to 170 ppb_v when wind was coming from Kuwait/Iraq. Please note that during the second leg wind was coming from Iran (Pfannerstill et al., 2019).

Comment 12: Page 16, L334-355: This section should include some more explanations: it seems there is a huge variation in NOx and O3 in AG (also a huge variation in NOPR as shown in Fig 9). What is the major driver of this: point sources from ships? Why are the highest NOx values in OG and why are some of the lowest O3 values found in OG? Why would you consider air masses over the Mediterranean as photochemically aged air masses due to the small whisker-interval, while the whisker-plots for AS and OG show pretty much the same with, but at much lower absolute O3 ranges. There are no emission sources in that area of the Mediterranean?

Reasons for large variations of NO_x and O_3 over the AG are point sources (ship, oil and gas processing) as well as a change in the general wind direction observed during both legs. NO_x are high over the OG due to the magnitude of emissions from vessels. O_3 is generally very low over the OG because it has been partly characterized as VOC-limited and high NO_x values may contribute to net ozone destruction. Air over the Mediterranean has previously been characterized as photochemically processed emissions from Eastern Europe (Turkey, Greece) (Destroff et al., 2017; Pfannerstill et al., 2019). We have included Destroff et al., "Volatile organic compounds (VOCs) in photochemically aged air from the eastern and western Mediterranean, 2017, doi:10.5194/acp-17-9547-2017 as a reference. Page 16, L348-364 following now say (please note that only the underlined sentences have been changed): **The low O_3 mixing ratios over the Arabian Sea was accompanied by the smallest variability (whisker-interval: 15.1 ppb_v). Although observing highest NO_x over the Oman Gulf, O_3 observed over the Oman Gulf was amongst the lowest detected throughout the whole campaign, which can be partly explained by the fact that high NO_x lead to low ozone production or even net ozone destruction. However, a significantly larger whisker-interval of observed ozone of 31.4 ppb_v over the Gulf of Oman indicates increasing amounts of pollution and advection from the Arabian Gulf where extreme events of ozone were observed several times during the campaign with maximum mixing ratios of up to 170 ppb_v when wind was coming from Kuwait/Iraq. Please note that during the second leg wind was coming from Iran (Pfannerstill et al., 2019).** The whisker-interval over the Arabian Gulf was 100.9 ppb_v, more than six times higher than that over the Arabian Sea. **Reasons for large variations of both NO_x and O_3 over the Arabian Gulf were a multitude of point sources as well as a change in the observed wind direction with air masses coming from Iraq/Kuwait area during the first leg and air masses coming from Iran during the second leg (Pfannerstill et al., 2019).** Over the Mediterranean, the Northern Red Sea and the Southern Red Sea, median ozone was 61.5 ppb_v, 64.2 ppb_v and 46.9 ppb_v, respectively. The whisker-interval over the Northern Red Sea and the Southern Red Sea were 44.2 ppb_v and 31.6 ppb_v, respectively. **Air masses over the Mediterranean were characterized as photochemically aged due to their impact by northerly winds (Etesians) which bring processed/oxidated air from eastern Europe (Turkey, Greece) to the Mediterranean area (Derstroff et al., 2017; Pfannerstill et al., 2019). This photochemical ageing/oxidation over the Mediterranean leads to a rather small whisker-interval of 18.7 ppb_v in ozone.**

Comment 13: Page 17, L367: As I understand it Velchev et al. (2011) show O3 data from the Western Mediterranean. A reference looking closer to the area the authors studied would be Kouvarakis et al (2002).
We have now replaced (Velchev et al., 2011) by (Kouvarakis et al., 2002) on page 17, L382.

Comment 14: Page 17, L369: Edwards et al. (2014) is not a good reference here. Edwards et al report wintertime O3 in cold-pool conditions, i.e. extremely low boundary layer heights. The meteorological conditions reported in Edwards et al are pretty different from the ones observed in the Middle East during summertime. Also, there is no word on the impact of narrow shipping lanes in Kleinman et al (2005) and Zhou et al (2014). O3 in Houston is predominantly driven by emissions from all kinds of petrochemical industries (including refineries, but no oil exploration) located in the Ship Channel area.
We agree that Edwards et al., 2014 is not the best reference in here, which has been removed in this context. Also Kleinman et al. (2005) and Zhou et al. (2014) have been removed in the context of shipping lanes. Instead we have included Mazzuca et al., 2016 "Ozone production and its sensitivity to NO_x and VOCs: results from the DISCOVER-AQ field experiment, Houston 2013", doi:10.5194/acp-16-14463-2016. On page 17, L382-384 now it says: The latter are consistent with O_3 mixing ratios reported from regions influenced by oil and gas processing (Pfannerstill et al., 2019) and shipping lanes such as the Houston Ship Channel (Mazzuca et al., 2016).

Comment 15: Page 25, L516-517: Actually, Figure 10 shows that in almost all areas O3 formation is NOx limited. However, the authors say that this is typical for photochemically aged air masses over the Mediterranean. As

already mentioned further above, why do the authors explicitly consider the Mediterranean area having aged air masses? It is even more surprising as the results for the Mediterranean area in Figure 10 indicate that the Box-Whisker plot stretches into the transition between NOx and VOC limitation.

The Mediterranean area is considered having aged air masses as it is impacted by processed emissions from eastern Europe (Destroff et al., 2017; Pfannerstill et al., 2019). We have removed the statement that photochemical ageing of air masses over the Mediterranean leads to NO_x-limitation, however it should be noted that on 29 August 2017 we were lying at anchor in front of Malta with a magnitude of pollution sources nearby. This day is characterized by a low $HCHO/NO_2$-ratio and explains why the Box-Whisker-Plot for the Mediterranean stretches into the transition between NOx- and VOC-limitation. Page 25, L534-538 now says: Ozone production over the Mediterranean was classified as rather NO_x-limited, however partly being in the transition regime between NO_x- and VOC-limitation, which can be explained by measurements obtained on 29 August 2017 when laying at anchor in front of Malta with a multitude of (NO_x)-emissions from nearby situated vessels. Average noontime NO_x on that particular day was about three times as large as the regional average noontime NO_x observed over the whole Mediterranean area.

Comment 16: Page 25. L517-519: Why would higher NOx lead to higher O3 pollution? For instance, according to Figure 4, OG has the highest NOx values, but also pretty low O3 values. With regard to NOPR, the Box-Whisker plot for OG shows positive, but also large negative values. In any case NOPR values are significantly lower than for AG, for instance.

Indeed, the passage needs more characterization. We have re-written the passage. Now it says on P25 L539-544: Note that a further increase in NO_x-emissions from increased shipping in the Arabian Gulf may initially lead to higher ozone production. However, a further increase in NO_x might eventually lead to a change from NO_x- to VOC-sensitivity and a decrease in ozone production for this region, as observed for the Oman Gulf (median $HCHO/NO_2$-ratio of 2.2 and average O_3 of 34 ppb_v). See supplementary Table ST9 for detailed statistics on regional $HCHO/NO_2$-ratios.

Comment 17: Table 1: This table can go into the supplement.

We have moved the table into the supplement and numbered the tables in the manuscript and supplement accordingly. In the manuscript (Line 99-101) now it says: See supplementary Table ST1 for the range of latitudinal and longitudinal coordinates of the different regions and supplementary Table ST2 for a detailed day to day description of the route.

Comment 18: Figure 7: The legend mentions "Measurements", the figure captions says "estimated". From Eq 3 I understand that RO2 was neither measured nor estimated, but calculated. Also, what would be the interpretation of the negative RO2 concentrations (blue Box- Whisker plots) when calculated from Eq 3?

The legends (Figure 7) now says Estimated based on measured data and EMAC. Also the legend for Figure 9 now says Estimated based on measured data and Estimated based on simulated data.

Comment 19: Figures S2 and S3: It would be nice to see the time series of OH and HO2 here as well.

We have added the time series of OH and preliminary HO_2 to Figures S2 and S3.

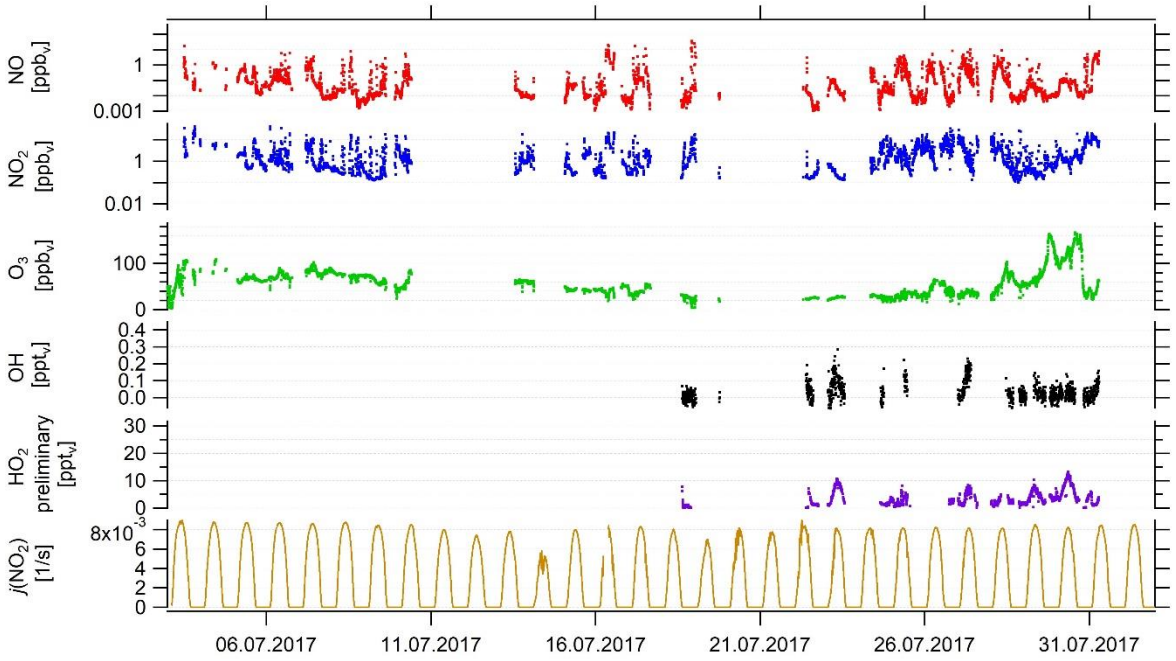

Figure S2: Timeline of NO, NO_2 (both CLD), O_3, OH, HO_2 preliminary and $j(NO_2)$ data during the first leg. See Table ST1 for additional information on the ship cruise. Note that HO_2 data are preliminary.

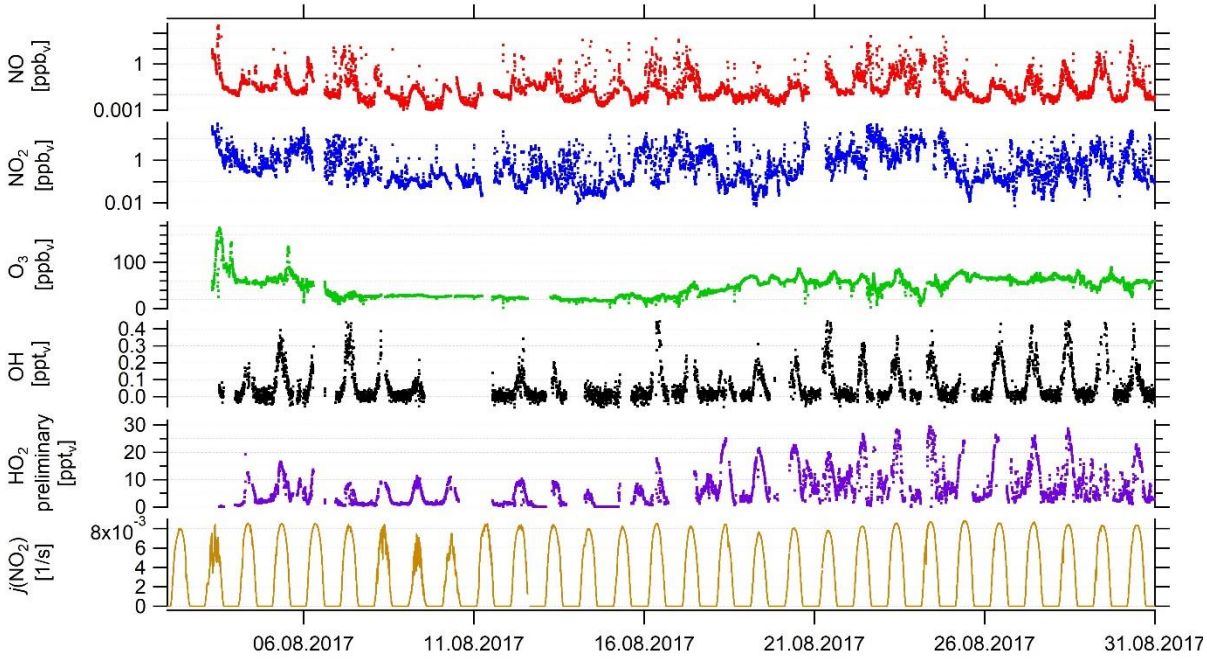

245

Figure S3: Timeline of NO, NO_2 (both CLD), O_3, OH, HO_2 preliminary and $j(NO_2)$ data during the second leg. See Table ST1 for additional information on the ship cruise. Note that HO_2 data are preliminary.

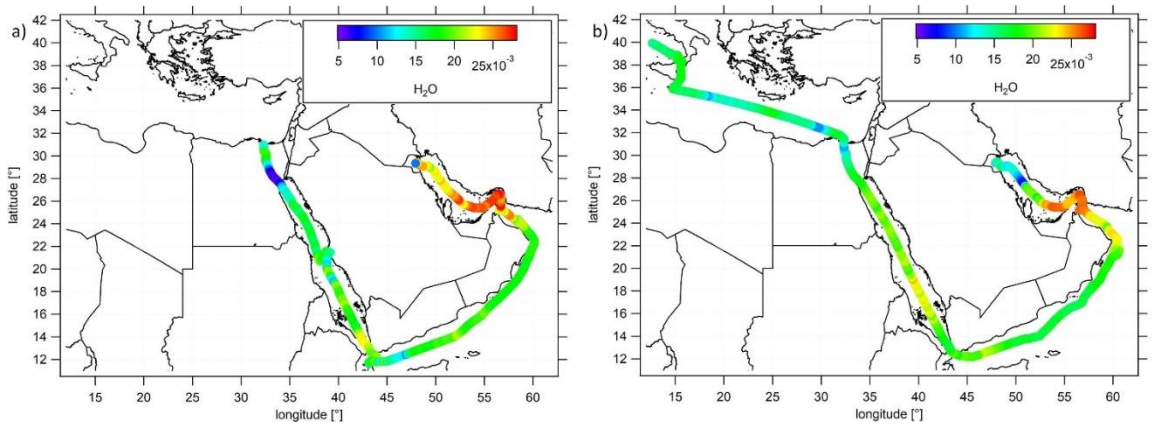

Figure S5: Ship cruises with color-scaled absolute humidity a) during the first and b) the second leg.

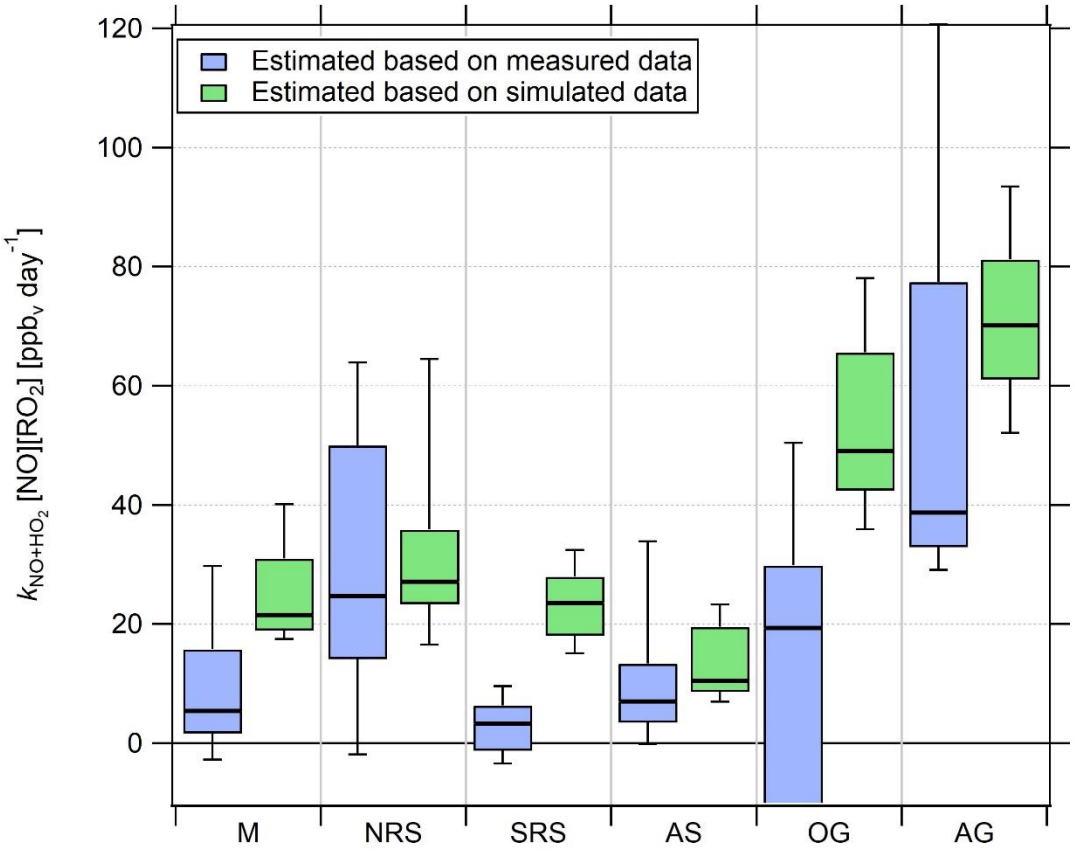

Figure S10: Comparison of the regional, absolute contribution of $k_{NO+HO_2}[NO][RO_2]$ to NOPR in the six different regions investigated during AQABA. The horizontal black bar indicates the median value, the box the 25- and 75-percentiles and the whiskers the 10- and 90-percentiles.

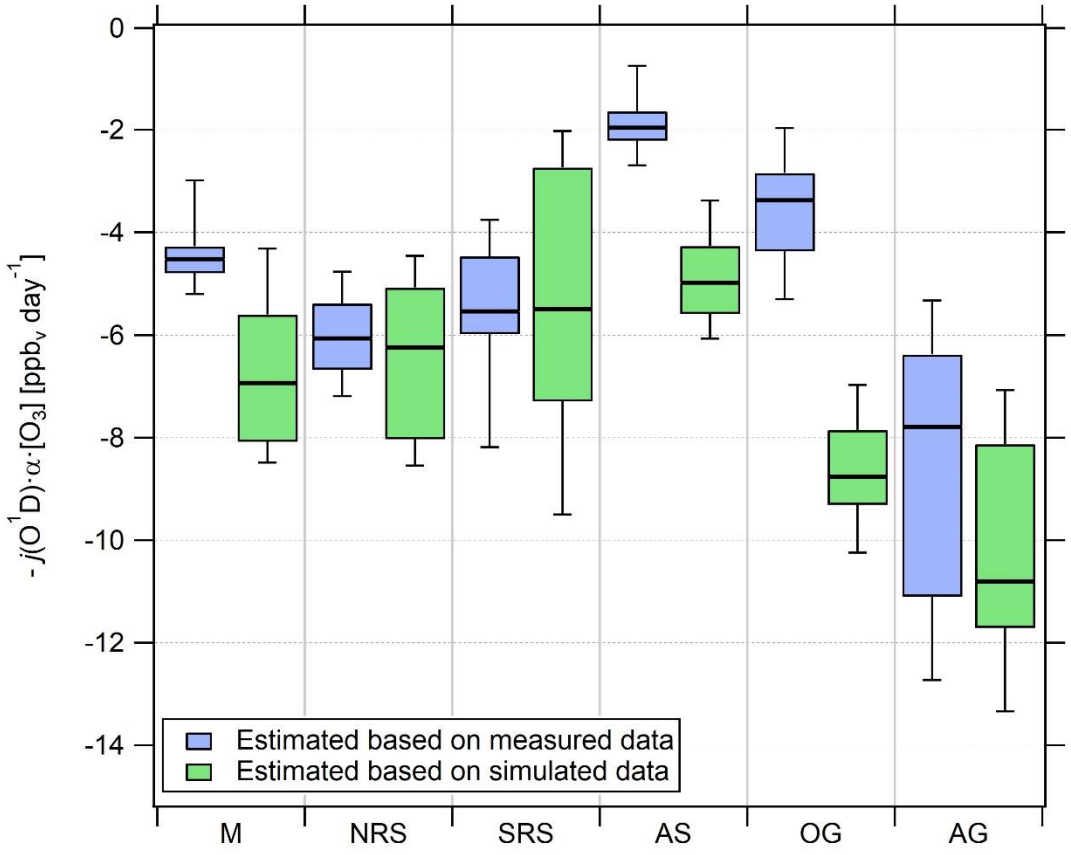

Figure S11: Comparison of the regional, absolute contribution of $-j(O^1D) \cdot \alpha \cdot [O_3]$ to NOPR in the six different regions investigated during AQABA. The horizontal black bar indicates the median value, the box the 25- and 75-percentiles and the whiskers the 10- and 90-percentiles.

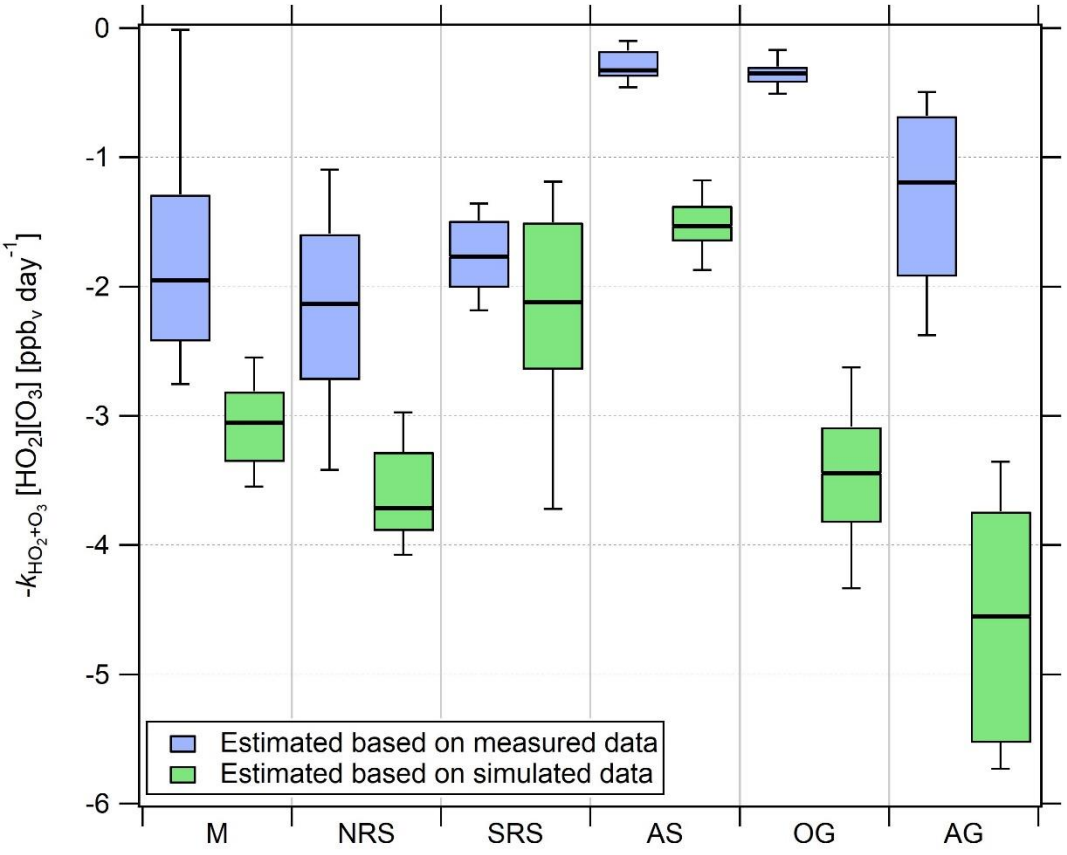

Figure S12: Comparison of the regional, absolute contribution of $-k_{HO_2+O_3}[HO_2][O_3]$ to NOPR in the six different regions investigated during AQABA. The horizontal black bar indicates the median value, the box the 25- and 75-percentiles and the whiskers the 10- and 90-percentiles.

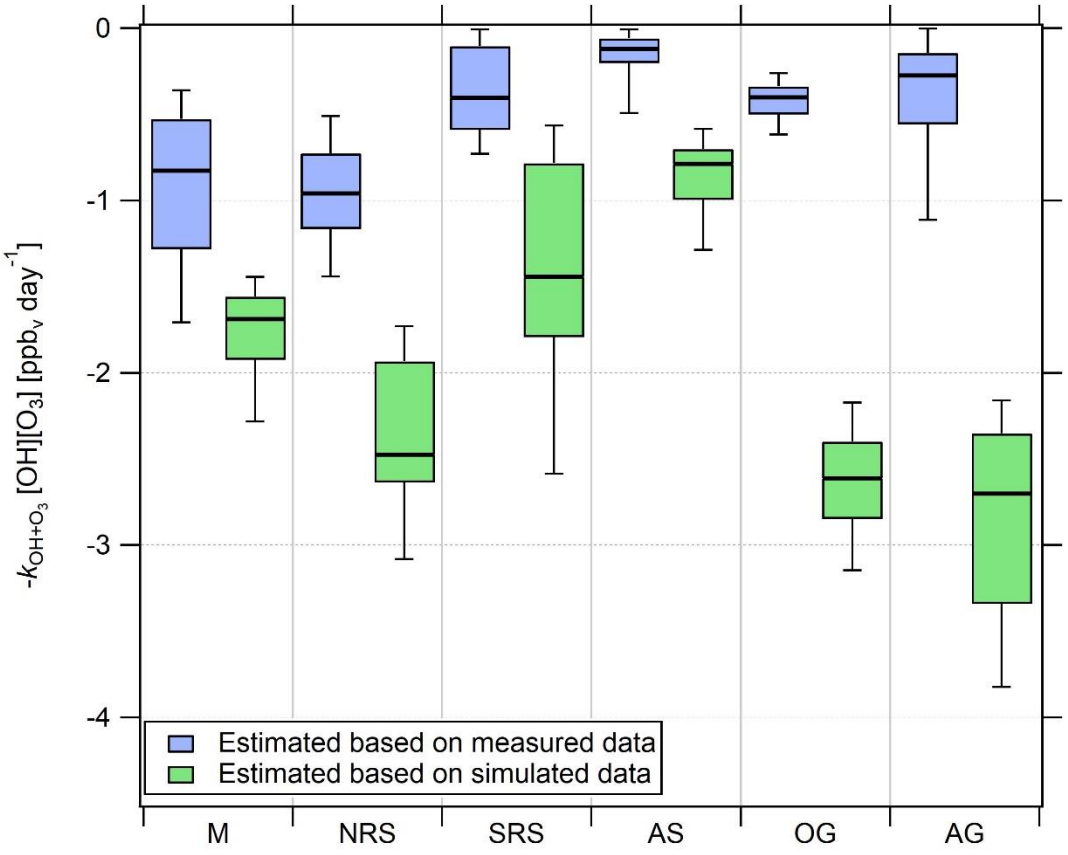

Figure S13: Comparison of the regional, absolute contribution of $-k_{OH+O_3}[OH][O_3]$ to NOPR in the six different regions investigated during AQABA. The horizontal black bar indicates the median value, the box the 25- and 75-percentiles and the whiskers the 10- and 90-percentiles.

Reply to Reviewer Report 2

In the following the comments of the reviewer are presented (black) alongside with our replies (in blue) and changes made to the manuscript (in red).

General statement: The authors have a very interesting data set. I'm not familiar with the chemistry of this region but I assume there are few high quality NOx measurements and perhaps no radical measurements. Analysis is through the use of deviations from the Leighton
photostationary state to get peroxy radical concentrations which are then used in conjunction
with measured NO to obtain ozone production rates. Observed OH and HO2 are presented only via a color-coded ship track. As far as I can tell, the only use of the observed OH and HO2 is to determine loss rates of ozone which when added to the PSS ozone production rate yields a net ozone production rate. The ratio of HCHO to NOx (both observed quantities) is used as an indicator ratio to predict regions in which O3 production is either NOx or VOC sensitive.

Comparisons are made with a Eulerian model for NOx, ozone, and RO2 mixing ratios as well as for net O3 production rate. This article contains the quantum of information to warrant publication. I can only guess that either they want to write up the radical and HCHO measurements in a separate study or that they are uninterruptable for one reason or another.

I found the article difficult to follow in places. It is my belief that the authors have underestimated the uncertainty of the instruments used to determine peroxy radicals. The authors need to re-examine their error propagation formula. I am calling this a major revision as it affects the most prominent results in the paper. In practice it can be done in an afternoon. They could also compare the PSS value of RO2 with measured HO2 (which is stated to be preliminary due to an up to 20% interference by RO2). This is a reality test.

Dear reviewer, thank you very much for reviewing our manuscript and for the insightful comments. Below we provide detailed responses to your comments. Please note that PSS RO_2 has been compared to HO_2 in Sect. 3.2, P 21 L442.

Comment 1: line 124 "UV-induced positive bias in the NO2 measurements due to photolysis of HONO, BrONO2, NO3 and ClNO2 to produce NO was characterized ahead of the campaign to be 7.7 %, 7.2 %, 5.6 % and 1.5 % of the respective ambient concentration of HONO, BrONO2, NO3 and ClNO2 respectively,"
(Italics mine). No where in the paper is it mentioned that these species are measured. Have interferences been determined based on model-calculated or typical concentrations? Or do these figures represent the percent interference if the interferent has the same concentration as NO?

We have used absorption cross sections from the MPI-Mainz UV/VIS Spectral Atlas of Gaseous Molecules (Keller-Rudek et al., 2013) for the estimation of the parallel interference. The particular photolysis rate of NO_2 and the regarded NO_y-compound was calculated by (Eq. 1)

$$j = \int F(\lambda,T) \cdot \sigma(\lambda,T) \cdot \varphi(\lambda)\, \mathrm{d}\lambda, \qquad (1)$$

where $F(\lambda,T)$ is the spectral emission of the UV LEDs, $\sigma(\lambda,T)$ the absorption cross section and $\varphi(\lambda)$ the quantum yield. For the calculation of the photolysis rate of the particular NO_y-compound the respective quantum yield was conservatively estimated to be equal 1, yielding an upper limit for the interference. On Page 5, L 120 now it says: The UV-induced positive bias in the NO_2-measurement due to photolysis of $BrONO_2$, HONO, NO_3 and $ClNO_2$ to produce NO was estimated at 6.1 %, 2.8 %, 2.7 % and 1.2 %, respectively, based on the absorption cross sections from the MPI-Mainz UV/VIS Spectral Atlas of Gaseous Molecules (Keller-Rudek et al., 2013). These values represent upper limits for the interference of the respective NO_y compound as the respective molecular quantum yield was estimated conservatively at 1. Note that the values represent percent interferences

if the interferent had the same concentration as NO_2. Due to small daytime concentrations of these molecules in the MBL, a UV-induced bias was neglected for the observations in this study.
Please note that the values have been revised to 6.1 %, 2.8%, 2.7 % and 1.2 % for $BrONO_2$, HONO, NO_3 and $ClNO_2$, respectively. See further changes.

Comment 2: line 181 NO2 was further measured by cavity ring-down spectroscopy (Sobanski et al., 2016) and used for correcting the instrumental background of the CLD NO2 data, as described above (the correction was taken as the ultimate absolute measurement uncertainty in the CLD NO2 data).
The uncertainty of the NO2 chemiluminescent measurement is not equal to that of the cavity ring-down instrument. The chemiluminescent NO2 is the difference between two measurements, one of which gets divided by 0.294 to take into account photolysis efficiency. In order to add errors in quadrature, I need to know the NO to NO2 ratio. I'm guessing that the relative uncertainty of NO2 will be at least twice that of NO. The NO2 chemiluminescent measurement is affected adversely by the relatively low photolysis efficiency. That accounts for random errors in NO2. Comparison with the cavity ringdown may take care of the NO2 instrumental background but how does it take care of the random errors?
Random errors are taken up by the calculation of a one-minute average before the instrumental background was estimated from the difference in the two NO_2 measurements. Note that random errors in the data are expected to be reduced as our final data analysis is based on a five minute average. NO_2 is calculated by

$$NO_2 = \frac{NO_c - NO}{K_e} \quad ,$$

where NO_c is the signal of the channel equipped with the photolytic converter, NO the signal of the NO-channel and K_e the NO_2 conversion efficiency. We agree that the relative uncertainty in the NO_2 has to be estimated by means of the largest error possible from the relative uncertainties of NO (6 %), NO_c (6 %) and the conversion efficiency K_e (3 %) rather than only from the uncertainty of the NO_c-signal and the uncertainty of the conversion efficiency. The revised TMU for NO_2 follows as:

$$\Delta NO_2 = \sqrt{\Delta NO^2 + \Delta NO_c^2 + \Delta K_e^2} = \sqrt{6\%^2 + 6\%^2 + 3\%^2} = 9\ \%.$$

We also agree that the absolute error of a single NO_2 data point might exceed 9 % when NO_2 is calculated from two high numbers (e.g. if we assume 100 ppb_v NO and 101 ppb_v NO_c, NO2 would be ~ 4 ppb_v), the error in NO_2 would be underestimated by 9 %. However the average and the median relative uncertainty of each data point of the campaign at 5 minute integration time are 13.6 % and 11.8 %, respectively, which is indeed slightly higher than the statistical estimate of 9 %. However the above average of 13.6 % yields a standard deviation of 6.9 %, which yields that both the average and the median relative uncertainty of NO_2 are significantly not different from the statistical estimate of 9 %. As we finally calculate median values for days and regions, it is more practicable to estimate a statistical error for the NO_2 measurement at 9 %. The manuscript has been explicitely revised on Page 7, L 158-160. Now it says: The TMU in NO_2 has been estimated by means of the largest error possible from error propagation at
$\Delta NO_2 = \sqrt{\Delta NO^2 + \Delta NO_c^2 + \Delta K_e^2} = \sqrt{6\%^2 + 6\%^2 + 3\%^2} = 9\ \%$
at a confidence level of 1σ and an integration time of five minutes.
Also the TMU of NO_2 in Table 1 has been corrected to 9 %.

Line 205 Total Measurement Uncertainty. All of these numbers appear very optimistic. In a previous comment, I gave my reasons why the TMU of NO2 appeared low. I do not know why the TMU of HO2 is not larger than OH. There are many sources of uncertainty in the conversion of HO2 to OH which is the quantity actually measured.

The authors state a 20% bias due to RO2 chemistry. I do not know to what extent quantification of HO2 is made easier than that of OH because there is more HO2 than OH and hence a larger signal.

The 1 sigma accuracy of OH is 20 % and the average precision is $3.4 \cdot 10^5$ molec cm^{-3}. The accuracy of HO_2 is 20 % and the largest uncertainty due to interference by contribution of RO_2 is 7 % or 3 ppt_v whichever is higher. The average precision of HO_2 is 3 ppt_v. The uncertainty in OH is estimated as the 1 sigma accuracy whereas the uncertainty in HO_2 is estimated at $\sqrt{(20\ \%)^2 + (7\ \%)^2} \approx 21\ \%$. Note that HO_2 is calculated as the difference from two signals: $HO_2 = (HO_2 + OH) - OH$, whereas the signal (HO_2+OH) is about two order of magnitude larger than the signal from OH, which means that the uncertainty in OH can be neglected in the determination of the uncertainty in HO_2. On page 8, L 190-193 now it says: HO_2 data used in this study is still preliminary due to not yet corrected interference of organic peroxy radicals RO_2. The largest uncertainty due to interference by contribution of RO_2 is 7 % or 3 ppt_v, whichever is higher. The 1 sigma accuracy of both OH and HO_2 is 20 %. The uncertainty in the OH data is here estimated as the 1 sigma accuracy of the data set at 20 %, whereas the uncertainty in HO_2 is estimated at $\sqrt{(20\ \%)^2 + (7\ \%)^2} \approx 21\ \%$. The measurement uncertainty for HO_2 has been corrected to 21 % in Table 1.

Comment 3: Line 272 “In low NOx environments (< 100 pptv) previous studies have indicated that further NO oxidizing trace gases such as peroxy radicals (HO2, RO2) and halogen monoxides (XO) may result in a deviation from unity (Nakamura et al., 2003; Hosaynali Beygi et al., 2011; Reed et al., 2016).”

Deviations from the Leighton relation can also be important at higher NO. Departures of the Leighton ratio from unity depend (primarily) on the competition between HO2+NO and O3+NO. In polluted environments, HO2 concentrations can increase, remain steady, or decrease only slowly as NO is increased.

Several studies address deviations from the Leighton Ratio. However in high NO_x regimes gaps between measurement and estimate can be closed by incorporating higher oxidations (HO_2, halogen monoxides). However, in low NO_x regimes, even addressing these further oxidants does not close the gap between observation and estimate (see for instance Hosaynali Beygi et al., 2011). We have added the following sentence Page 10, L 238: Deviations from expected NO/NO_2-ratios at low NO_x generally refer to missing oxidants converting NO to NO_2 (Hosaynali Beygi et al., 2011; Reed et al., 2016) or to a measurement error due to an instrumental background or a positive interference from thermal labile NO_x reservoir species (Reed et al., 2016; Silvern et al., 2018).

Line 250 and following. Does Fig. S1 show the ratio of actinic flux in the 4 hour window centered around noon to the total measured actinic flux? Or is Fig. S1 a ratio obtained by fitting a Gaussian, between zeroes in the AM and PM?

You are right, Figure S1 shows the ratio of the actinic flux in the 4 hour window (centered to noon) to the total measured actinic flux of that particular day. The Gaussian Fit was only used to estimate noontime of each particular day. We have revised caption of Figure S1. Now the first sentence of the caption of supplementary Figure S1 says: Ratio of the noontime actinic flux ($\pm$ 2h around noon) with regard to the total actinic flux $j(NO_2)$ of that particular day.

Comment 4: Lines 266-270, typos for O singlet D. Elsewhere, the “1” is in its proper place as a superscript.

Thank you for noticing. Now it says on Page 11, Line 269: $O(^1D) + H_2O \rightarrow 2OH$

Comment 5: Line 285. Am I correct that insofar as ozone production is concerned the only use of the HO2 and OH measurements is their contribution to the loss rate of ozone (and hence their effect on net ozone production)?

HO_x data have been used to calculate net ozone production rates, however HO_2 has also been used as a reality test: The peroxy radical estimate based on Eq. 3 was compared to measured HO_2 in Section 3.2 (Page 21, L 442).

Comment 6: Line 373. “We find that the median NOx(model)/NOx(measurement)-ratio throughout the whole campaign is 0.91, indicating that the model underestimates NOx by roughly 10 %.” The median of what? Could you please specify what items you are taking the median of; i.e., what are the data points. Ratios by Region? Days? Individual data points. I may have missed it; how long are data points? Equal to the 5 minute instrument averaging time?

The median NO_x(model)/NO_x(measurement) has been calculated as the median of five minute individual data points of the whole data set of the campaign. We have cleared out the misunderstanding in the text, now it says on Page 17, L386-387 following: We find that the median NO_x(model)/NO_x(measurement)-ratio of all five minute averaged data points of the whole campaign is 0.91, indicating that the model underestimates NO_x by roughly 10 %.

Comment 7: Line 391. “Noontime RO2 was estimated based on Eq. 3. As the steady state assumption will not hold for air masses originating from fresh emissions (times to acquire steady state estimated from the inverse sum of the loss and production terms for NO2 typically ranged from 1-2 minutes during AQABA) and for fast changes in the actinic flux,” What I think you want to say is mis-stated. As written, it says: We can’t use samples that had fresh emissions, so we used samples taken when actinic flux was slowly changing. Was the data screened to eliminate time periods in which NOx (or less likely O3) was rapidly varying? From the looks of the actinic flux plot you did not have many clouds giving rapid variations in jNO2. I would be surprised if the time window around noon could not have been wider. How much does jNO2 change between, say noon-3 hours and noon – 175 minutes and what change in HO2 does that produce?

Please note that before performing photochemistry calculation, the whole data set was filtered based on a stack filter which was established based on parameters such as wind direction, wind speed, variability in NO data, O_3, SO_2 (see Lines 209-211). However rapid changes in the actinic flux $j(NO_2)$ were observed e.g. after sunrise and before sunset. For $\pm$ 2h around noon the variation of the actinic flux (within the 4 hour period) was about 7 %, whereas the variation of the actinic flux within a 6-hour window ($\pm$ 3h around noon) would be at least 20 % and assumptions that the actinic flux does not change within this time frame would not have been supportable. Differences in the actinic flux between noon-3 hours and noon-175 minutes would already be about 2 % of the maximum noontime value (and about the same change in HO_2). Differences in the actinic flux between noon-2 hours and noon–115 minutes would also be about 1-2 % of the maximum noontime value (slightly less than for 6 hours), but however expecting to decrease to zero towards noontime. Constant RO_2 and NOPR can be rather assumed for a 4-hour window around noon than for a 6-hour window around noon.

Comment 8: Figure 6. Obtaining peroxy radical concentrations from photostationary state calculations is not easy. Line 413 “the total uncertainty in the RO2 estimates is estimated at 14%. This is a way too optimistic estimate of the uncertainty of RO2. Instrument precision is too high and no account (except for NO2) is taken of biases. Even still, the PSS is a difference in two numbers, often of comparable magnitude. I’m not certain the error propagation was correctly performed. I would like to see the formula that represents “errors added in quadrature”. Compare those results with a simple Monte Carlo calculation that can be done on a spreadsheet. And keep in mind that the result will not take into account errors in rate constants.

We agree that obtaining RO_2 from PSS calculations is not trivial and very much depends on the errors of the used quantities. The TMU in RO_2 was estimated based on Gaussian error propagation by means of the estimate of the largest error possible. RO_2 is calculated by

$$[\mathrm{RO_2}] = \frac{j(\mathrm{NO_2})\cdot[\mathrm{NO_2}] - k_{\mathrm{NO+O_3}}\cdot[\mathrm{NO}][\mathrm{O_3}]}{k_{\mathrm{NO+HO_2}}\cdot[\mathrm{NO}]}.$$

The relative uncertainty in the RO_2 data has to be calculated from the relative uncertainty of NO, NO_2, O_3 and $j(NO_2)$ at roughly 6 %, 9 % (instead of 7 %), 2 % and 10 %, respectively, which yields a relative uncertainty of 15 % for RO_2.

$$\Delta RO_2 = \sqrt{\Delta NO^2 + \Delta NO_2^2 + \Delta O_3^2 + \Delta j(NO_2)^2} = \sqrt{6\%^2 + 9\%^2 + 2\%^2 + 10\%^2} \approx 15\ \%$$

The relative uncertainty in RO_2 has been revised in the manuscript, now it says on Page 20 line 425-428: Based on the total measurement uncertainties of the measured quantities in Eq. 3, the uncertainty in RO_2 is estimated by means of the largest error possible at 15 %.

$$\Delta RO_2 = \sqrt{\Delta NO^2 + \Delta NO_2^2 + \Delta O_3^2 + \Delta j(NO_2)^2} = \sqrt{6\%^2 + 9\%^2 + 2\%^2 + 10\%^2} \approx 15\ \% \qquad (9)$$

Note that our calculation assumes that errors in the used rate coefficients are negligible.

Comment 9: Line 416. “Negative values for all regions are regularly found in the vicinity of fresh emissions and air masses not in photochemical equilibrium” That might be the explanation. It would useful to quantify this point. HO2 and RO2 concentrations will be low in a high NOx environment. The negative values may reflect the measurement accuracy needed to distinguish, for example, – 5 ppt RO2 from zero.

Note that the uncertainty of the best estimates of RO_2 for each day/each region is estimated at 15 %. A reason why negative values were regularly found in the vicinity of fresh emissions is that the assumption of photostationary steady state (PSS) might not be fulfilled for fresh emissions. Time to acquire PSS was estimated as the inverse sum of the loss and production terms of NO_2 and was of the order of 1-2 minutes during AQABA, depending on the particular conditions (temperature, radiation, ozone concentration). The assumption that the regarded air masses were in PSS might not be true in the vicinity of fresh emissions (with transport time from source to instrument of less than 2 minutes). For these air masses production of NO_2 (oxidation of NO) prevailed over photolysis of NO_2 leading to $j(NO_2) \cdot [NO_2] - k_{NO+O_3} \cdot [NO][O_3] < 0$. Negative values might hence simply reflect that the regarded air mass has not reached PSS.

Comment 10: Figure 7. Here the RO2 data looks much better. There are differences mentioned in the text. but for this reader could you please provide a concise reason why Fig. 7. looks so much better than Fig. 6. Is it the data groupings? I assume that in both Fig. 6 and 7. the blue RO2 data is from Eq. 3. I am not totally positive because you were measuring HO2 and some fraction of RO2.

Figure 7 has been processed based on five minute data points in each region whereas Figure 6 has been processed for single days which might be more biased by single data outliers. Grouping into regions rather than for single days allows for a statistically more established estimate.

Comment 11: Line 421. As peroxy radicals are short-lived molecules generated from the oxidation of VOCs, enhanced RO2 concentrations observed over the Arabian Gulf are most likely due to high VOC observed over the Arabian Gulf are most likely due to high VOC emissions from intense oil and gas activities in the region. High HO2 can also occur in aged air masses in which NOx and VOCs have reacted away but still have significant O3 and (perhaps) HCHO. Photolysis could then yield peroxy radicals.

We have added the comment to the manuscript on Page 21, L. 438-439. However high HO_2 and RO_2 can also occur in aged air massed with low NO_x and VOCs but still significant O_3 (and perhaps HCHO whose photolysis would then yield peroxy radicals).

Comment 12: Line 440. Regarding the extrapolated actinic flux curve to get a daily ozone production. j(1OD) decreases early and late in the day faster than J(NO2). Not sure how much difference it makes. I would be very leery of this extrapolation over land; I'm assuming that you are far enough away that varying traffic and boundary layer heights are not a concern.

Except for $j(O^1D)*\alpha*[O_3]$ all other terms will scale with $j(NO_2)$. However errors due to a different diurnal profiles of $j(O^1D)$ will remain insignificant with respect to the relative uncertainty of NOPR, as NOPR are mainly determined by k*[NO]*[RO_2] and loss reactions due to OH and HO_2.

Comment 13: Line 455 "the uncertainty of the regional NOPR is 40 % which has been estimated by error propagation" I don't disagree with this value. Merely surprised at its magnitude compared to a 15% uncertainty for RO2 from Eq. 3.

The uncertainty in NOPR was estimated by means of the largest error possible and is mainly driven by the high uncertainty in OH and HO_2 (20 % and 21 %, respectively) and by the uncertainty in RO_2 (15 %). Diurnal net ozone production rates were estimated by scaling the median hourly noontime value to a diurnal value (by multiplying by the hourly value by 4 due to a 4-hour window around noon and by further dividing by 0.461 (noontime fraction ($\pm$ 2h) of jNO$_2$). Strictly speaking, the relative uncertainty (6 %) in the division by 0.461, referred to as Δs (see Supplements Figure 1), also needs to be accounted for when estimating the uncertainty in NOPR. Also the error in α (Eq. 5) is rather determined by the error in H_2O (5 %) than from its relative variation over the campaign (relative variation ~ 21 %). This yields a measuremrent uncertainty for NOPR of

$$\Delta\mathrm{NOPR} = \sqrt{\Delta\mathrm{NO}^2 + \Delta\mathrm{NO}_2^2 + \Delta\mathrm{O}_3^2 + \Delta j(\mathrm{NO}_2)^2 + \Delta j(\mathrm{O}^1\mathrm{D})^2 + \Delta\alpha^2 + \Delta\mathrm{RO}_2^2 + \Delta\mathrm{OH}^2 + \Delta\mathrm{HO}_2^2 + \Delta s^2}$$
$$= \sqrt{6\%^2 + 9\%^2 + 2\%^2 + 10\%^2 + 10\%^2 + 5\%^2 + 15\%^2 + 20\%^2 + 21\%^2 + 6\%^2} \approx 38\ \%.$$

We have corrected the error in NOPR from 40 % to 38 % in the manuscript and specified error calculation in detail also for NOPR in the manuscript.

On Page 12, L274 now it says: The error in α is mainly determined by the error of H_2O at 5 %.

On Page 21, L453 now it says: These noontime values are scaled to diurnal production rates (Figure 8). As photochemical net ozone production is in good approximation linear with actinic flux $j(NO_2)$ and as on average (46.1 $\pm$ 2.8) % of the total $j(NO_2)$ occurred $\pm$ 2h around noon, the median noontime NOPR estimate was multiplied by 4/0.461 $\approx$ 8.68 to obtain a diurnal value. The error in the total actinic flux located $\pm$ 2h around noon is estimated from the standard deviation of the best estimate of 0.461 at $\Delta s \approx 6$ %.

On Page 23, L 472 now it says: Based on the total measurement uncertainties of the measured quantities in Eq. 3, the systematic error in NOPR is estimated from error propagation by means of the largest error possible at 38 %.

$$\Delta\mathrm{NOPR} = \sqrt{\Delta\mathrm{NO}^2 + \Delta\mathrm{NO}_2^2 + \Delta\mathrm{O}_3^2 + \Delta j(\mathrm{NO}_2)^2 + \Delta j(\mathrm{O}^1\mathrm{D})^2 + \Delta\alpha^2 + \Delta\mathrm{RO}_2^2 + \Delta\mathrm{OH}^2 + \Delta\mathrm{HO}_2^2 + \Delta s^2}$$
$$= \sqrt{6\%^2 + 9\%^2 + 2\%^2 + 10\%^2 + 10\%^2 + 5\%^2 + 15\%^2 + 20\%^2 + 21\%^2 + 6\%^2} \approx 38\ \%.$$

Comment 14: Line 473. "Although EMAC predicts high ozone levels over the Arabian Sea, it also reports the lowest NOPR in this region. Deviations between model-calculated estimate and the estimate based on measured

tracer data over the Mediterranean and over the Southern Red Sea could be linked to NOx being overestimated in the model in these regions." I'm not following. There is a low net ozone production rate. which to me implies that the model has a too low NO concentration, but you say that the model overpredicts NOx.

As demonstrated in Figure 4, the model overpredicts the NO_x measurement over the Mediterranean and the Southern Red Sea. As these regions are classified as rather NO_x sensitive regimes (see Figure 10), higher NO_x (in the model) will likewise imply higher NOPR (under stagnant chemistry, i.e. NO_x sensitivity). The text is not fully clear and will be rewritten on P. 23 L492-495 as: Although EMAC predicts high ozone levels over the Arabian Sea, it also reports the lowest NOPR in this region. On the other side, the large overestimation of the model-calculated estimate NOPR against the one based on measured tracer data over the Mediterranean and over the Southern Red Sea could be linked to NO_x being overestimated in the model in these regions.

Comment 15: Section 3.4 VOC and NOx sensitivity. Makes sense.

We have changed the title of chapter 3.4 to VOC- and NO_x-sensitivity.

Further changes

We have further made the following changes in the manuscript:

Change 1: There has been an updated version of the preliminary HO_2 data, which were used to revise NOPR in the different regions yielding 16 ppb_v day^{-1} over the Oman Gulf (instead of 14 ppb_v day^{-1}), 32 ppb_v day^{-1} over the Arabian Gulf (instead of 28 ppb_v day^{-1}) and -1 ppb_v day^{-1} over the Mediterranean (instead of -2 ppb_v day^{-1}). The values have been corrected in the manuscript and the supplement, e.g. in Line 17 now it says: Net ozone production rates (NOPR) were greatest with 16 ppb_v day^{-1} over both the Gulf of Oman and the Northern Red Sea and with 32 ppb_v day^{-1} over the Arabian Gulf.
In the manuscript in Line 490 and Line 569 the values have also been revised. We have also revised the median noontime RO_2(measurement estimate)/HO_2(estimate)-ratio to 1.88 in Line 450-451: We find that the median noontime RO_2(measurement estimate)/HO_2(estimate)-ratio throughout the whole campaign is 1.88.
A new file with updated HO_2 data has been uploaded to zenodo and a new DOI has been generated. The data is now available at https://doi.org/10.5281/zenodo.3693988.

Change 2: Each end of the photolytic converter features 200 UV LED units instead of 50 UV LED units. In Line 122, 123 now it says: The photolytic NO_2 converter features a set of 200 UV LED units attached to each end of the converter.

Change 3: The calculation of the UV-induced positive bias was revised, which reduced the estimated maximum interferences of $BrONO_2$, HONO, NO_3 and $ClNO_2$ to 6.1 %, 2.8 %, 2.7 % and 1.2 %, respectively (instead of 7.7 %, 7.2 %, 5.6 % and 1.5 % for HONO, $BrONO_2$, NO_3 and $ClNO_2$, respectively). Now it says in Line 124-127: The UV-induced positive bias in the NO_2-measurement due to photolysis of $BrONO_2$, HONO, NO_3 and $ClNO_2$ to produce NO was estimated at 6.1 %, 2.8 %, 2.7 % and 1.2 %, respectively, based on the absorption cross sections from the MPI-Mainz UV/VIS Spectral Atlas of Gaseous Molecules (Keller-Rudek et al., 2013).

Change 4: In the manuscript it says "supplementary Figure" and "supplementary Table" instead of "supplements Figure" and "supplements Table", respectively. Also we now write "Figure" and "Table" instead of "Fig." and "Tab.", respectively, and we have revised the used date format in the manuscript to, e.g. 21 July 2017 instead of July 21st 2017.

Change 5: Table 1 was moved into the supplement. Figure S5 was also added to the supplement. All other figures and tables have been numbered accordingly in the manuscript and supplement.

Change 6: In the caption of supplementary Figures S6-S9 now it says "The error bars represent the 25-75-percentile variation" instead of "The error bars are represented by the 25-75-percentile variation"

Changes made to the final manuscript and supplements are written in red.

Net ozone production and its relationship to NO_x and VOCs in the marine boundary layer around the Arabian Peninsula

Ivan Tadic[1], John N. Crowley[1], Dirk Dienhart[1], Philipp Eger[1], Hartwig Harder[1], Bettina Hottmann[1], Monica Martinez[1], Uwe Parchatka[1], Jean-Daniel Paris[2], Andrea Pozzer[1,4], Roland Rohloff[1], Jan Schuladen[1], Justin Shenolikar[1], Sebastian Tauer[1], Jos Lelieveld[1,3], and Horst Fischer[1]

[1]Atmospheric Chemistry Department, Max Planck Institute for Chemistry, Mainz, Germany
[2]Laboratoire des Sciences du Climat et de l'Environnement, LSCE/IPSL, CEA-CNRS-UVSQ, Université Paris-Saclay, Gif-sur-Yvette, France
[3]Energy, Environment and Water Research Center, The Cyprus Institute, Nicosia, Cyprus
[4]International Centre for Theoretical Physics, Trieste, Italy

Correspondence to: Ivan Tadic (i.tadic@mpic.de)

Abstract. Strongly enhanced tropospheric ozone mixing ratios have been reported in the Arabian Basin, a region with intense solar radiation and high concentrations of ozone precursors such as nitrogen oxides and volatile organic compounds. To analyze photochemical ozone production in the marine boundary layer (MBL) around the Arabian Peninsula, we use ship-borne observations of NO, NO_2, O_3, OH, HO_2, HCHO, actinic flux, water vapor, pressure and temperature obtained during the summer 2017 Air Quality and Climate in the Arabian Basin (AQABA) campaign, compare them to simulation results of the ECHAM-MESSy atmospheric chemistry (EMAC) general circulation model. Net ozone production rates (NOPR) were greatest with 16 ppb_v day^{-1} over both the Gulf of Oman and the Northern Red Sea and with 32 ppb_v day^{-1} over the Arabian Gulf. NOPR over the Mediterranean, the Southern Red Sea and the Arabian Sea did not significantly deviate from zero; however, results for the Arabian Sea indicate weak net ozone production of 5 ppb_v day^{-1}, and net ozone destruction over the Mediterranean and the Southern Red Sea with -1 ppb_v day^{-1} and -4 ppb_v day^{-1}, respectively. Constrained by HCHO/NO_2-ratios, our photochemistry calculations show that net ozone production in the MBL around the Arabian Peninsula occurs mostly in NO_x-limitation regimes with a significant share of ozone production occurring in the transition regime between NO_x- and VOC-limitation over the Mediterranean and more significantly over the Northern Red Sea and Oman Gulf.

1 Introduction

Revenues from exploitation of the great oil reserves in the states of and around the Arabian Peninsula have propelled remarkable economic development associated with industrialization and urbanization. Strong population growth and anthropogenic emissions of gases and particulates in the last few decades have resulted in the Middle East becoming a hotspot for air pollution and associated health effects, while it is also one of the regions worldwide where climate change is particularly rapid (Lelieveld et al., 2016a). Unique meteorological conditions such as intense solar radiation, high temperatures and aridity, as well as strong anthropogenic emissions of volatile organic compounds (VOCs) and NO_x (= NO + NO_2) by on- and off-shore petrochemical industries, dense ship traffic, fossil energy production for air conditioning and desalination, and urban development are expected to further intensify in the future and contribute to photochemical ozone production (Lelieveld et al, 2009; Krotkov et al., 2016; Pfannerstill et al., 2019). Understanding the sources and sinks of NO_x and other ozone precursors on and around the Arabian Peninsula is therefore of major importance for atmospheric chemistry studies, including the investigation of net ozone production rates (NOPR) (Monks et al., 2015; Reed et al., 2016; Bozem et al., 2017).

NO_x plays a central role in atmospheric photochemistry (Nakamura et al., 2003; Tuzson et al., 2013; Reed et al., 2016). It is the primary precursor for tropospheric ozone (O_3), secondary organic aerosols and photochemical smog in urban areas (Hollaway et al., 2012; Javed et al., 2019). Main ground-based sources of NO and NO_2 are fossil fuel combustion and to a lesser extent bacterial processes in soils, and both lightning and aircraft emissions in the upper troposphere (Nakamura et al., 2003; Miyazaki et al., 2017; Javed et al., 2019). Transport of NO_x in the atmosphere is relatively limited due to its short lifetime of a few hours (Reed et al., 2016). It is removed from the troposphere mainly by conversion to HNO_3 (via reaction with OH) during the day, or the formation of N_2O_5 (in the reaction of NO_2 with NO_3 at night-time), which also leads to formation of nitric acid by heterogeneous hydrolysis on aerosol surfaces (Crutzen, 1973; Liu et al., 2016; Reed et al., 2016). Ultimately, the deposition of HNO_3 constitutes the major loss process of NO_x from the atmosphere. Ozone is a secondary pollutant that is photochemically formed in the troposphere from its precursors NO_x and VOCs (Bozem et al., 2017; Jaffe et al., 2018). It is an important greenhouse gas, an atmospheric oxidant and the most important primary precursor for OH (Lelieveld et al., 2004; Monks et al., 2015; Bozem et al., 2017). O_3 in the planetary boundary layer causes health damage, notably respiratory diseases, and reduces crop yields (Monks et al., 2015; Jaffe et al., 2018).

NO_x and O_3 mixing ratios in the troposphere vary from less than 20 ppt_v and 10 ppb_v, respectively, for pristine conditions such as the remote marine boundary layer (MBL) up to mixing ratios of several hundreds of ppb_v in regions with heavy automobile traffic and in international shipping lanes (for NO_x) and downwind of urbanized areas (for O_3) (Reed et al., 2016; Jaffe et al., 2018). Low NO_x environments such as the clean MBL and the lower free troposphere are considered net ozone destruction regimes whereas the upper troposphere and areas with anthropogenic emissions of ozone precursors are regions

of net ozone production (Klonecki and Levy, 1997; Bozem et al., 2017). Measurements performed in the the Houston Ship Channel revealed NOPR of the order of several tens of ppb h^{-1} (Chen et al., 2010; Mao et al., 2010; Ren et al., 2013).

In the last decade much effort has been successfully devoted to the mitigation of NO_x emissions over Europe and America, and levels of reactive nitrogen trace gases have decreased (Miyazaki et al., 2017). But in Asia, India and the Middle East, NO_x emissions have substantially increased during the last decade so that the global NO_x burden has essentially remained constant (Miyazaki et al., 2017). NO_x emissions by ocean-going vessels have attracted considerable attention as they are reported to account for 15 % of the global NO_x emission burden (Celik et al., 2019). Model calculations suggest that the Arabian Gulf, with an estimated annual NO_x emission density of about one ton km^{-2} from ship traffic, is among the regions with highest NO_x emission densities worldwide (Johansson et al., 2017). Although NO_x emissions in the Red Sea and Arabian Sea areas were reported to be three and five times smaller than for the Arabian Gulf, respectively, these values are still 50-100 times larger than the emission density reported for the South Pacific Ocean, for example (Johansson et al., 2017).

In the present study, we characterize photochemical NOPR in the MBL around the Arabian Peninsula. In Sect. 2, the campaign, instrument description, data processing and a description of the methods used in this study is presented. In Sect. 3, mixing ratios of nitrogen oxides and ozone around the Arabian Peninsula are reported. Based on concurrent measurements of HO_x, actinic flux, temperature and pressure, noontime RO_2 mixing ratios are estimated and used to calculate NOPR in the different regions around the Arabian Peninsula. Observation-based analysis of HCHO/NO_2-ratios will be used to distinguish between NO_x- or VOC-limited chemistry in the particular regions. A comparison of the results with data retrieved from the 3D global circulation model EMAC is also included.

2 Experimental

2.1 AQABA campaign

The AQABA ship campaign (**A**ir **Q**uality and Climate in the **A**rabian **Ba**sin) investigated the chemical composition of the MBL around the Arabian Peninsula. From late June to early September 2017, the *Kommandor Iona* Research and Survey Vessel sailed from Toulon (France) to Kuwait and back in order to perform gas-phase and particle measurements in the region. The gas-phase and aerosol measurement instrumentation was housed in five laboratory containers on the front deck. A 6 m high, 20 cm diameter cylindrical stainless steel common inlet was installed on the front deck of the vessel to sample air at a total mass flow rate of 10,000 SLM. NO and NO_2 chemiluminescence measurements were obtained at a total bypass flow rate of 28.5 SLM sampling air from the common inlet with a residence time in the tubing of ~3 s. HCHO, NO_2 cavity ring-down spectroscopy and O_3 measurements were obtained with similar bypass systems sampling air from the common inlet. H_2O vapor was measured on the top of the ship mast in the front. The OH and HO_2 detection units were placed on the prow to allow for inlets with residence times less than 10 ms.

The *Kommandor Iona* left Malta in late June 2017 traversing the Mediterranean Basin, the Suez Canal and the Northern Red Sea. A 3 day stop over at KAUST University (Saudi Arabia) was made from 11 July 2017 to 13 July 2017 before passing the Southern Red Sea area. On 17 July 2017, we briefly stopped at Djibouti port before passing the Gulf of Aden, the Arabian Sea and the Gulf of Oman. Kuwait at the northern end of the Arabian Gulf marked the turning point of the ship cruise where, during a second 3-day stop-over, scientific staff was exchanged. The *Kommandor Iona* started the second leg on 03 August 2017 arriving in Toulon (France) in early September 2017 without any further stops. Figure 1 shows the ship's route subdivided into six different regimes.

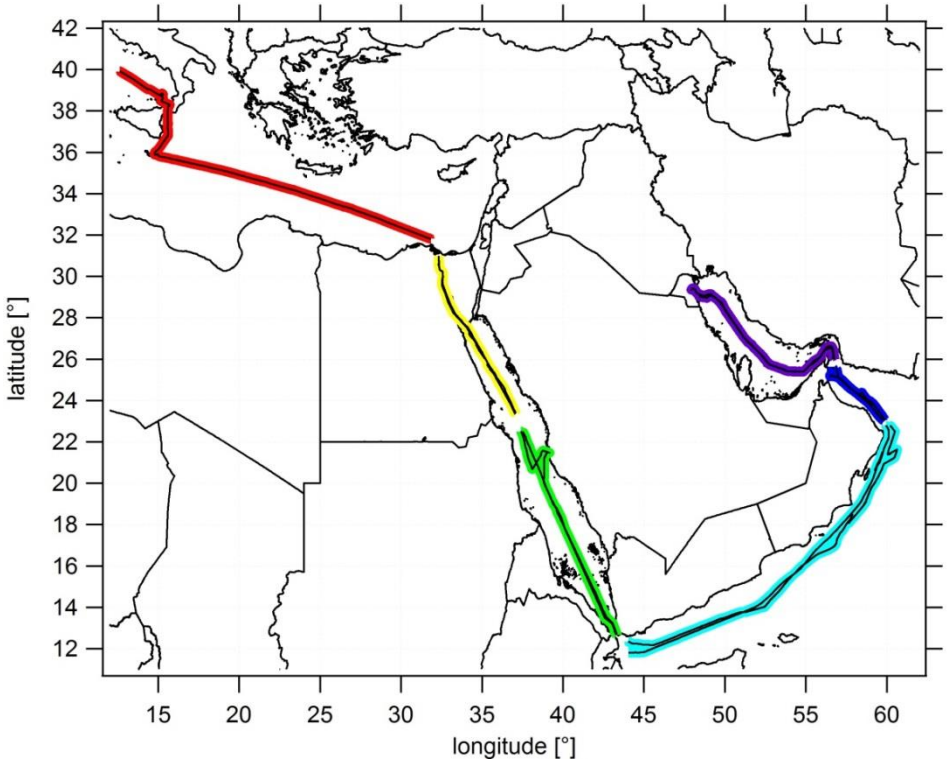

Figure 1: Ship cruises during both legs and color-coded subdivision into six different regimes. The following abbreviations will be used: AG for Arabian Gulf (purple), OG for Oman Gulf (dark blue), AS for Arabian Sea (blue), SRS for Southern Red Sea (green), NRS for Northern Red Sea (yellow), M for Mediterranean (red).

To enhance the statistical significance of our results and due to comparable signatures of the NO_x and O_3 measurements in the northern part of the Red Sea, the Suez Gulf and the Suez Canal, we have combined these regions which are represented by the 'Northern Red Sea' (NRS). For the same reasons we have merged the Gulf of Aden with the Arabian Sea (AS). See supplementary Table ST1 for the range of latitudinal and longitudinal coordinates of the different regions and supplementary Table ST2 for a detailed day to day description of the route.

2.2 Measurements of nitrogen oxides during AQABA

Chemiluminescent detection of NO and NO_2 is a widely applied method to quantify mixing ratios from the ppm_v down to the low ppt_v range (Nakamura et al., 2003; Pollack et al., 2011; Hosaynali Beygi et al., 2011; Reed et al., 2016). During AQABA we deployed a compact, robust and commercially available two-channel chemiluminescence instrument CLD 790 SR (ECO Physics AG, Dürnten, Switzerland) that has been optimized for in situ field measurements during the last decade (Hosaynali Beygi et al., 2011). The measurement principle of the CLD is based on the addition of O_3 to NO to produce stoichiometric quantities of excited state NO_2^* that will emit an infrared photon (λ > 600 nm) forming the chemiluminescent detection principle for NO (Drummond et al., 1985; Reed et al., 2016). Both channels feature an identical layout and were operated at a mass flow of 1.5 SLM during AQABA. One channel of the CLD (NO_c-channel) has additionally been equipped with a LED solid state photolytic converter (Droplet Measurement Techniques, Boulder, Colorado) installed upstream of the O_3 addition to selectively photolyze NO_2 to NO, which is subsequently measured. In this section, we will concentrate on modifications made prior to the campaign and especially on operational conditions of the photolytic converter during the campaign. Further details on the measurement principle are described elsewhere (Pollack et al., 2011; Hosaynali Beygi et al., 2011; Reed et al., 2016).

During AQABA, the cylindrical photolytic converter (length 14 cm, volume ~ 0.079 l) was operated at a constant pressure of 95 hPa yielding a residence time of ~ 0.3 s. The photolytic NO_2 converter features a set of 200 UV LED units attached to each end of the converter. The emission profile of the UV LED units was characterized in laboratory measurements to peak at 398 nm with a Full Width at Half Maximum (FWHM) of 16 nm. The UV-induced positive bias in the NO_2-measurement due to photolysis of $BrONO_2$, HONO, NO_3 and $ClNO_2$ to produce NO was estimated at 6.1 %, 2.8 %, 2.7 % and 1.2 %, respectively, based on the absorption cross sections from the MPI-Mainz UV/VIS Spectral Atlas of Gaseous Molecules (Keller-Rudek et al., 2013). These values represent upper limits for the interference of the respective NO_y compound as the respective molecular quantum yield was estimated conservatively at 1. Note that the values represent percent interferences if the interferent had the same concentration as NO_2. Due to small daytime concentrations of these molecules in the MBL, a UV-induced bias was neglected for the observations in this study. To limit wall loss of NO_2, the inner cavity surface is made of PTFE (polytetrafluoroethylene), which may potentially provide a reservoir (via surface adsorption) for NO_y that can thermally dissociate to increase the background signal of the NO_2 measurement (Reed et al., 2016). The conversion efficiency K_e of the photolytic NO_2 conversion was estimated by gas phase titration (SYCOS K-GPT-DLR, ansyco, Karlsruhe, Germany) several times before, during and after the campaign at (29.4 ± 0.9) % allowing the calculation of NO_2 concentrations by $[NO_2] = \frac{[NO_c]-[NO]}{K_e}$. To avoid chemical interferences due to adding ozone in excess during a gas phase titration, a small but not vanishing amount of NO has always been left unoxidized during gas phase titrations.

During AQABA, regular dry zero-air measurements as well as NO and NO_2 calibrations were performed autonomously over a 10 minute period every 6 hours to accurately quantify the instrumental background and to correct for sensitivity drifts. An autonomous cycle of '2 min zero air measurements – 2 min NO calibration – 2 min zero air measurement – 2 min NO_2 calibration – 2 min zero air measurement' was implemented. Continuous flows NO and NO_2 calibration gases were added to the synthetic airflow or directed to a pump by switching solenoid valves. The NO calibration standard (1.954 ± 0.039 ppm_v NO in N_2, Air Liquide, Germany) used during the campaign was compared to a primary standard (5.004 ± 0.025) ppm_v (NPL, Teddington, UK) after the campaign yielding an effective NO mixing ratio of (2.060 ± 0.057) ppm_v in the NO calibration gas. Zero air measurements and NO calibrations were performed with a total flow of 3.44 SLM achieving an overflow of 0.44 SLM to guarantee ambient air free standard measurements. The calibration gas was added at 4.5 sccm to the zero air flow. During AQABA, NO calibrations at 2.5 ppb_v were achieved. During the first leg of the campaign, zero air was sampled from a bottle (Westfalen AG, Germany), whereas during the second leg zero air was generated from a zero air generator (Air Purifier CAP 180, acuraLine). Zero air measurements generated with the zero air generator were statistically not significantly different from those achieved by a bottle. To correctly account for the photomultiplier background and chemical interferences due to reactions of ozone with ambient alkenes additional pre-chamber measurements were performed every 5 minutes as well as at the beginning of zero air measurements and calibrations for 25 s each. This correction is removing a large fraction of the interference signal from alkenes. However, in regions where alkene concentrations are strongly varying in time and magnitude, the CLD is prone to enhanced backgrounds due to the interference of alkenes with ozone in the instrument. A schematic setup of the two-channel CLD instrument is given in Figure 2.

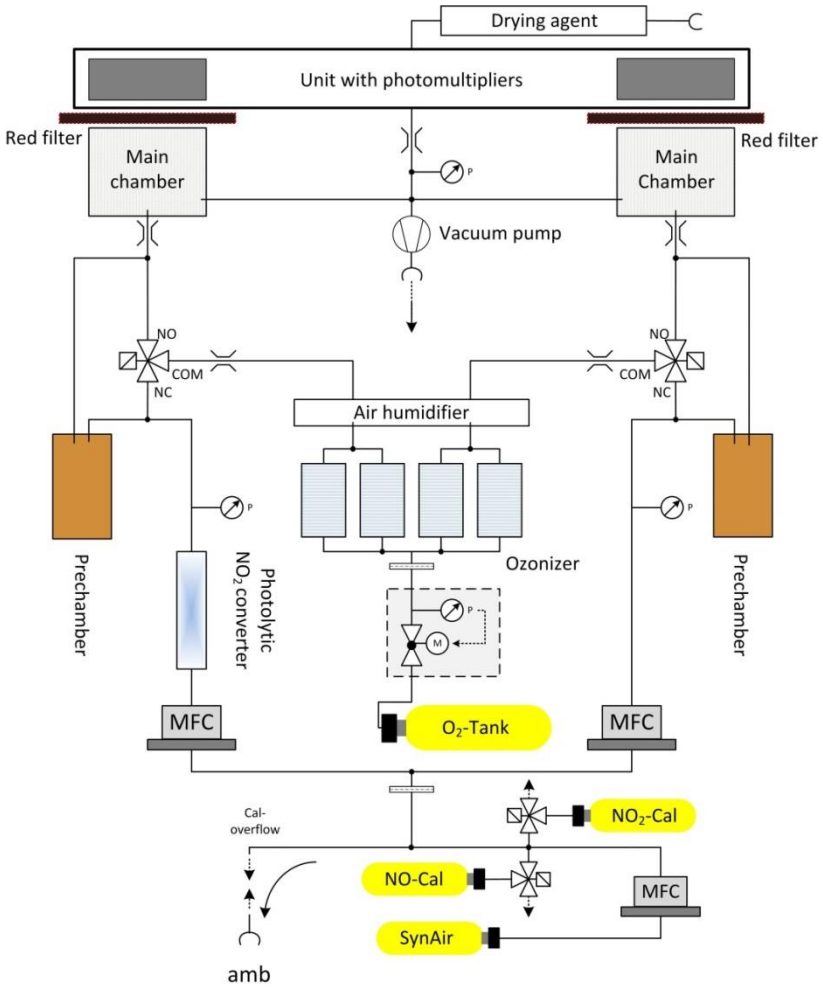

Figure 2: Schematic setup of the two channel CLD instrument in the configuration used during AQABA. NO and NO_2 calibration gases were running continuously and were added to the zero airflow by switching the respective solenoid valves.

The total measurement uncertainty (TMU) in the NO data is 5.5 % at a 5 min integration time and a confidence level of 1σ. The limit of detection in the NO channel was estimated as the full width at half maximum of the frequency distribution of all zero air measurements obtained during the campaign to be 9 ppt_v at a 5 min integration time and a confidence level of 1σ. The TMU in NO_2 has been estimated by means of the largest error possible from error propagation at

$$\Delta NO_2 = \sqrt{\Delta NO^2 + \Delta NO_c^2 + \Delta K_e^2} = \sqrt{6\%^{\,2} + 6\%^{\,2} + 3\%^{\,2}} = 9\ \%$$

at a confidence level of 1σ and an integration time of five minutes. As the zero air measurements in the NO_2 channel produced an increased background affected by memory effects after exposure to high NO_x levels e.g. during measurements of stack emissions, the NO_2 raw data were initially processed without converter background subtraction. As we therefore expect the CLD NO_2 data to be offset due to not being initially background corrected, the converter background was estimated at 112 ppt_v from the centre of a Gaussian fit representing the difference of 1-minute averaged CLD NO_2 and

concurrent cavity ring-down spectroscopy (CRDS) NO_2 measurements for data points below 10 ppb_v. Setting the threshold for calculating the difference of the two concurrent data sets to 10 ppb_v is somewhat arbitrary, however, changing this limit to 5 ppb_v or 20 ppb_v does not significantly vary the estimated offset of the CLD NO_2 data. The offset correction of 112 ppt_v was taken as the ultimate absolute measurement uncertainty of the CLD NO_2 measurement. Further corrections of to the final CLD data include residence time corrections as well as corrections for NO and O_3 losses and the subsequent formation of NO_2 in the sampling line (Ryerson et al., 2000). Both NO and NO_2 CLD data have also been corrected for nonlinearities for concentrations higher than 55 ppb_v, as experienced during probing of stack emissions.

2.3 Further measurements used in this study

An extensive set of concurrent measurements providing mixing ratios of O_3, NO_2, HCHO, OH, HO_2, absolute humidity and actinic flux, temperature and pressure data obtained during AQABA was used in this study. Ozone was measured with an absorption photometer (Model 202 Ozone Monitor, 2B Technologies, Boulder, Colorado) based on the well-established absorption of the mercury line in the Hartley band at 254 nm (Viallon et al., 2015). Eliminating water and particle interferences during sampling was achieved via sampling through a nafion tube and a Teflon filter. The ozone monitor was zeroed ten times during the campaign. NO_2 was further measured by cavity ring-down spectroscopy (Sobanski et al., 2016) and used for correcting the instrumental background of the CLD NO_2 data, as described above (the correction was taken as the ultimate absolute measurement uncertainty in the CLD NO_2 data). Note that in this study we will use the NO_2 CLD data rather than the NO_2 CRDS data as the temporal coverage of the CLD NO_2 data over the course of the campaign is about 60 % compared to about 35 % for the cavity ring-down measurement. Formaldehyde (HCHO) was measured with an Aerolaser 4021 (AERO-LASER GmbH, Garmisch-Partenkirchen, Germany), which is a fully automatized monitor based on the Hantzsch technique (Kormann et al., 2003). H_2O measurements were obtained using a cavity ring-down spectroscopy monitor (PICARRO G2401, Santa Clara, California) supervised by Laboratoire des Sciences du Climat et de l'Environnement (LSCE) (Kwok et al., 2015). Measurements of OH and HO_2 were performed with the custom-built **H**ydr**O**xyl **R**adical measurement **U**nit based on fluorescence **S**pectroscopy (HORUS) instrument based on laser-induced fluorescence (LIF) spectroscopy of the OH molecule and NO titration of HO_2 to OH followed by LIF spectroscopy detection of the OH molecule (Martinez et al., 2010; Regelin et al., 2013). HO_2 data used in this study is still preliminary due to not yet corrected interference of organic peroxy radicals RO_2. The largest uncertainty due to interference by contribution of RO_2 is 7 % or 3 ppt_v whichever is higher. The 1 sigma accuracy of both OH and HO_2 is 20 %. The uncertainty in the OH data is here estimated as the 1 sigma accuracy of the data set at 20 %, whereas the uncertainty in HO_2 is estimated at $\sqrt{20\,\%^2 + 7\,\%^2} \approx 21\,\%$. Wavelength resolved down-welling actinic flux was measured with a spectral radiometer (model CCD Spectroradiometer 85237). The *j*-values for NO_2 and O_3 were not corrected for upwelling UV radiation and were estimated to have a ~ 10 % measurement uncertainty (Meusel et al., 2016). The radiometer was installed 10 m above sea level, respectively 5 m above the front deck surface. Decreases in sensitivity due to sensor contamination with e.g. sea-spray

were corrected with a linear interpolation between two (daily) cleaning events. Temperature and pressure measurements were performed with the Shipborne **Eu**ropean **C**ommon **A**utomatic **W**eather **S**tation (EUCAWS), a weather station specifically designed for ships. The weather station incorporates sensors, processing units, satellite positioning and communication systems in one device and is implemented and coordinated by the European National Meteorological Service EUMETNET. Table 1 lists the measurement methods and the TMU for each observation.

Table 1: List of observations and gas phase measurements during AQABA. The TMU at a confidence level of 1σ and at the particular temporal resolution as well as a reference of the measurement operability are given.

Molecule	Method	TMU	References
NO	chemiluminescence	6 %	Hosaynali Beygi et al., 2011
NO_2	photolysis-chemiluminescence	9 %	Hosaynali Beygi et al., 2011
NO_2	cavity ring-down spectroscopy	7 %	Sobanski et al., 2016
O_3	UV absorbance	2 %	Viallon et al., 2015
OH	LIF	20 %	Martinez et al., 2010
HO_2	NO titration / LIF	21 %	Martinez et al., 2010
HCHO	Hantzsch technique	13 %	Kormann et al., 2003
H_2O	cavity ring-down spectroscopy	5 %	Kwok et al., 2015
actinic flux	spectral radiometer	10 %	Meusel et al., 2016

The *Kommandor Iona* Research and Survey Vessel sailed whenever possible with the wind coming from the bow to avoid contamination by stack emissions. However, based on the relative wind direction, the variability in NO as well as the temporal evolution of NO_x, SO_2, and O_3 sections of data in which the air mass was contaminated by the ship's stack were identified. All data used here to calculate RO_2 and NOPR have been filtered to remove contaminated air masses. Altogether, 21 % of the sampling time was potentially contaminated by the ship exhaust of the KI of which 87 % occurred on the first leg. During the second leg the ship sailed against the wind and most of the data was free of stack contamination. Our analysis is based on a 5-minute running mean for each data set, whereby only averages that have been calculated at a temporal coverage greater than 30 % have been used. A time series of the NO, NO_2 (both CLD), O_3, OH, HO_2 preliminary and $j(NO_2)$ measurements is given in the supplementary Figures S2 and S3.

NO and NO_2 were measured from 03 July 2017 to 31 August 2017, O_3 was measured from 22 June 2017 to 01 September 2017, HCHO from 01 July 2017 to 31 August 2017 and OH and HO_2 from 18 July 2017 to 31 August 2017. For the analysis of peroxy radicals RO_2 and NOPR around the Arabian Peninsula we have removed data measured during the stop-overs in Jeddah (11 July to 13 July), Kuwait (31 July to 03 August) and during bunkering at Fujairah City (06 August, 07:00 – 15:00

225 UTC). Due to HO_x data being available from 18 July 2017 onward, we have limited the net ozone production analysis to the period after this date.

2.4 Methods

The so-called NO_x-O_3-null cycle represents a rapid daytime cycling between NO, NO_2 and O_3. Solar UV radiation
230 photolyzes NO_2 to NO and $O(^3P)$ (R1) which will reform O_3 in the subsequent reaction with molecular oxygen O_2 (R2) (Leighton, 1961). NO and O_3 react to form NO_2 and O_2 (R3). R1, R2 and R3 constitute a so called null cycle which establishes photostationary steady state (PSS) for both NO_x and O_3 in mid latitudes during noon time on a time scale of ~100 s (Thornton et al., 2002; Mannschreck et al., 2004).

$$NO_2 + h\nu\ (\lambda < 424\ nm) \rightarrow NO + O(^3P) \quad (R1)$$

235 $$O_2 + O(^3P) + M \rightarrow O_3 + M \quad (R2)$$

$$NO + O_3 \rightarrow NO_2 + O_2 \quad (R3)$$

Under the assumption of PSS, the Leighton Ratio φ is unity (Leighton, 1961)

$$\varphi = \frac{j(NO_2)\cdot[NO_2]}{k_{NO+O_3}\cdot[NO][O_3]} = 1 \quad (1)$$

with $j(NO_2)$ being the NO_2 photolysis rate [s^{-1}]. In low NO_x environments (< 100 ppt_v) previous studies have indicated that
240 further NO oxidizing trace gases such as peroxy radicals (HO_2, RO_2) and halogen monoxides (XO) may result in a deviation from unity (Nakamura et al., 2003; Hosaynali Beygi et al., 2011; Reed et al., 2016).

$$NO + HO_2 \rightarrow NO_2 + OH \quad (R4)$$

$$NO + RO_2 \rightarrow NO_2 + RO \quad (R5)$$

$$NO + XO \rightarrow NO_2 + X \quad (R6)$$

245 Deviations from expected NO/NO_2-ratios at low NO_x generally refer to missing oxidants converting NO to NO_2 (Hosaynali Beygi et al., 2011; Reed et al., 2016) or to a measurement error due to an instrumental background or a positive interference from thermal labile NO_x reservoir species (Reed et al., 2016; Silvern et al., 2018). In the present study we include HO_2 and R_iO_2 into the production term for NO_2.

$$j(NO_2)\cdot[NO_2] = k_{NO+O_3}\cdot[NO][O_3] + k_{NO+HO_2}\cdot[NO][HO_2] + [NO]\cdot\sum_i k_{NO+R_iO_2}\cdot[R_iO_2] \quad (2)$$

Assuming that the temperature-dependent rate coefficient for the reaction of each particular peroxy radical R_iO_2 with NO equals the rate k_{NO+HO_2} for Reaction R4 (Hauglustaine et al., 1996; Cantrell et al., 1997; Thornton et al., 2002), we can combine HO_2 and the sum of all organic peroxy radicals R_iO_2 to the entity RO_2 that can be estimated using the steady state equation

$$[RO_2] = \frac{j(NO_2)\cdot[NO_2] - k_{NO+O_3}\cdot[NO][O_3]}{k_{NO+HO_2}\cdot[NO]}. \quad (3)$$

However, the steady state assumption is not valid if the sampled air parcel is affected by fresh emissions or fast changes in the actinic flux (Thornton et al., 2002). After sampling a fresh emission e.g. a ship plume, for which NO_x went up typically to values of several tens of ppb_v with simultaneous titration in O_3, we assume that PSS is re-established on a time scale of 2 minutes (Thornton et al., 2002; Mannschreck et al., 2004). To best approximate PSS in our analysis we have restricted the estimation of RO_2 on time frames $\pm$ 2 h around noontime for which we expect the smallest relative changes in the actinic flux. Noontime for each day was determined as the centre of a Gaussian fit that was applied to the actinic flux data. We applied a Gaussian Fit to the actinic flux data as this fitting method is sufficient to estimate the centre of the diurnal actinic flux. To further limit the effect of periods for which PSS is not fulfilled, we use the median instead of the average that is often disproportionately biased by strong NO_x sources nearby. See supplementary Tables ST3, ST5 and ST7 for detailed statistics and a further motivation on regional averages and median values. See supplementary Figure S1 for a detailed illustration of the calculation of the fraction of the noontime integral.

A further part of the analysis will be the investigation of NOPR. Ozone production is initiated by reactions that produce HO_x, for which primary production is from the photolysis of ozone, formaldehyde, nitrous acid (HONO) and hydrogen peroxide (H_2O_2) (Thornton et al., 2002; Lu et al., 2010; Hens et al., 2014; Mallik et al., 2018). The production of ozone can be approximated by the rate of oxidation of NO with RO_2 (HO_2 + $\Sigma_i R_iO_2$) to form NO_2 that will rapidly form O_3 (R1-R2) (Bozem et al., 2017). For RO_2 we use the result from Eq. 3 that incorporates HO_2 and the sum of all further peroxy radicals $\sum_i R_iO_2$ (Parrish et al., 1986; Thornton et al., 2002).

$$P(O_3) = k_{NO+HO_2}\cdot[NO][RO_2] \quad (4)$$

Photochemical O_3 loss is mainly due to photolysis ($\lambda < 340$ nm) in the presence of water vapor and the reactions of ozone with OH and HO_2 (Bozem et al., 2017).

$$O_3 + h\nu\ (\lambda < 340\ nm) \rightarrow O_2 + O(1D) \quad (R7.1)$$

$$O(^1D) + H_2O \rightarrow 2OH \quad (R7.2)$$

$$O_3 + OH \rightarrow HO_2 + O_2 \quad (R8)$$

$$O_3 + HO_2 \rightarrow OH + 2O_2 \quad (R9)$$

α, the fraction of $O(^1D)$ that reacts with H_2O

$$\alpha = \frac{k_{O(1D)+H_2O}[H_2O]}{k_{O(1D)+H_2O}[H_2O]+k_{O(1D)+M}[M]} \quad (5)$$

was (10.6 ± 2.2) % during AQABA with a quasi linear dependence on water concentrations. The error in α is mainly determined by the error of H_2O at 5 %. Furthermore, ozone is lost due to reactions with alkenes (R12) and halogen radicals (R13).

$$O_3 + \text{alkenes} \rightarrow \text{radicals} \quad (R12)$$

$$O_3 + X \rightarrow O_2 + XO \quad (R13)$$

We find that the loss rate is dominated by the photolysis of ozone with subsequent reaction of $O(^1D)$ with H_2O, was 60 – 80 % of the total loss rate, followed by the reaction of O_3 with HO_2, which makes up 10 – 30 % (note that the uncertainty in HO_2 radical concentrations mentioned above has no significant influence on the total O_3 loss rate, due to its small contribution). The remaining fraction (10-30 %) is due to the reaction of O_3 with OH. The reaction of ozone with ethene is on average 0.005 – 0.01 ppb_v h^{-1} and therefore generally less than 2 % of the total ozone loss rate (Bourtsoukidis et al., 2019). The reaction of O_3 with all alkenes will hence be neglected. Halogen radicals were not measured during AQABA and will not be incorporated into our study. Based on oxidative pairs, Bourtsoukidis et al. (2019) have classified the majority of their samples collected during AQABA by an OH/Cl-ratio of 200:1. As measured daytime OH concentrations were of the order of $5 \cdot 10^6$ molecule cm^{-3}, the estimate would yield a Cl concentration of $2.5 \cdot 10^4$ molecule cm^{-3}, which would decrease the estimated diurnal net ozone production rates by roughly 0.2 ppb_v day^{-1} over the Arabian Sea and at most 0.6 ppb_v day^{-1} over the other regions, which does not substantially alter the here presented results. The noontime chemical ozone loss rate can be summarized by

$$L(O_3) = [O_3] \cdot \left(\alpha \cdot j(O^1D) + k_{OH+O_3} \cdot [OH] + k_{HO_2+O_3} \cdot [HO_2]\right). \quad (6)$$

NOPR presented in this study is finally calculated as the difference of Eq. 4 and Eq. 6.

$$NOPR = k_{NO+RO_2}[NO][RO_2] - [O_3] \cdot (\alpha \cdot j(O^1D) + k_{OH+O_3}[OH] + k_{HO_2+O_3}[HO_2]). \quad (7)$$

Under the assumption of constant chemical composition for a given day, the NOPR is expected to have a diel cycle following the measured actinic flux. Hence integrating the estimated NOPR over the course of a day based on the particular fractional noontime integral of $j(NO_2)$ will yield a diurnal value for NOPR. A detailed calculation of the diurnal fractional integrals is given in the supplementary Figure S1. Note that all reaction rate constants used are from the IUPAC Task Force on Atmospheric Chemistry Chemical Kinetic Data Evaluation (Atkinson et al., 2004). Indications whether a chemical regime is NO_x-limited or VOC-limited can be derived from the ratio of HCHO to NO_2. Former studies have derived HCHO/NO_2-

ratios from satellite measurements to establish whether ozone production is NO_x-limited or VOCs-limited. The results indicate NO_x-limitation for $HCHO/NO_2 > 2$ and prevailing VOC-limitation for $HCHO/NO_2 < 1$(Duncan et al., 2010).

2.5 ECHAM/MESSy Atmospheric Chemistry (EMAC) model

EMAC is a 3D general circulation model that includes a variety of sub-models to describe numerous processes in the troposphere, their interaction with oceans and land surfaces and incorporates anthropogenic influences. Here we use the second development cycle of the Modular Earth Submodel System (MESSy2) (Jöckel et al., 2010) and ECHAM5 (Röckner et al., 2006) which is the fifth generation European Centre Hamburg general circulation model in the T106L31 resolution (corresponding to a quadratic grid of roughly 1.1° and 1.1°). The model has 31 vertical pressure levels and involves the complex organic chemistry mechanism MOM (Mainz Organic Mechanism) as presented by Sander et al. (2019) that includes further developments of the version used by Lelieveld et al. (2016b). Here we use the lowest pressure level in a terrain following coordinates (equivalent to the surface level) and simulations of NO, NO_2, O_3, OH, HO_2, $j(NO_2)$ and $j(O^1D)$. The sum of peroxy radicals was estimated as the sum of all radicals R_iO_2 with less than four carbon atoms. Net ozone production based on data retrieved from EMAC was estimated as

$$NOPR = [NO] \cdot \left(k_{NO+HO_2}[HO_2] + \sum_i k_{NO+R_iO_2}[R_iO_2]\right) - [O_3] \cdot (\alpha \cdot j(O^1D) + k_{OH+O_3}[OH] + k_{HO_2+O_3}[HO_2]). \quad (8)$$

A list of all included peroxy radicals R_iO_2 for the reaction with NO is given in the supplementary Table ST10.

3 Results and discussions

3.1 NO_x and O_3 in the MBL around the Arabian Peninsula

During AQABA NO_x mixing ratios varied over five orders of magnitude with lowest values of less than 50 ppt_v observed in relatively pristine regions and highest values of several hundred ppb_v found in the vicinity of megacities or nearby passing ships. Ozone mixing ratios ranged from values of less than 20 ppb_v, detected over the Arabian Sea, to more than 150 ppb_v during episodes of severe pollution. Figures 3a) and 3b) show distributions of NO_x measured during the first and second leg of the campaign (range from 0.1 ppb_v to 20 ppb_v) while Figure 3c) and 3d) show corresponding ozone mixing ratios covering a range from 20 ppb_v to 100 ppb_v, respectively. A classification of the different regions based on Box-Whisker-Plots, including the 25-75-percentile interval (box) and whiskers for the 10-90-percentile interval, is shown in Figure 4 and Figure 5 for NO_x and O_3, respectively. As average NO_x is often influenced by fresh, localized emissions, we have included the median (black bar) instead of the average in the Box-Whisker-Plot for NO_x, which is less sensitive to extreme values. For O_3, although the difference between median and mean is mostly negligible, we also use the median in Figure 5. NO_x and O_3 averages, medians, standard deviations, 1st and 3rd quantiles and the number of data points quantified per region are given in the supplementary Table ST3. See supplementary Figure S4 for OH and preliminary HO_2 mixing ratios around the Arabian Peninsula. Supplementary Figure S5 shows the variation of the absolute humidity around the Arabian Peninsula.

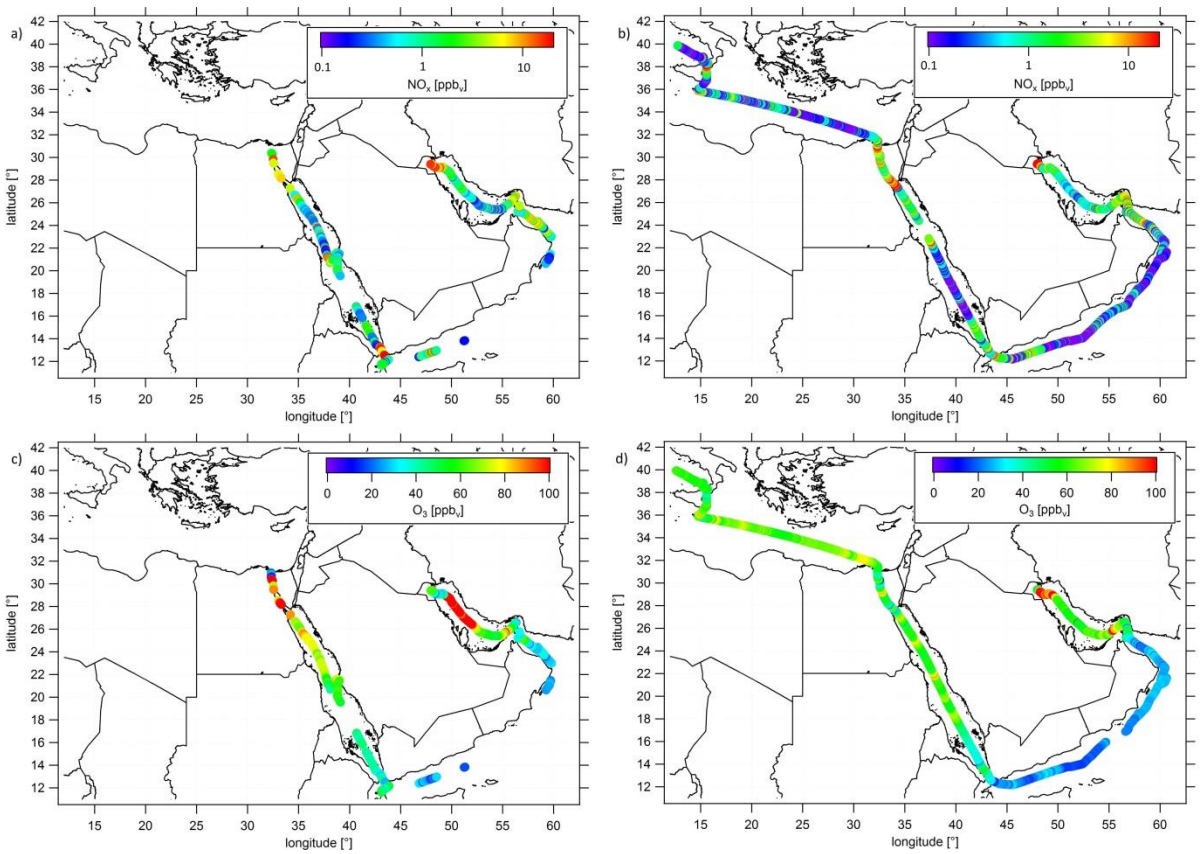

Figure 3: Ship cruises with color-scaled NO_x mixing ratios (logarithmic scale) a) during the first and b) the second leg and color-scaled O_3 mixing ratios (linear scale) c) during the first and d) during the second leg. Note that both NO_x and O_3 has been filtered for own stack contamination.

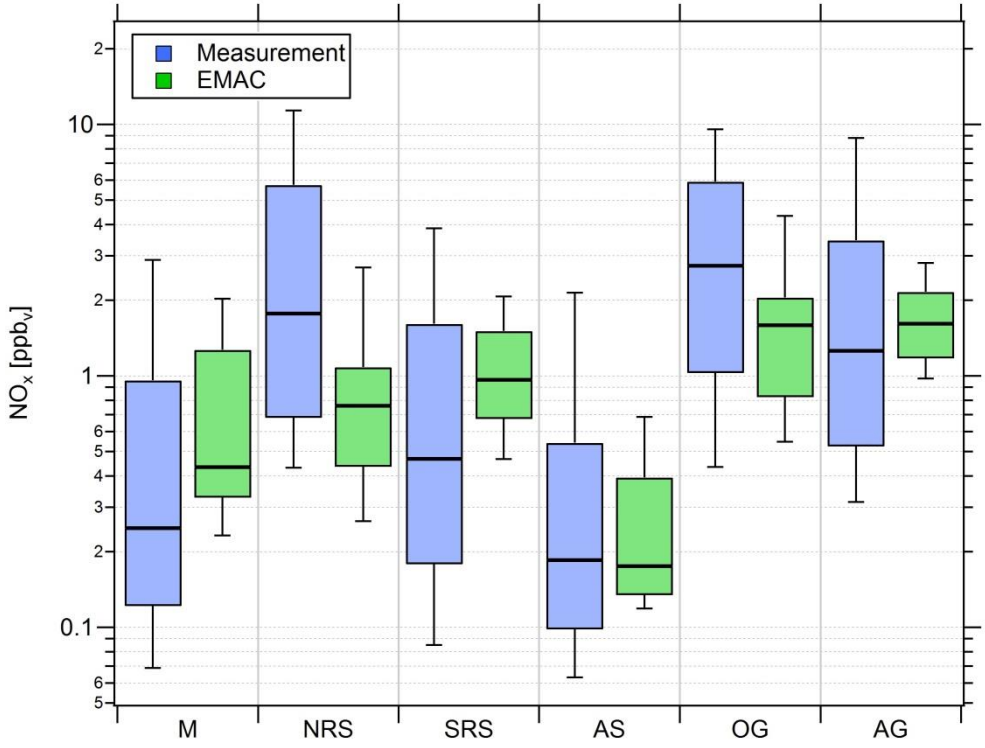

Figure 4: Comparison of measured (blue) and simulated (green) NO_x mixing ratios in the six different regions investigated during AQABA. The horizontal black bar indicates the median value, the box the 25- and 75-percentiles and the whiskers the 10- and 90-percentiles.

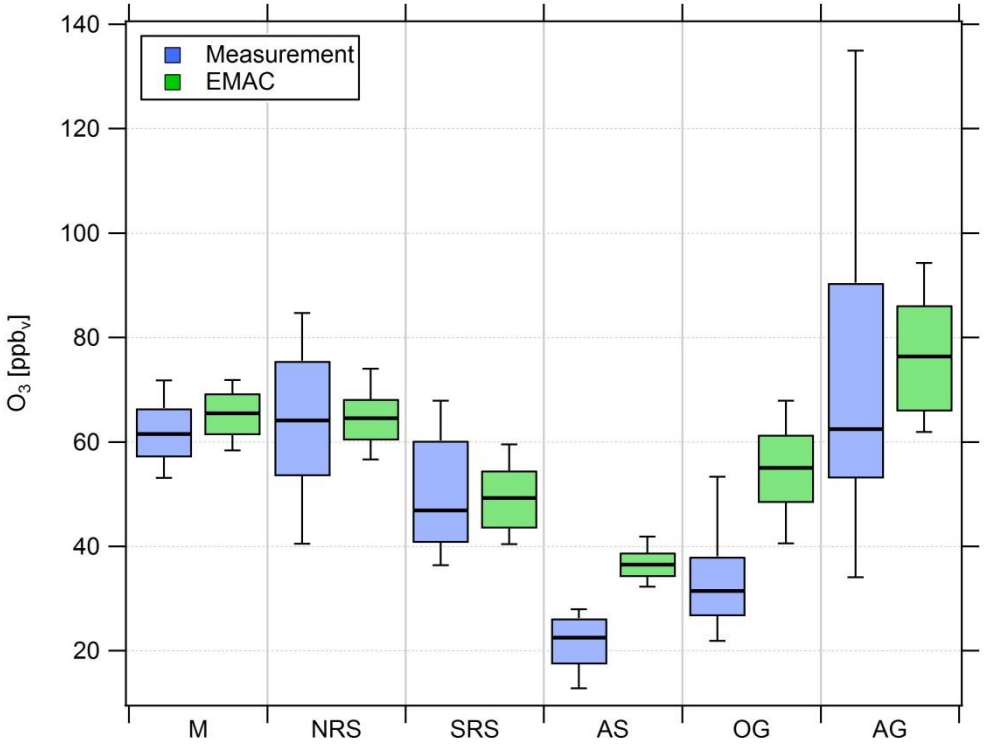

Figure 5: Comparison of measured (blue) and simulated (green) O_3 mixing ratios in the six different regions investigated during AQABA. The horizontal black bar indicates the median value, the box the 25- and 75-percentiles and the whiskers the 10- and 90-percentiles.

Overall, we find that NO_x mixing ratios over the Northern Red Sea, the Gulf of Oman and the Arabian Gulf are approximately one order of magnitude higher than in the other three regions (Southern Red Sea, Arabian Sea, Mediterranean). NO_x medians over the Arabian Gulf, the Northern Red Sea and the Gulf of Oman are 1.26 ppb_v, 1.76 ppb_v and 2.74 ppb_v, respectively. Lower median NO_x mixing ratios were measured over the Southern Red Sea (0.46 ppb_v), the Mediterranean (0.25 ppb_v) and the Arabian Sea (0.19 ppb_v). With respect to observed O_3 mixing ratios, the Arabian Sea is the only region representing remote MBL conditions with lowest median and average O_3 of 21.5 ppb_v and 22.5 ppb_v respectively, followed by the Gulf of Oman where median and mean O_3 were 31.5 ppb_v and 34 ppb_v, respectively. The low O_3 mixing ratios over the Arabian Sea were accompanied by the smallest variability (whisker-interval: 15.1 ppb_v). Although observing highest NO_x over the Oman Gulf, O_3 observed over the Oman Gulf was amongst the lowest detected throughout the whole campaign, which can be partly explained by the fact that high NO_x lead to low ozone production or even net ozone destruction. However, a significantly larger whisker-interval of observed ozone of 31.4 ppb_v over the Gulf of Oman indicates increasing amounts of pollution and advection from the Arabian Gulf where extreme events of ozone were observed several times during the campaign with maximum mixing ratios of up to 170 ppb_v when wind was coming from Kuwait/Iraq. Please note that during the second leg wind was coming from Iran (Pfannerstill et al., 2019). The whisker-interval over the Arabian

Gulf was 100.9 ppb_v, more than six times higher than that over the Arabian Sea. Reasons for large variations of both NO_x and O_3 over the Arabian Gulf were a multitude of point sources as well as a change in the observed wind direction with air masses coming from Iraq/Kuwait area during the first leg and air masses coming from Iran during the second leg (Pfannerstill et al., 2019). Over the Mediterranean, the Northern Red Sea and the Southern Red Sea, median ozone was 61.5 ppb_v, 64.2 ppb_v and 46.9 ppb_v, respectively. The whisker-intervals over the Northern Red Sea and the Southern Red Sea were 44.2 ppb_v and 31.6 ppb_v, respectively. Air masses over the Mediterranean were characterized as photochemically aged due to their impact by northerly winds (Etesians) which bring processed/oxidized air from eastern Europe (Turkey, Greece) to the Mediterranean area (Derstroff et al., 2017; Pfannerstill et al., 2019). This photochemical ageing/oxidation over the Mediterranean leads to a rather small whisker-interval of 18.7 ppb_v in ozone. In summary, median NO_x over the Oman Gulf was 56 % and 117 % higher than over the Northern Red Sea and the Arabian Gulf, respectively. However, the highest NO_x average was measured over the Northern Red Sea at 4.69 ppb_v, similar to the values observed over the Oman Gulf (4.16 ppb_v) and the Arabian Gulf (3.65 ppb_v). Note that highest NO_x mixing ratios over the Oman Gulf and over the Northern Red Sea are not always associated with high O_3 mixing ratios. We find that average ozone was highest over the Arabian Gulf with 74 ppb_v followed by the Northern Red Sea region (63.4 ppb_v). The average ozone mixing ratio over the Oman Gulf was 34 ppb_v, which corresponds to 46 % of the value observed over the Arabian Gulf. Photochemically aged air masses over the Mediterranean Basin show an ozone average of 61.6 ppb_v and air masses encountered over the Northern Red Sea (O_3 median of 64.2 ppb_v, O_3 average of 63.4 ppb_v) are comparable to the Arabian Gulf.

Due to a number of large pollution sources in the region around the Arabian Peninsula such as passing ships, highly urbanized areas as well as on- and off-shore petrochemical processing, NO_x levels were rarely as low as those found in remote locations such as over the South Atlantic (Fischer et al., 2015) where NO_x levels may be under 20 ppt_v. Apart for a few occasions where NO_x was below 50 ppt_v for short periods (Arabian Sea, the Southern Red Sea and the Mediterranean), NO_x levels during AQABA generally ranged from 100 ppt_v up to several ppb_v. The campaign NO_x median of 0.65 ppb_v and mean value of (2.51 ± 5.84) ppb_v is comparable to urban sites (Kleinman et al., 2005). A detailed emission density analysis performed by Johansson et al. (2017) shows that NO_x emissions on and around the Arabian Peninsula are amongst the highest worldwide, which could explain the rather high NO_x level in the MBL around the peninsula (Johansson et al., 2017; Pfannerstill et al., 2019). O_3 mixing ratios measured during AQABA were also very variable with O_3 mixing ratios ranging between less than 20 ppb_v in the remote MBL (Fischer et al., 2015) to 60-70 ppb_v in the Mediterranean (consistent with previous ship-based measurements in the region (Kouvarakis et al., 2002) and as high as 150 ppb_v measured over the Arabian Gulf region. The latter are consistent with O_3 mixing ratios reported from regions influenced by oil and gas processing (Pfannerstill et al., 2019) and shipping lanes such as the Houston Ship Channel (Mazzuca et al., 2016).

Figure 4 also shows that the general trend for NO_x mixing ratios in the different regions is widely reproduced by the EMAC model. We find that the median NO_x(model)/NO_x(measurement)-ratio of all five minute averaged data points of the whole

campaign is 0.91, indicating that the model underestimates NO_x by roughly 10 %. The average ratio and its standard deviation are significantly larger at 2.57 and 5.71, respectively, indicating that single modeled data points strongly exceed the measurements, especially during periods of low in situ NO_x (see supplementary Figure S6). Particularly over the Arabian Sea and the Southern Red Sea, the model generally simulates NO_x mixing ratios higher than 100 and 200 ppt_v, respectively while the measurements indicate mixing ratios of less than 50 ppt_v for certain periods. Furthermore, as expected, the model is not able to reproduce point sources such as passing ships for which we observe a significant underestimation of the measured NO_x. For ozone we find that the median O_3(model)/O_3(measurement)-ratio throughout the campaign is 1.23, indicating that over the course of the campaign the model overestimates O_3 by about 23 %. This could partly be related to the same limitation, i.e. the inability of the model to resolve point sources in which O_3 is locally reduced due to titration by NO. While the model is in rather good agreement with the measurements over the Mediterranean, the Northern Red Sea and Southern Red Sea, large deviations are found over the Arabian Sea and the Oman Gulf, where the model overestimation with respect to the regional median is 63 % and 75 %, respectively. A possible explanation for the overestimation of both ozone and NO_x in pristine regions such as over the Arabian Sea and the Oman Gulf could be related to the model resolution of 1.1° x 1.1°. Interpolation of model simulations along the *Kommandor Iona* ship track close to the coast at this resolution will most likely incorporate contributions from nearby land areas, affected by anthropogenic emissions. See supplementary Table ST3 and Table ST4 for further information and Figure S6 and S7 for additional scatterplots of measured and simulated regional median NO_x and O_3, respectively.

3.2 Estimation of RO_2 around the Arabian Peninsula

Noontime RO_2 was estimated based on Eq. 3. As the steady state assumption will not hold for air masses originating from fresh emissions (times to acquire steady state estimated from the inverse sum of the loss and production terms for NO_2 typically ranged from 1-2 minutes during AQABA) and for fast changes in the actinic flux, we have calculated Box-Whisker-Plots for $\pm$ 2 h around noontime for which we expect relatively minor changes in the actinic flux (Figure 6). The noontime of each day was approximated by applying a Gaussian fit routine to the measured $j(NO_2)$ values whereas $j(NO_2)$ values being less than 10^{-3} s^{-1} were neglected. Due to the availability of OH and HO_2 data from 18 July 2017 onwards, we have limited the analysis to this period. Note that there are no noontime RO_2 estimates from 18 July to 21 July due to contamination by the ship exhaust and on 24 August 2017 due to missing data. The black bar in Figure 6 indicates the median value, with the Box-interval marking the 25- and 75-percentile and the whisker showing the 10- and 90-percentile. Figure 7 shows summarized regional trends of the RO_2 estimates for measured and simulated data.

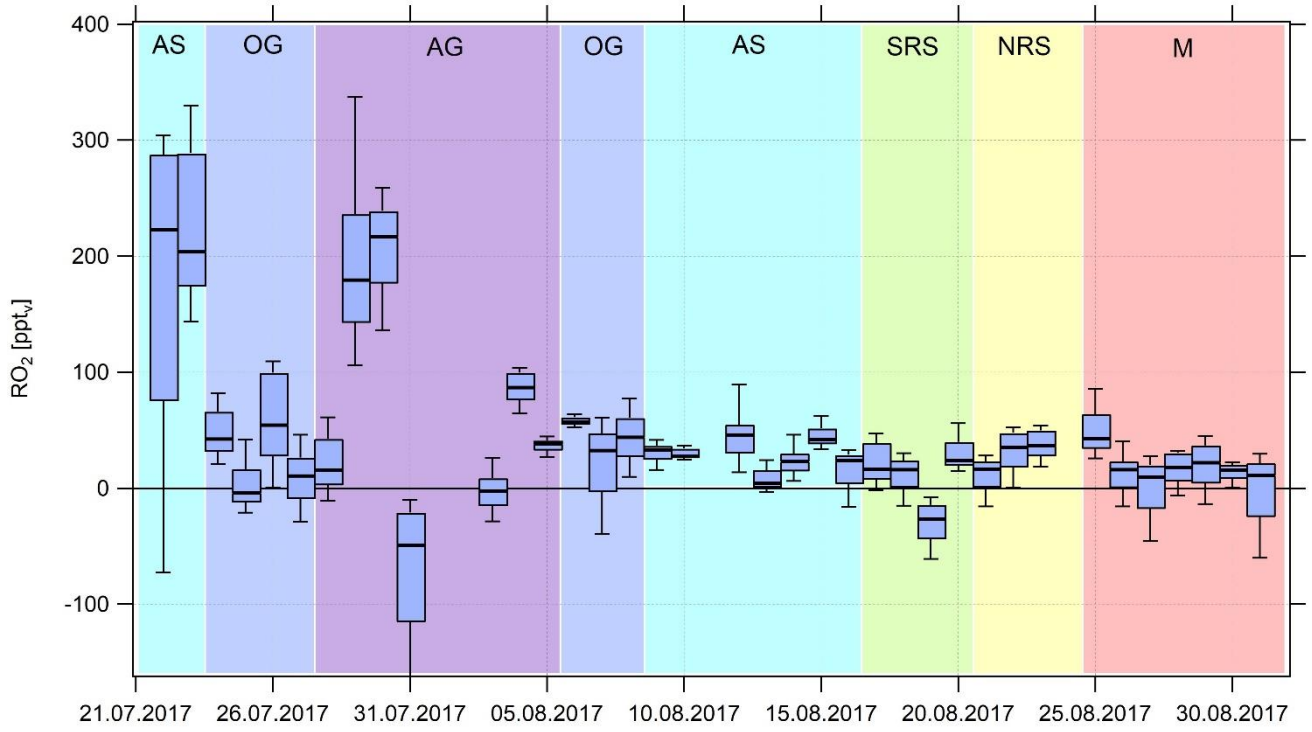

425 **Figure 6: Timeline of median RO_2 noontime estimates from 22 July to 31 August 2017. Due to contamination by the ship exhaust itself, there is no data from 18 July to 21 July 2017. See annotations for the classification of the different regions.**

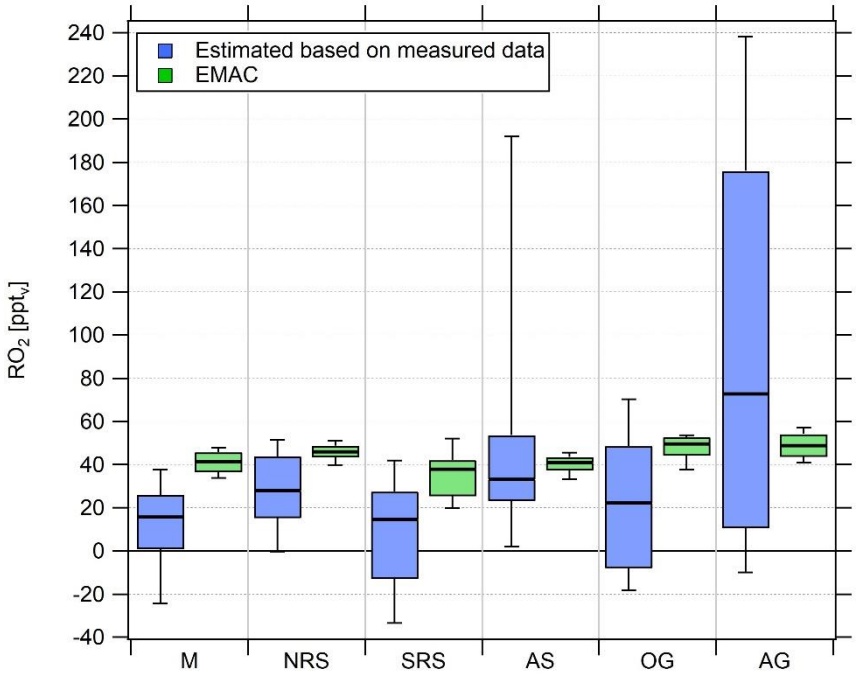

Figure 7: Comparison of Box-Whisker-Plots of the regional estimated noontime RO_2 median based on estimated and simulated data for the period from 18 July 2017 onwards.

We find median noontime RO_2 mixing ratios over the Mediterranean, the Northern Red Sea, the Southern Red Sea, the Arabian Sea and Oman Gulf of 16 ppt_v, 28 ppt_v, 15 ppt_v, 33 ppt_v and 22 ppt_v, respectively, with each respective 75-percentile RO_2 being equal or less than 54 ppt_v. Based on the total measurement uncertainties of the measured quantities in Eq. 3, the uncertainty in RO_2 is estimated by means of the largest error possible at 15 %.

$$\Delta RO_2 = \sqrt{\Delta NO^2 + \Delta NO_2^2 + \Delta O_3^2 + \Delta j(NO_2)^2} = \sqrt{6\%^2 + 9\%^2 + 2\%^2 + 10\%^2} \approx 15\ \%$$

Note that our calculation assumes that errors in the used rate coefficients are negligible. Only over the Arabian Gulf, the RO_2 estimate yields a median noontime mixing ratio of 73 ppt_v accompanied by the largest variations in the box-interval of the whole campaign. While the box-interval of the RO_2 estimate in the other regions is 25-57 ppt_v, the box-interval over the Arabian Gulf is significantly higher at 165 ppt_v. Negative values for all regions are regularly found in the vicinity of fresh emissions and air masses not in photochemical equilibrium. The elevated 90-percentile over the Arabian Sea is due to high RO_2 estimates during the first leg on 22 and 23 July.

Estimated RO_2 mixing ratios based on measured tracer data are in general agreement with previous studies performed in marine boundary layer environments which report maximum mixing ratios between 30 and 55 ppt_v around noontime

(Hernandez et al., 2001). As peroxy radicals are short-lived molecules generated from the oxidation of VOCs, enhanced RO_2 concentrations observed over the Arabian Gulf are most likely due to high VOC emissions from intense oil and gas activities in the region (Bourtsoukidis et al., 2019; Pfannerstill et al., 2019). However high HO_2 and RO_2 can also occur in aged air masses with low NO_x and VOCs but still significant O_3 (and perhaps HCHO whose photolysis would then yield peroxy radicals). Bourtsoukidis et al. report that spatial volume mixing ratios of ethane and propane over the Arabian Gulf were about a factor of 10-15 times higher than over the Arabian Sea and the Southern Red Sea (Bourtsoukidis et al., 2019). We find that the median noontime RO_2(measurement estimate)/HO_2(measurement)-ratio throughout the whole campaign is 1.88. Note that during single days, HO_2 may be higher than the RO_2 estimate, which is within the uncertainty of the RO_2 estimate.

EMAC modelled, median noontime RO_2 mixing ratios estimated as the sum of simulated HO_2 and all simulated peroxy radicals with less than four carbon molecules are 41 ppt_v, 46 ppt_v, 38 ppt_v, 41 ppt_v, 50 ppt_v and 49 ppt_v over the Mediterranean, the Northern Red Sea, the Southern Red Sea, the Arabian Sea, the Oman Gulf and the Arabian Gulf, respectively. The observation based RO_2 estimate yields 16 ppt_v, 28 ppt_v, 15 ppt_v, 33 ppt_v, 22 ppt_v and 73 ppt_v respectively. We find that the median point by point RO_2(model)/RO_2(measurement estimate)-ratio from 18 July onward is 1.05 so that, on average, the model overestimates the measurement by 5 %. Please note that the observational variability is much higher than the modeled one and that the median of 1.05 is accompanied by a larger average (1.84) and a large variability (42.51). See supplementary Table ST5 and ST6 for further information and Figure S8 for an additional scatterplot of measured and simulated regional median RO_2.

3.3 Net ozone production rates around the Arabian Peninsula

In the following, net ozone production rates (at noon) are calculated based on Eq. 7 for the different regions. These noontime values are scaled to diurnal production rates (Figure 8). As photochemical net ozone destruction is in good approximation linear with actinic flux $j(NO_2)$ and as on average (46.1 $\pm$ 2.8) % of the total $j(NO_2)$ occurred $\pm$ 2h around noon, the median noontime NOPR estimate was multiplied by 4/0.461 $\approx$ 8.68 to obtain a diurnal value. The error in the total actinic flux located $\pm$ 2h around noon is estimated from the standard deviation of the best estimate of 0.461 at $\Delta s \approx 6$ %. Due to contamination by the own ship exhaust and due to the availability of OH and HO_2 data only from 18 July 2017 onwards, we have limited the analysis to the period from 22 July 2017 to 31 August 2017. A comparison of NOPR estimated based on measured and simulated data for the different regions is shown in Figure 9. A break-down of the different terms of Eq. 7 in the six regions is included in the supplementary Figures S10-S13.

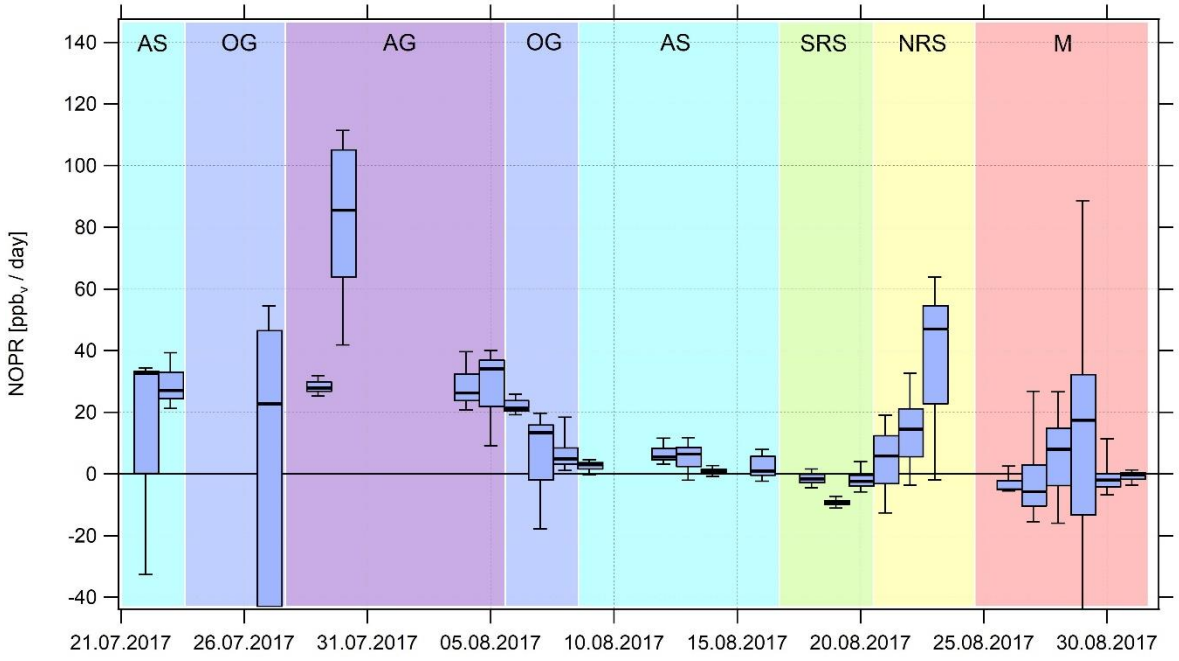

Figure 8: Timeline of the diurnal NOPR from 22 July to 31 August 2017. NOPR calculations are limited to the time period from 22 July onwards due to missing HO_x data and contamination by the ship exhaust itself before this period. See annotations for the classification of the different regions.

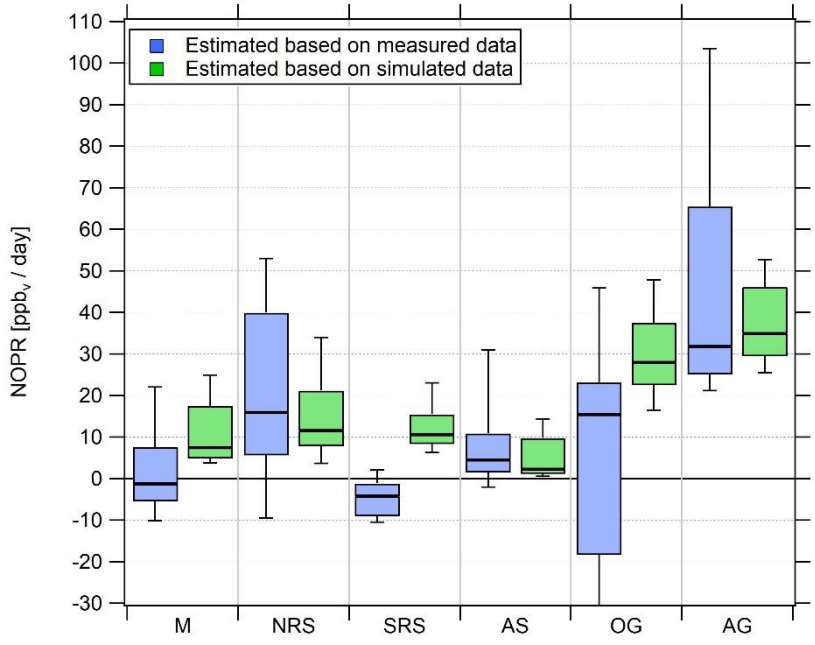

Figure 9: Diurnal net ozone production rates in the different regions. Related to the magnitude of pollution sources, the lower whisker of the NOPR estimate over the Oman Gulf is -324 ppb day^{-1}.

Over the Mediterranean and the Southern Red Sea, NOPR values do not significantly deviate from zero (production equals loss) within the atmospheric variability. Based on the total measurement uncertainties of the measured quantities in Eq. 3, the systematic error in NOPR is estimated from error propagation by means of the largest error possible at 38 %.

$$\Delta NOPR = \sqrt{\Delta NO^2 + \Delta NO_2^2 + \Delta O_3^2 + \Delta j(NO_2)^2 + \Delta j(O^1D)^2 + \Delta \alpha^2 + \Delta RO_2^2 + \Delta OH^2 + \Delta HO_2^2 + \Delta s^2}$$

$$= \sqrt{6\%^2 + 9\%^2 + 2\%^2 + 10\%^2 + 10\%^2 + 5\%^2 + 15\%^2 + 20\%^2 + 21\%^2 + 6\%^2} \approx 38\ \%. \quad (485)$$

The best estimate indicates slight net ozone destruction for the Mediterranean and Southern Red Sea (- 1 ppb day^{-1}) and (- 4 ppb day^{-1}) respectively, and slight net production for the Arabian Sea (5 ppb day^{-1}), which is significantly positive within the variability of the box-interval. Variations in NOPR calculated as the width of the 25-75-percentile-box yield comparable values of 9-11 ppb day^{-1} for these three regions. Substantial net ozone production was inferred over the Oman Gulf, the Northern Red Sea, and the Arabian Gulf with the respective median values being 16 ppb day^{-1}, 16 ppb day^{-1} and 32 ppb day^{-1}, respectively. Especially over the Red Sea we find a strong latitudinal gradient in net ozone production rates with higher values towards the northern end, while slight net ozone destruction of -4 ppb day^{-1} is reported over the southern part.

NOPR estimates for the Oman Gulf, the Northern Red Sea and the Arabian Gulf are comparable to results reported for dense traffic shipping routes such as the Houston Ship Channel with NOPR of a few tens of ppb h^{-1} for periods of severe pollution (Zhou et al., 2014). Similar net ozone production rates have been reported for regions of Beijing in summer 2006 (Lu et al., 2010). For regions with low anthropogenic influence such as the Southern Red Sea and the Arabian Sea we estimate net ozone production that does not differ significantly from zero. This is due to the rather low NO_x mixing ratios in the clean marine boundary layer (Bozem et al., 2017). Note that we calculated net ozone destruction only for a few days over the Southern Red Sea and the Arabian Sea, indicating that the marine boundary layer around the Arabian Peninsula is rarely free from anthropogenic influence owing to the multitude of on- and off-shore anthropogenic activities.

We find that model-calculated estimates of NOPR reproduce the trends observed for NOPR calculated from in situ measurements except over the Mediterranean and the Southern Red Sea. Although EMAC predicts high ozone levels over the Arabian Sea, it also reports the lowest NOPR in this region. On the other side, the large overestimation of the model-calculated estimate NOPR against the one based on measured tracer data over the Mediterranean and over the Southern Red Sea could be linked to NO_x being overestimated in the model in these regions. In the model, pollution emissions, especially over the Oman Gulf and the Arabian Gulf, seem to be averaged over a large (1.1° grid size) region. High background concentrations of ozone precursors hence contribute to net ozone production rates that compare to conditions observed in the Houston case (Zhou et al., 2014). Even in the more pristine regions such as over the Southern Red Sea and the Arabian Sea, the model is not able to reproduce net ozone destruction, which is consistent with the fact the ozone is generally too high and

that NO_x levels below 0.1 ppb_v are not found in the model. See supplementary Table ST7 and ST8 for further information and supplementary Figure S9 for an additional scatterplot of measured and simulated regional NOPR.

3.4 VOC- and NO_x-sensitivity

Ozone is photochemically formed when the precursors NO_x and VOCs are abundant in the presence of sunlight (Bozem et al., 2017; Jaffe et al., 2018). In order to determine whether a chemical system is NO_x- or VOC-limited or in a transition between those two regimes, one has to estimate the total amount of OH reactivity towards VOCs and towards NO_x. Therefore the VOC/NO_x-ratio is an important indicator of the behavior of NO_x, VOCs and O_3 in a system. Since it is not feasible to precisely define all ambient VOCs (could be thousands), formaldehyde mixing ratios have been used as a proxy for the OH reactivity towards VOCs since it is a short-lived oxidation product of many VOCs that is often positively correlated with peroxy radicals (Sillman et al., 1995; Duncan et al., 2010). Sillman et al. first used afternoon concentrations of indicator species such as HCHO and total reactive nitrogen (NO_y) to determine the sensitivity of ozone production to VOCs or NO_x (Sillman et al., 1995). Their approach was later successfully transferred to space-based satellite observations by using the ratio of tropospheric columns of HCHO and NO_2 to determine the sensitivity of ozone production (Martin et al., 2004). Here we use HCHO/NO_2-ratios (referred to as "Ratio") deduced by Duncan et al. as indicators for the sensitivity of ozone production to NO_x- and VOC-limitations in megacities in the United States with large amounts of anthropogenic NO_x and VOC emissions (Duncan et al., 2010). The Ratio is an indicator of surface photochemistry as most of the atmospheric column of HCHO and NO_2 is located in the planetary boundary layer (Duncan et al., 2010). Duncan et al. have derived NO_x-limited ozone production regimes for HCHO/NO_2 > 2 and VOC-limited ozone production for HCHO/NO_2 < 1 (Duncan et al., 2010). For 1 < HCHO/NO_2 < 2 both NO_x and VOC emission reductions may lead to a reduction in ozone. Figure 10 shows the Box-Whisker-Plot classification of the HCHO/NO_2-ratio of the different regions during noontime.

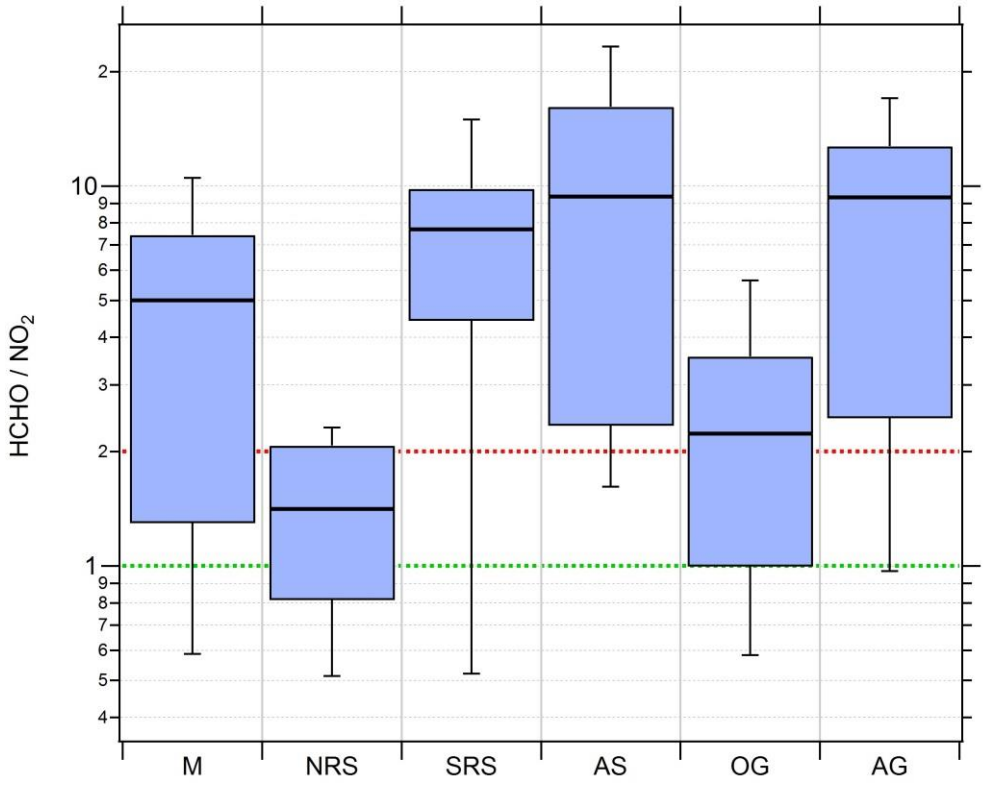

Figure 10: Box-Whisker-Plots of the HCHO/NO_2-ratio for the different regions with the black bar indicating the median value. Red (ratio = 2) and green (ratio = 1) lines indicate the limits for HCHO/NO_2 deduced by Duncan et al. (2010) for NO_x-limitation and VOC-limitation, respectively.

Median HCHO/NO_2-ratios of 5, 7.7, 9.4 and 9.3 over the Mediterranean, the Southern Red Sea, the Arabian Sea and the Arabian Gulf respectively indicate tendencies towards NO_x-limited regimes. In a previous study based on measured OH reactivity, Pfannerstill et al. classified these regions as being mostly in a transition between NO_x- and VOC-limitation, with a tendency towards NO_x-limitation (2019). Median HCHO/NO_2-ratios of 1.4 and 2.2 estimated over the Northern Red Sea and the Oman Gulf signify tendencies towards VOC-limitation. However, none of the medians of the six regions falls below the VOC-limit deduced by Duncan et al. (2010).

Over the Red Sea we find a latitudinal gradient in the HCHO/NO_2-ratio, similar to the gradients for NO_x and NOPR. Due to very low NO_x over the Southern Red Sea, O_3 production is NO_x-limited, changing into a more VOC-limited regime over the Northern Red Sea. Ozone production over the Mediterranean was classified as rather NO_x-limited, however partly being in the transition regime between NO_x- and VOC-limitation., which can be explained by measurements obtained on 29 August 2017 when laying at anchor in front of Malta with a multitude of (NO_x)-emissions from nearby situated vessels. Average noontime NO_x on that particular day was about three times as large as the regional average noontime NO_x observed over the

whole Mediterranean area. NO_x limitation is also inferred for the relatively clean Arabian Sea and the polluted Arabian Gulf atmosphere. Note that a further increase in NO_x-emissions from increased shipping in the Arabian Gulf may initially lead to higher ozone production. However, a further increase in NO_x might eventually lead to a change from NO_x- to VOC-sensitivity and a decrease in ozone production for this region, as observed for the Oman Gulf (median $HCHO/NO_2$-ratio of 2.2 and average O_3 of 34 ppb_v). See supplementary Table ST9 for detailed statistics on regional $HCHO/NO_2$-ratios.

4 Conclusion

In situ observations of NO, NO_2, O_3, HCHO, OH, HO_2, absolute humidity, actinic flux, temperature and pressure were carried out in the marine boundary layer around the Arabian Peninsula during the AQABA ship campaign from late June to early September 2017. Concentration ranges of both NO_x and O_3 clearly showed anthropogenic influence in the MBL. NO_x was highest over the Arabian Gulf, the Northern Red Sea and the Oman Gulf. Lowest NO_x was observed over the Arabian Sea and over the Southern Red Sea during the second leg. O_3 mixing ratios were highest over the Arabian Gulf. We observed a latitudinal gradient in O_3 concentrations with higher values towards the northern part of the Red Sea. Although comparable O_3 averages were measured over the Northern Red Sea and over the Mediterranean, lower variability over the Mediterranean towards the end of August 2017 indicates photochemically more extensively aged air masses. The lowest regional O_3 mixing ratio average was detected over the Arabian Sea, which is broadly comparable to remote marine boundary layer conditions in the Northern Hemisphere.

Noontime RO_2 estimates based on deviations from the Leighton Ratio yield median values around the Arabian Peninsula amount to 15 – 33 ppt_v for all regions except over the Arabian Gulf where the median is 73 ppt_v. The uncertainty due to the missing up-welling actinic flux portion is expected to be insignificant. Furthermore, we estimated noontime and diurnal NOPR based on Eq. 6 and the integral over the actinic flux. Highest diurnal NOPR were observed over the Oman Gulf, the Northern Red Sea and the Arabian Gulf with median values of 16 $ppb_v\ day^{-1}$, 16 $ppb_v\ day^{-1}$ and 32 $ppb_v\ day^{-1}$, respectively, which is in agreement with previous studies that predicted net photochemical O_3 formation conditions in the region. Net ozone destruction was only observed for a few days with clean conditions over the Arabian Sea and the Southern Red Sea. Based on $HCHO/NO_2$-ratios our analysis suggests tendencies towards NO_x-limitation over the Mediterranean, the Southern Red Sea, the Arabian Sea and the Arabian Gulf and VOC-limitation over the Northern Red Sea and the Oman Gulf, which reproduces the trends observed by Pfannerstill et al. (2019).

NO_x results from the atmospheric chemistry – general circulation model EMAC underestimate the measurement data by 10 % whereas median modeled O_3 overestimates the measurement by 23 %, the latter being related to limitations in model resolution in coastal proximity and near shipping lanes. Although EMAC generally reproduces regional NO_x and O_3 medians, the scatter when comparing both data sets is large. NO_x is generally too low as it does not resolve local point

sources and too high for clean regions. Lowest NO_x of less than 0.1 ppb_v found in the in situ measurements is not reproduced by the model as emissions are averaged over a large area (1.1°). Median noontime RO_2 retrieved from the EMAC model are ~ 5 % higher than RO_2 estimates based on measurement data, however, the RO_2 sum deduced from EMAC is sometimes about a factor of 2 higher than the regional RO_2 estimate based on the Leighton Ratio and measured tracer data. NOPR estimates based on modeled data reproduce the tendencies derived from the measurements very well. However, the model does not reproduce observed net ozone destruction along some clean parts of the ship cruise.

Data availability

Data used in this study is available to all scientists agreeing to the AQABA protocol at https://doi.org/10.5281/zenodo.3693988.

Author contributions

IT, HF and JL designed the study. UP and IT performed the CLD NO and NO_2 measurements and processed the data. JC and PE performed the O_3 measurements, JS performed the actinic flux measurements. JS performed cavity ring-down spectroscopy measurements of NO_2. DD and BH performed the HCHO measurements. HH, MM, RR, ST performed the OH and HO_2 measurements. J-DP was responsible for the H_2O measurements. Model simulations were made by AP. All authors have contributed to writing this manuscript

Competing interests

The authors declare no conflict of interest.

Acknowledgements

We acknowledge the collaborations with King Abdullah University of Science and Technology (KAUST), The Cyprus Institute (CyI) and the Kuwait Institute for Scientific Research (KISR). We would like to thank Marcel Dorf and Claus Koeppel for the organization of the campaign. We would like to thank Hays Ships Ltd. and the ship crew for caring about the physical well-being of the scientific participants and for an unforgettable time on board *Kommandor Iona*. Last but not least we would like to thank the whole AQABA community for a successful campaign.

Appendix: Acronyms and abbreviations

General

AQABA	**A**ir **Q**uality and Climate in the **A**rabian **Ba**sin campaign
CyI	The **Cy**prus **I**nstitute
KAUST	**K**ing **A**bdullah **U**niversity of **S**cience and **T**echnology
KISR	**K**uwait **I**nstitute for **S**cientific **R**esearch

Regions

AG	**A**rabian **G**ulf
AS	**A**rabian **S**ea
M	**M**editerranean Sea
NRS	**N**orthern **R**ed **S**ea
OG	**O**man **G**ulf
SRS	**S**outhern **R**ed **S**ea

Scientific

CLD	**C**hemi**l**uminescence **d**etector
CRDS	**C**avity **r**ing-**d**own **s**pectroscopy
ECHAM5	Fifth generation **E**uropean **C**entre **Ham**burg general circulation model
EMAC	**E**CHAM/**M**ESSy **A**tmospheric **C**hemistry model
FWHM	**F**ull **w**idth at **h**alf **m**aximum
GC-FID	**G**as **c**hromatography – **f**lame **i**onization **d**etector
HORUS	**H**ydr**O**xyl **R**adical measurement **U**nit based on fluorescence **S**pectroscopy instrument
HO_x	$OH + HO_2$
LED	**L**ight **e**mitting **d**iode
LIF	**L**aser **i**nduced **f**luorescence
MBL	**M**arine **b**oundary **l**ayer
MESSy	**M**odular **E**arth **S**ubmodel **Sy**stem
NOPR	**N**et **o**zone **p**roduction **r**ate
NO_x	$NO + NO_2$
PFA	**P**er**f**luoro**a**lkoxy
PSS	**P**hotostationary **s**teady **s**tate
PTFE	**P**oly**t**etra**f**luoro**e**thylene
SLM	**S**tandard **l**iter per **m**inute
STEAM3	**S**hip **T**raffic **E**mission **A**ssessment **M**odel 3
TMU	**T**otal **m**easurement **u**ncertainty
VOC	**V**olatile **o**rganic **c**ompounds
UV	**U**ltra**v**iolet

References

Atkinson, R., Baulch, D. L., Cox, R. A., Crowley, J. N., Hampson, R. F., Hynes, R. G., Jenkin, M. E., Rossi, M. J., and Troe, J.: Atmos. Chem. Phys., 4, 1461, 2004; IUPAC Task Group on Atmospheric Chemical Kinetic Data Evaluation, (http://iupac.pole-ether.fr).

Bourtsoukidis, E., Ernle, L., Crowley, J. N., Lelieveld, J., Paris, J.-D., Pozzer, A., Walter, D., and Williams, J.: Non Methane Hydrocarbon (C2-C8) sources and sinks around the Arabian Peninsula, doi:10.5194/acp-2019-92, 2019.

Bozem, H., Butler, T.M., Lawrence, M. G., Harder, H., Martinez, M., Kubistin, D., Lelieveld, J., and Fischer, H: Chemical processes related to net ozone tendencies in the free troposphere, Atmos. Chem. Phys., 17, 10565-10582, doi:10.5194/acp-17-10565-2017, 2017.

Cantrell, C. A., Shetter, R. E., Calvert, J. G., Eisele, F. L., Williams, E., Baumann, K., William, H. B., Stevens, P. S., Mather, J., H.: Peroxy radicals from photostationary state deviations and steady state calculations during the Tropospheric OH Photochemistry Experiment at Idaho Hill, Colorado, 1993, J. Geophys. Res., 102, 6369-6378, 1997.

Celik, S., Drewnick, F., Fachinger, F., Brooks, J., Darbyshire, E., Paris, J.-D., Eger, P. G., Schuladen, J., Tadic, I., Friedrich, N., Dienhart, D., Crowley, J. N., Harder, H., and Borrmann, S.: Influence of vessel characteristics and atmospheric processes on the gas and particle phase of ship emission plumes measured in the Mediterranean Sea and around the Arabian Peninsula, Atmos-. Chem. Phys. Discuss., https://doi.org/10.5194/acp-2019-859, in review, 2019.

Chen, S., Ren, X., Mao, J., Chen, Z., Brune, W. H., Lefer, B., Rappenglück, B., Flynn, J., Olson, J., Crawford, J. H.: A comparison of chemical mechanisms based on TRAMP-2006 field data, Atmos. Environ., 44, 4116-4125, doi: 10.1016/j.atmosenv.2009.05.027, 2009.

Crutzen, P. J.: Photochemical reactions initiated by and influencing ozone in unpolluted tropospheric air, Tellus, 26, 47–57, doi:10.1111/j.2153-3490.1974.tb01951.x, 1973.

Derstroff B., Hüser, I., Bourtsoukidis, E., Crowley, J. N., Fischer, H., Gromov, S., Harder, H., Janssen, R. H. H., Kesselmeier, J., Lelieveld, J., Mallik, C., Martinez, M., Novelli, A., Parchatka, U., Phillips, G. J., Sander, R., Sauvage, C., Schuladen, J., Stönner, C., Tomsche, L., and Williams, J.: Volatile organic compounds (VOCs) in photochemically aged air from the eastern and western Mediterranean, Atmos. Chem. Phys., 17, 9547-9566, doi:10.5194/acp-17-9547-2017, 2017.

Duncan, B. N., Yoshida, Y., Olson, J. R., Sillman, S., Martin, R. V., Lamsal, L., Hu, Y., Pickering, K. E., Retscher, C., Allen, D. J., Crawford, J. H.: Application of OMI observations to a space-based indicator of NO_x and VOC controls on surface ozone formation, J. Atmos. Env., 44, 2213-2223, doi:10.1016/j.atmosenv.2010.03.010, 2010.

Drummond, J.W., Volz, A., and Ehhalt, D. H.: An optimized chemiluminescence detector for tropospheric NO measurements, J. Atmos. Chem., 2, 287–306, doi:10.1007/BF00051078, 1985.

Fischer, H., Pozzer, A., Schmitt, T., Jöckel, P., Klippel, T., Taraborrelli, D., and Lelieveld, J.: Hydrogen peroxide in the marine boundary layer over the South Atlantic during the OOMPH cruise in March 2007, Atmos. Chem. Phys., 15, 6971-6980, doi:10.5194/acp-15-6971-2015, 2015.

Hauglustaine, D. A., Madronich, S., Ridley, B. A., Walega, J. G., Cantrell, C. A., and Shetter, R. E.: Observed and model-calculated photostationary state at Mauna Loa Observatory during MLOPEX 2, J. Geophys. Res., 101, 14681-14696, doi:10.1029/95JD03612, 1996.

Hens, K., Novelli, A., Martinez, M., Auld, J., Axinte, R., Bohn, B., Fischer, H., Keronen, P., Kubistin, D., Nölscher, A. C., Oswald, R., Paasonen, P., Petäjä, T., Regelin, E., Sander, R., Sinha, V., Sipilä, M., Taraborrelli, D., Tatum Ernest, C., Williams, J., Lelieveld, J., Harder, H.: Observation and modelling of HO_x radicals in a boreal forest, Atmos. Chem. Phys., 14, 8723-8747, doi:10.5194/acp-14-8723-2014, 2014.

Hernandez, M. D. A., Burkert, J., Reichert, L., Stöbener, D., Meyer-Arnek, J., and Burrows, J. P.: Marine boundary layer peroxy radical chemistry during the AEROSOLS99 campaign: Measurements and analysis, J. Geophys. Res., 106, 20833-20846, doi:10.1029/2001JD900113, 2001.

Hollaway, M. J., Arnold, S. R., Challinor, A. J., and Emberson, L. D.: Intercontinental trans-boundary contributions to ozone-induced crop yield losses in the Northern Hemisphere, Biogeosciences, 9, 271-292, doi:10.5194/bg-9-271-2012, 2012.

Hosaynali Beygi, Z., Fischer, H., Harder, H. D., Martinez, M., Sander, R., Williams, J., Brookes, D. M., Monks, P. S., and Lelieveld, J.: Oxidation photochemistry in the Southern Atlantic boundary layer: unexpected deviations of photochemical steady state, Atmos. Chem. Phys., 11, 8497-8513, doi:10.5194/acp-11-8497-8513, 2011.

Jaffe, D. A., Cooper, O. R., Fiore, A. M., Henderson, B. H., Tonnesen, G. S., Russell, A. G., Henze, D. K., Langford, A. O., Lin, M., and Moore, T.: Scientific assessment of background ozone over the U.S.: Implications for air quality management, Elem. Sci. Anth., 6, 56, doi:10.1525/elementa.309, 2018.

Javed, U., Kubistin, D., Martinez, M., Pollmann, J., Rudolf, M., Parchatka, U., Reiffs, A., Thieser, J., Schuster, G., Horbanski, M., Pöhler, D., Crowley, J. N., Fischer, H., Lelieveld, J., and Harder, H.: Laser-induced fluorescence-based detection of atmospheric nitrogen dioxide and comparison of different techniques during the PARADE 2011 field campaign, Atmos. Meas. Tech., 12, 1461-1481, doi:10.5194/amt-12-1461-2019, 2019.

Jöckel, P., Kerkweg A., Pozzer, A., Sander, R., Tost, H., Riede, H., Baumgartner, A., Gromov, S., and Kern, B.: Development of cycle 2 of the Modular Earth Submodel System (MESSy2), Geosci. Model Dev., 3, 717-752, doi:10.5194/gmd-3-717-2010, 2010.

Johansson, L., Jalkanen, J.-P., Kukkonen, J.: Global assessment of shipping emissions in 2015 on a high spatial a temporal resolution, J. Atmos. Env., 167,403-415, doi:10.1016/j.atmosenv.2017.08.042., 2017.

Keller-Rudek, H., Moortgat, G. K., Sander, R., and Sörensen, R.: The MPI-Mainz UV/VIS Spectral Atlas of Gaseous Molecules of Atmospheric Interest, Earth Syst. Sci. Data, 5, 365-373, doi:10.5194/essd-5-365-2013, 2013.

Kleinman, L. I., Daum, P. H., Lee, Y.-N., Nunnermacker, L. J., Springston, S. R. Weinstein-Lloyd, J., and Rudolph, J.: A comparative study of ozone production in five U.S. metropolitan areas, J. Geophys. Res.-Atmos., 110, D02301, doi:10.1029/2004jd005096, 2005.

Klonecki, A. and Levy, H.: Tropospheric chemical ozone tendencies in CO-CH_4-NO_y-H_2O system: Their sensitivity to variations in environmental parameters and their application to a global chemistry transport model study, J. Geophys. Res., 102, 21221–21237, doi:10.1029/97JD01805, 1997.

Kormann, R., Fischer, H., de Reus, M., Lawrence, M., Brühl, Ch., von Kuhlmann, R., Holzinger, R., Williams, J., Lelieveld, J., Warneke, C., de Gouw, J., Heland, J., Ziereis, H., and Schlager, H.: Formaldehyde over the eastern Mediterranean during MINOS: Comparison of airborne in-situ measurements with 3D-model results, Atmos. Chem. Phys., 3, 851-861, doi:10.5194/acp-3-851-2003, 2003.

Kouvarakis, G., Vrekoussis, M., Mihailopoulos, N., Kourtidis, K., Rappenglueck, B., Gerasopoulos, E., and Zerefos, C.: Spatial and temporal variability of tropospheric ozone (O3) in the boundary layer above the Aegean Sea (eastern Mediterranean), J. Geophys. Res., 107, D18, 8137, doi:10.1029/2000JD000081, 2002.

Krotkov, N. A., McLinden, C. A., Li, C., Lamsal, L. N., Celarier, E. A., Marchenko, S. V., Swartz, W. H., Bucsela, E. J., Joiner, J., Duncan, B. N., Boersma, K. F., Veefkind, J. P., Levelt, P. F., Fioletov, V. E., Dickerson, R. R., He, H., Lu, Z., and

Streets, D. G.: Aura OMI observations of regional SO_2 and NO_2 pollution changes from 2005 to 2015, Atmos. Chem. Phys., 16, 4605–4629, doi:10.5194/acp-16-4605-2016, 2016.

Kwok, C. Y., Laurent, O., Guemri, A., Philippon, C., Wastine, B., Rella, C. W., Vuillemin, C., Truong, F., Delmotte, M., Kazan, V., Darding, M., Lebegue, B., Kaiser, C., Xueref-Remy, I., and Ramonet, M.: Comprehensive laboratory and field testing of cavity ring-down spectroscopy analyzers measuring H_2O, CO_2, CH_4 and CO, Atmos. Chem. Phys., 8, 3867-3892, doi:10.5194/amt-8-3867-2015, 2015.

Leighton, P. A.: Photochemistry of air pollution, Phys. Chem., 9, 1961.

Lelieveld. J., Dentener, F. J., Peters, W., and Krol, M. C.: On the role of hydroxyl radicals in the self-cleansing capacity of the troposphere, Atmos. Chem. Phys., 4, 2337-2344, doi:10.5194/acp-4-2337-2004, 2004.

Lelieveld, J., Hoor, P., Jöckel, P., Pozzer, A., Hadjinicolaou, P., Cammas, J.-P., and Beirle, S.: Severe ozone air pollution in the Persian Gulf region, Atmos. Chem. Phys., 9, 1393–1406, doi:10.5194/acp-9-1393-2009, 2009.

Lelieveld, J.: Strongly increasing heat extremes in the Middle East and North Africa (MENA) in the 21st century, Climate Change, 137, 245-260, doi:10.1007/s10584-016-1665-6, 2016a.

Lelieveld, J., Gromov, S., Pozzer, A., and Taraborrelli, D.: Global tropospheric hydroxyl distribution, budget and reactivity, Atmos. Chem. Phys., 16, 12477-12493, doi:10.5194/acp-16-12477-2016, 2016b.

Liu, F., Beirle, S., Zhang, Q., Dörner, S., He, K., and Wagner, T.: NO_x lifetimes and emissions of cities and power plants in polluted background estimated by satellite observations, Atmos. Chem. Phys., 16, 5823-5298, doi:10.5194/acp-16-5283-2016, 2016.

Lu, K., Zhang, Y., Su, H., Brauers, T., Chou, C., Hofzumahaus, A., Liu, S., Kita, K., Kondo, K., Shao, M., Wahner, A., Wang, J., Wang, X., and Zhu, T.: Oxidant (O_3+NO_2) production processes and formation in regimes in Beijing, J. Geophys. Res., 115, D07303, doi:10.1029/2009JD012714, 2010.

Mallik, C., Tomsche, L., Bourtsoukidis, E., Crowley, J. N., Derstroff, B., Fischer, H., Hafermann, S., Hüser, I., Javed, U., Keßel, S., Lelieveld, J., Martinez, M., Meusel, H., Novelli, A., Phillips, G. J., Pozzer, A., Reiffs, A., Sander, R., Taraborrelli, D., Sauvage, C., Schuladen, J., Su, H., Williams, J., and Harder, H.: Oxidation processes in the eastern Mediterranean atmosphere: evidence from the modelling of HO_x measurements over Cyprus, Atmos. Chem. Phys., 18, 10825-10847, doi:10.5194/acp-18-10825-2018, 2018.

Mannschreck, K., Gilge, S., Plass-Duelmer, C., Fricke, W., and Berresheim, H.: Assessment of the applicability of NO-NO_2-O_3 photostationary state to long-term measurements at the Hohenpeissenberg GAW Station, Germany, Atmos. Chem. Phys., 4, 1265-1277, doi:10.5194/acp-4-1265-2004, 2004.

Mao, J., Ren, X., Chen, S., Brune, W. H., Chen, Z., Martinez, M., Harder, H., Lefer, B., Rappenglück, B., Flynn, J., Leuchner, M.: Atmospheric oxidation capacity in the summer of Houston 2006: Comparison with summer measurements in the metropolitan studies, Atmos. Environ., 44, 4107-4115, doi:10.1016/j.atmosenv.2009.01.013, 2009.

Martin R., Fiore, A., Van Donkelaar, A. 2004: Space-based diagnosis of surface ozone sensitivity to anthropogogenic emissions, Geophys. Res. Lett., 31, L06120, doi:10.1029/2004GL019416, 2004.

Martinez, M., Harder, H., Kubistin, D., Rudolf, M., Bozem, H., Eerdekens, G., Fischer, H., Klüpfel, T., Gurk, C., Königstedt, R., Parchatka, U., Schiller, C. L., Stickler, A., Williams, J., and Lelieveld, J.: Hydroxyl radicals in the tropical troposphere over the Suriname rainforest: airborne measurements, Atmos. Chem. Phys., 10, 3759-3773, doi: 10.5194/acp-10-3759-2010, 2010.

Mazzuca G. M., Ren, X., Loughner, C. P., Estes, M., Crawford, J. H., Pickering, K. E., Weinheimer, A. J., and Dickerson, R. R.: Ozone production and its sensitivity to NOx and VOCs: results from the DISCOVER-AQ field experiment, Houston 2013, Atmos. Chem. Phys., 16, 14463-14474, doi:10.5194/acp-16-14463-2016, 2016.

Meusel, H., Kuhn, U., Reiffs, A., Mallik, C., Harder, H., Martinez, M., Schuladen, J., Bohn, B., Parchatka, U., Crowley, J. N., Fischer, H., Tomsche, L., Novelli, A., Hoffmann, T., Janssen, R. H. H., Hartogensis, O., Pikridas, M., Vrekoussis, M., Bourtsoukidis, E., Weber, B., Lelieveld, J., Williams, J., Pöschl, U., Cheng, Y., and Su, H.: Daytime formation of nitrous acid at a coastal remote site in Cyprus indicating a common ground source of atmospheric HONO and NO, Atmos. Chem. Phys., 16, 14475-14493, doi:10.5194/acp-16-14475-2016, 2016.

Miyazaki, K., Eskes, H., Sudo, K., Folkert Boersma, K., Bowman, K., and Kanaya, Y.: Decadal changes in global surface NO_x emissions from multi-constituent satellite data assimilation, Atmos. Chem. Phys., 17, 807-837, doi:10:5194/acp-17-807-2017, 2017.

Monks, P. S., Archibald, A. T., Colette, A., Cooper, O. Coyle, M., Derwent, R., Fowler, D., Granier, C., Law, K. S., Mills, G. E., Stevenson, D. S., Tarasova, O., Thouret, V., von Schneidemesser, E., Sommariva, R., Wild, O., Williams, M. L.: Tropospheric ozone and its precursors from the urban to the global scale from air quality to short-lived climate forcer, Atmos. Chem. Phys., 15, 8889-8973, doi:10.5194/acp-15-8889-2015, 2015.

Nakamura, K., Kondo, Y., Chen, G., Crawford, J. H., Takegawa, N., Koike, M., Kita, K., Miyazaki, Y., Shetter, R. E., Lefer, B. L., Avery, M., and Matsumoto J.: Measurement of NO_2 by the photolysis conversion technique during the Transport and Chemical Evolution Over the Pacific (TRACE-P) campaign, J. Geophys. Res., 108, D24, 4752, doi:10.1029/2003JD003712, 2003.

Parrish, D. D., Trainer, M., Williams, E. J., Fahey D. W., Hübler, G., Eubank, C. S., Liu S. C., Murphy, P. C., Albritton, D. L., Fehsenfeld, F. C.: Measurements of the NO_x-O_3-photostationary steady state at Niwot Ridge, Colorado, J. Geophys. Res., 91,5361-5370, doi:10.1029/JD091iD05p05361, 1986.

Pollack, I. B., Lerner, B. M., Ryerson, T. B.: Evaluation of ultraviolet light-emitting diodes for detection of atmospheric NO_2 by photolysis – chemiluminescence, J. Atmos. Chem., 65, 111-125, doi:10.1007/s10874-011-9184-3, 2011.

Pfannerstill, E. Y., Wang, N., Edtbauer, A., Bourtsoukidis, E., Crowley, J. N., Dienhart, D., Eger, P. G., Ernle, L., Fischer, H., Hottmann, B., Paris, J.-D., Stönner, C., Tadic, I., Walter, D., Lelieveld, J., Williams, J.: Shipborne measurements of total OH reactivity around the Arabian Peninsula and its role in ozone chemistry, Atmos. Chem. Phys., 19, 11501-11523, doi:10.5194/acp-19-11501-2019, 2019.

Reed, C., Evans, M. J., Di Carlo, P., Lee, J. D., and Carpenter, L. J.: Interferences in photolytic NO_2 measurements: explanation for an apparent missing oxidant?, Atmos. Chem. Phys., 16, 4707-4724, doi:10.5194/acp-16-4707-2016, 2016.

Regelin, E., Harder, H., Martinez, M., Kubistin, D., Tatum Ernest, C., Bozem, H., Klippel, T., Hosaynali Beygi, Z., Fischer, H., Sander, R., Jöckel, P., Königstedt, R., and Lelieveld, J.: HO_x measurements in the summertime upper troposphere over Europe: a comparison of observations to a box model and a 3-D model, Atmos. Chem. Phys. Phys., 13, 10703-10720, doi:10.5194/acp-13-10703-2013, 2013.

Ren, X., van Duin, D., Cazorla, M., Chen, S., Mao, J., Zhang, L., Brune, W. H., Flynn, J. H., Grossberg, N., Lefer, B. L., Rappenglück, B., Wong, K. W., Tsai, C., Stutz, J., Dibb, J. E., Jobson, B. T., Luke, W. T., and Kelley, P.: Atmospheric oxidation chemistry and ozone production: Results from SHARP 2009 in Houston, Texas, J. Geophys. Res., 118, 5570-5780, doi:10.1002/jgrd.50342, 2013.

Roeckner, E., Brokopf, R., Esch, M., Giorgetta, M., Hagemann, S., Kornblueh, L., Manzini, E., Schlese, U., and Schulzweida, U.: Sensitivity of Simulated Climate to Horizontal and Vertical Resolution in the ECHAM5 Atmosphere Model, J. Climate, 19, 3771-3791, doi:10.1175/JCLI3824.1, 2006.

Ryerson, T. B., Williams, E. J., and Fehsenfeld, F. C.: An efficient photolysis system for fast-response NO_2 measurements, J. Geophys. Res., 105, D21, 26447-26461, doi:10.1029/2000JD900389, 2000.

Sander, R., Baumgartner, A., Cabrera-Perez, D., Frank, F., Gromov, S., Grooß, J.-U., Harder, H., Huijnen, V., Jöckel, P., Karydis, V. A., Niemeyer, K. E., Pozzer, A., Riede, H., Schultz, M. G., Taraborrelli, D., and Tauer, S.: The community atmospheric chemistry box model CAABA/MECCA-4.0, Geosci. Model Dev., 12, 1365-1385, doi: 10.5194/gmd-12-1365-2019, 2019.

Sobanski, N., Schuladen, J., Schuster, G., Lelieveld, J., and Crowley, J. N.: A five-channel cavity ring-down spectrometer for the detection of NO_2, NO_3, N_2O_5, total peroxy nitrates and total alkyl nitrates, Atmos. Meas. Techn., 9, 5103-5118, doi:10.5194/amt-9-5103-2016, 2016.

Sillman, S., Al-Wali, K., Marsik, F. J., Nowacki, P., Samson, P. J., Rodgers, M. O., Garland, L. J., Martinez, J. E., Stoneking, C., Imhoff, R., Lee, J. H., Newman, L., Weinstein-Lloyd, J., and Aneja, V.: Photochemistry of ozone formation in Atlanta, GA - models and measurements, Atmos. Environ., 29, 21, 3055-3066., doi:10.1016/1352-2310(95)00217-M, 1995.

Thornton, J. A., Wooldridge, P. J., Cohen, R. C., Martinez, M., Harder, H., Brune, W. H., Williams, E. J., Roberts, J. M., Fehsenfeld, F. C., Hall, S. R., Shetter, R. E., Wert, B. P., and Fried, A.: Ozone production rates as a function of NO_x abundances and HO_x production rates in the Nashville urban plume, J. Geophys. Res., 107, D12, doi:10.1029/2001JD000932, 2002.

Tuzson, B., Zeyer, K., Steinbacher, M., McManus, J. B., Nelson, D. D., Zahniser, M. S., and Emmenegger, L.: Selective measurements of NO, NO_2 and NO_y in the free troposphere using quantum cascade laser spectroscopy, Atmos. Meas. Tech., 6, 927-936, doi:10/5194/amt-6-927-2013, 2013.

Viallon, J., Lee, S., Moussay, P., Tworek, K., Petersen, M., and Wielgosz, R. I.: Accurate measurements of ozone absorption cross-sections in the Hartley band, Atmos. Meas. Tech., 8, 1245-1257, doi:10.5194/amt-8-1245-2015, 2015.

Velchev, K., Cavalli, F., Hjorth, J., Vignati, E., Dentener, F., and Raes, F.: Ozone over the Western Mediterranean Sea – results from two years of shipborne measurements, Atmos. Chem. Phys., 11, 675-688, doi:10.5194/acp-11-675-2011, 2011.

Zhou, W., Cohan, D. S., and Henderson, B. H.: Slower ozone production in Houston, Texas following emission reductions: evidence from Texas Air Quality Studies in 2000 and 2006, Atmos. Chem. Phys., 14, 2777-2788, doi:10.5194/acp-14-2777-2014, 2014.

Supplement of

Net ozone production and its relationship to NO_x and VOCs in the marine boundary layer around the Arabian Peninsula

Ivan Tadic[1], John N. Crowley[1], Dirk Dienhart[1], Philipp Eger[1], Hartwig Harder[1], Bettina Hottmann[1], Monica Martinez[1], Uwe Parchatka[1], Jean-Daniel Paris[2], Andrea Pozzer[1,4], Roland Rohloff[1], Jan Schuladen[1], Justin Shenolikar[1], Sebastian Tauer[1], Jos Lelieveld[1,3], and Horst Fischer[1]

[1]Atmospheric Chemistry Department, Max Planck Institute for Chemistry, Mainz, Germany
[2]Laboratoire des Sciences du Climat et de l'Environnement, LSCE/IPSL, CEA-CNRS-UVSQ, Université Paris-Saclay, Gif-sur-Yvette, France
[3]Energy, Environment and Water Research Center, The Cyprus Institute, Nicosia, Cyprus
[4]International Centre for Theoretical Physics, Trieste, Italy

Correspondence to: Ivan Tadic (i.tadic@mpic.de)

Figure S1 shows a day to day calculation of the correction factor to scale the fractional noontime integral to a diurnal value. An average ± standard deviation of (46.1 ± 2.8) % of the diurnal integral within ± 2h around noontime was estimated.

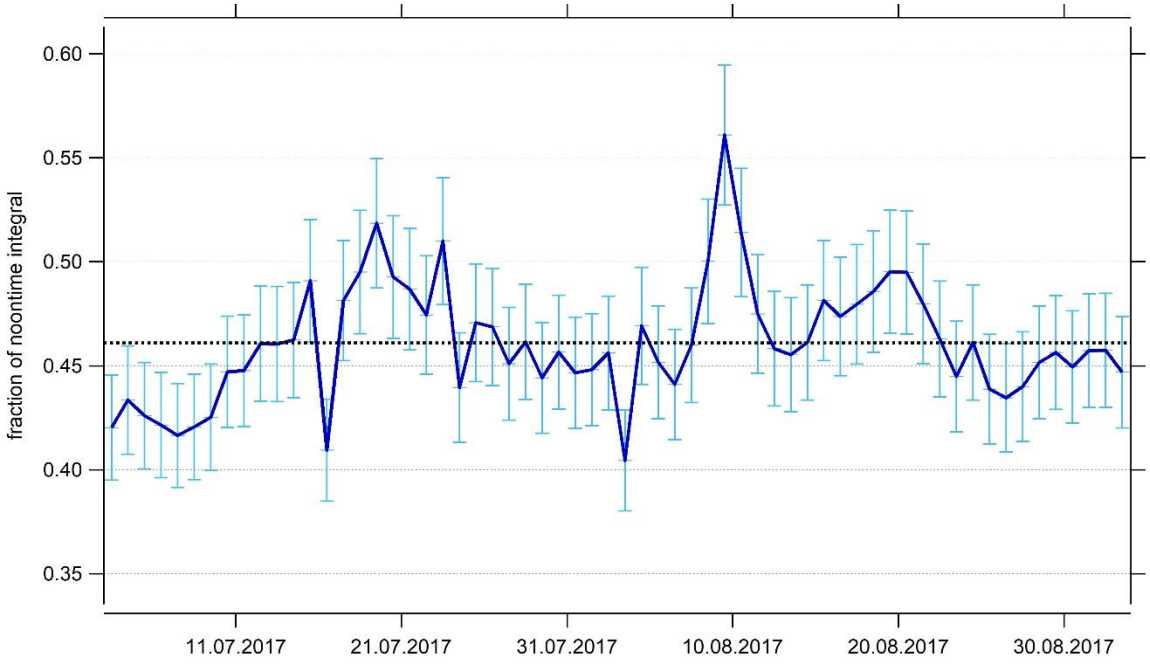

Figure S1: Ratio of the noontime actinic flux (± 2h around noon) with regard to the total actinic flux $j(NO_2)$ of that particular day. Dashed line represents the campaign average of (46.1 ± 2.8) %. The errors bars are represented by the relative uncertainty (6 %) of the campaign average.

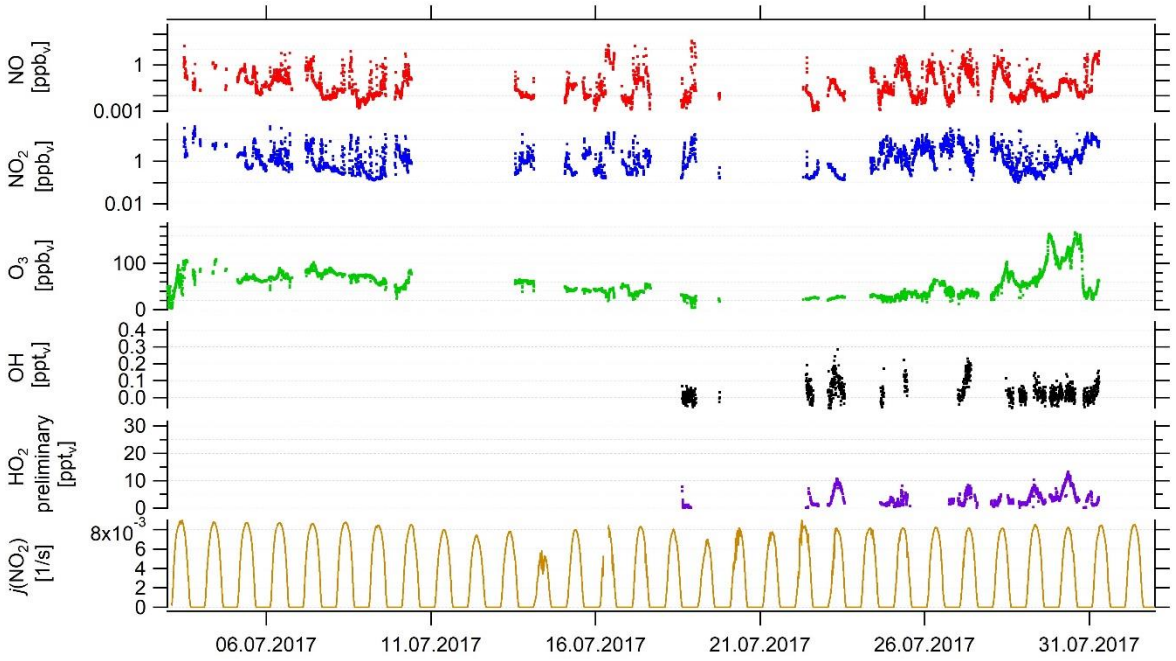

845

Figure S2: Timeline of NO, NO_2 (both CLD), O_3, OH, HO_2 preliminary and $j(NO_2)$ data during the first leg. See Table ST2 for additional information on the ship cruise. Note that HO_2 data are preliminary.

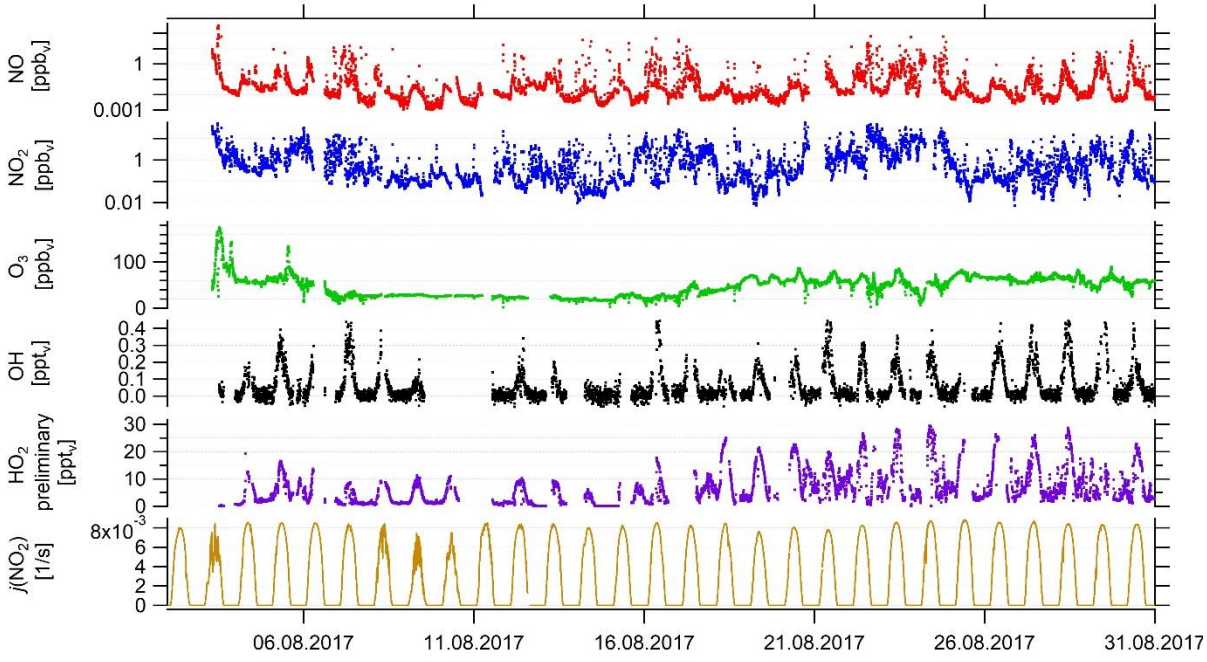

850 **Figure S3: Timeline of NO, NO_2 (both CLD), O_3, OH, HO_2 preliminary and $j(NO_2)$ data during the second leg. See Table ST2 for additional information on the ship cruise. Note that HO_2 data are preliminary.**

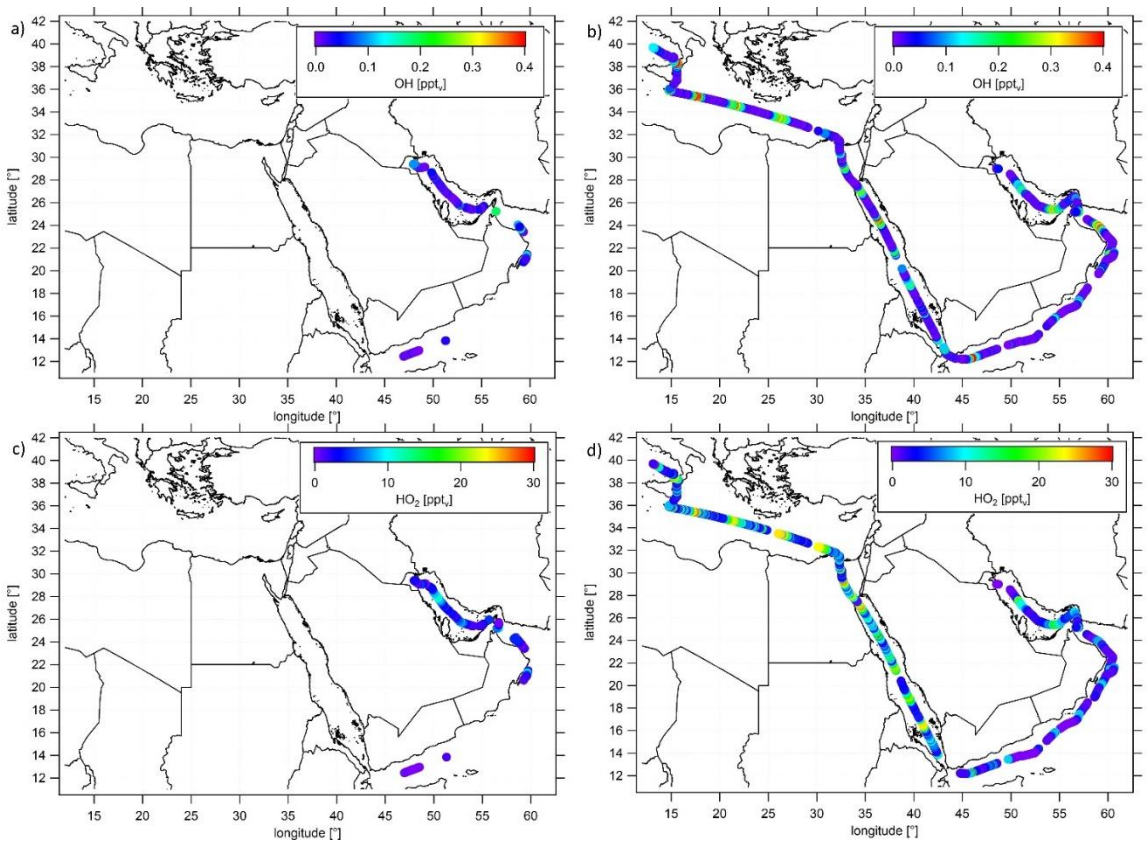

Figure S4: Ship cruises with color-scaled OH mixing ratios a) during the first and b) the second leg and color-scaled HO_2 mixing ratios (preliminary) c) during the first and d) the second leg. Note that OH and preliminary HO_2 data have been filtered for own stack contamination.

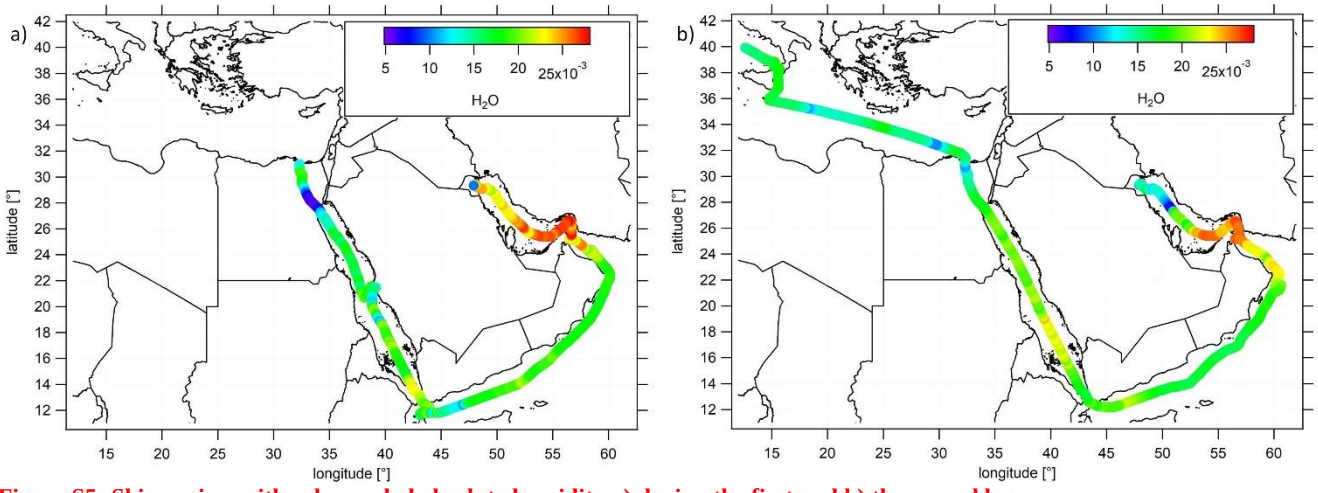

Figure S5: Ship cruises with color-scaled absolute humidity a) during the first and b) the second leg.

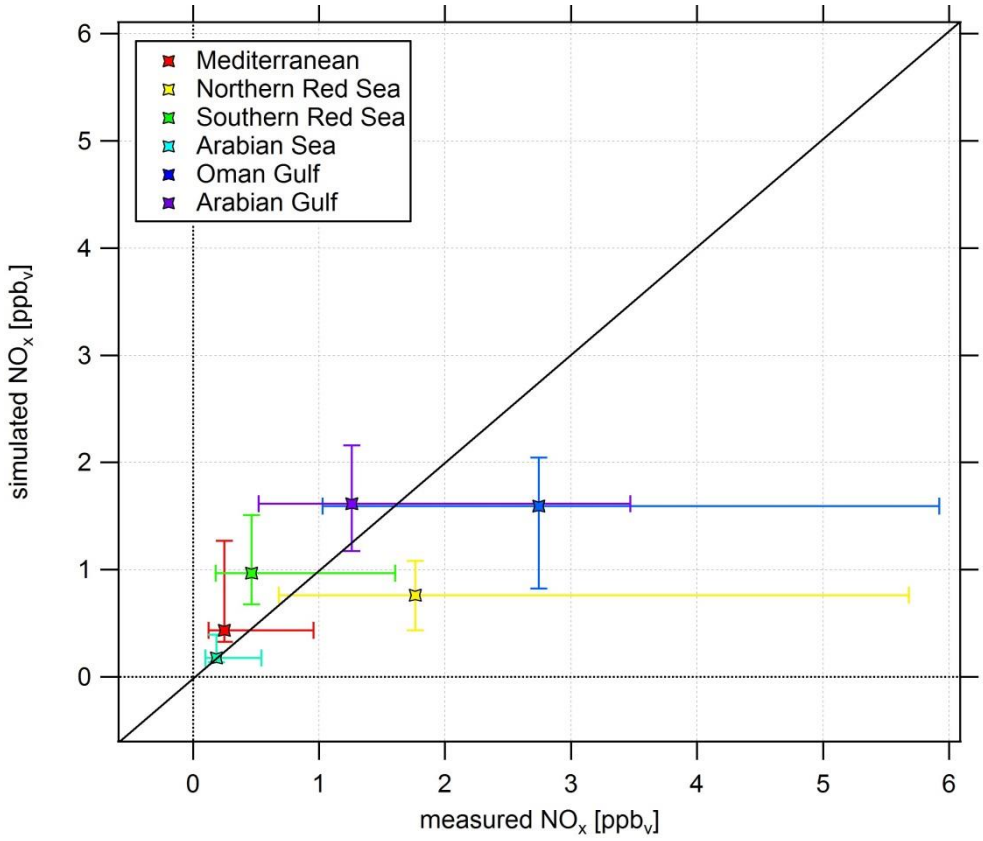

Figure S6: Scatterplot of simulated and measured regional NO_x median in ppb_v. 1:1 line added for orientation. The error bars represent the 25-75-percentile variation.

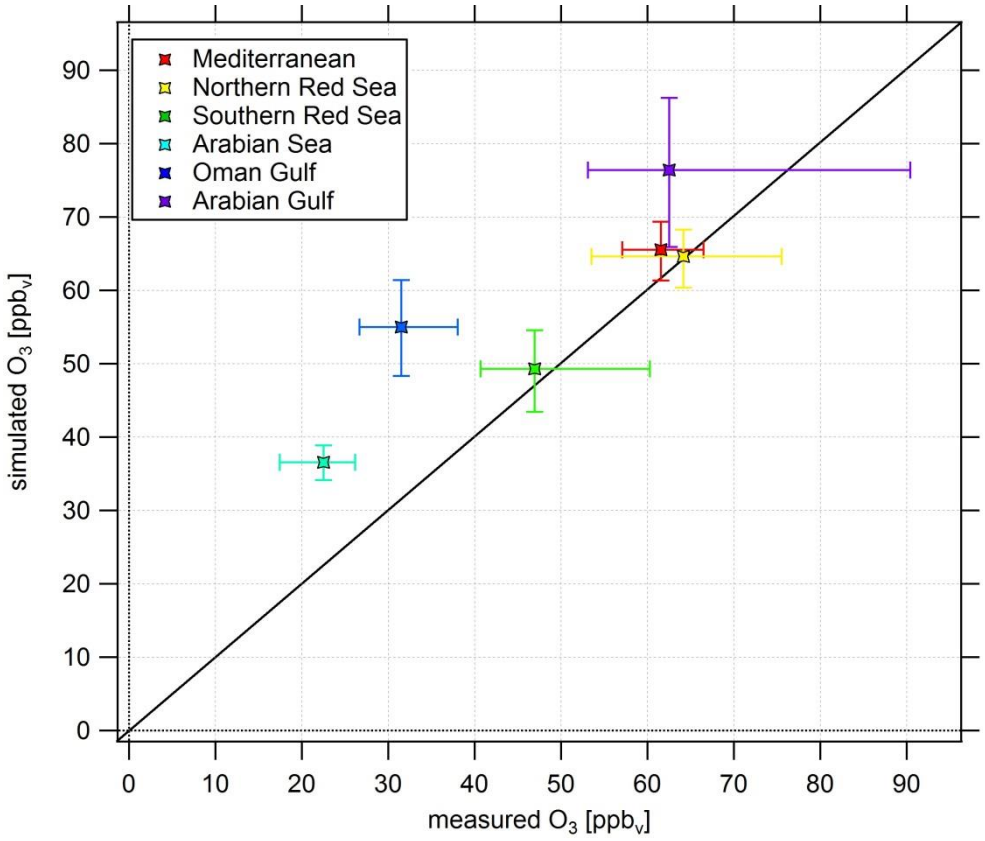

865 **Figure S7: Scatterplot of simulated and measured regional O_3 median in ppb_v. 1:1 line added for orientation. The error bars represent the 25-75-percentile variation.**

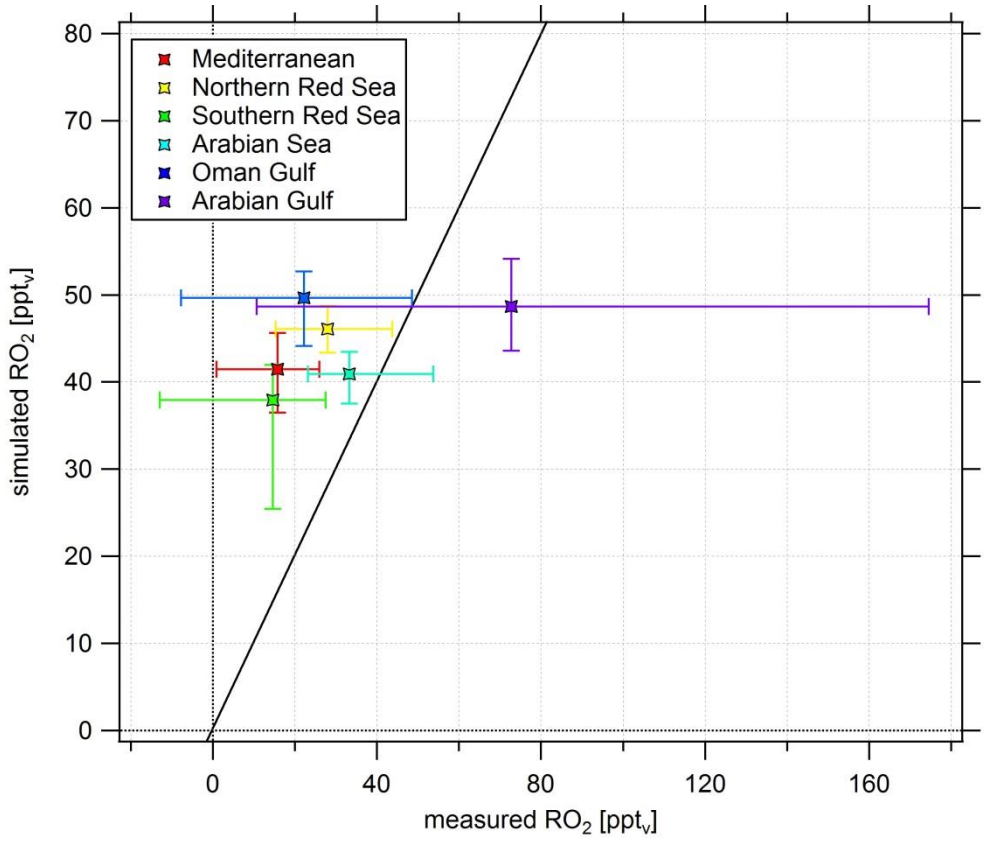

Figure S8: Scatterplot of simulated regional RO_2 median and regional RO_2 median estimated based on measured tracer data in ppt_v. 1:1 line added for orientation. The error bars represent the 25-75-percentile variation.

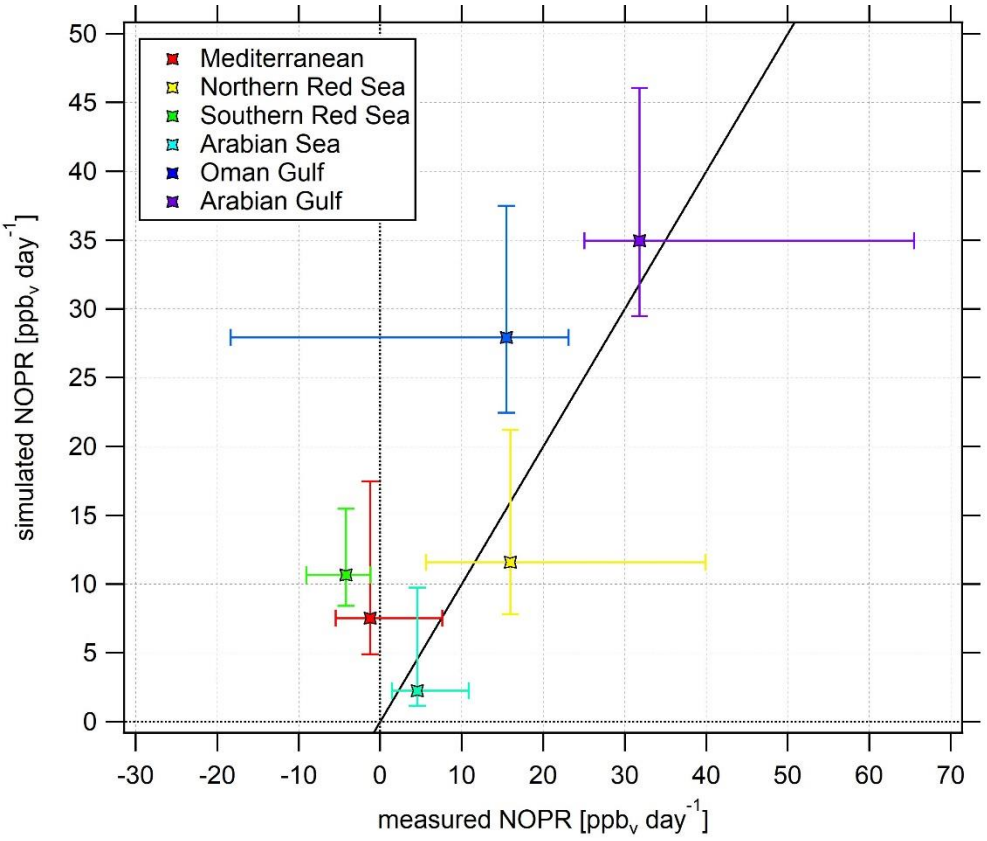

870

Figure S9: Scatterplot of median NOPR in ppb$_v$ day^{-1} estimated based on simulated and measured tracer data. 1:1 line added for orientation. The error bars represent the 25-75-percentile variation.

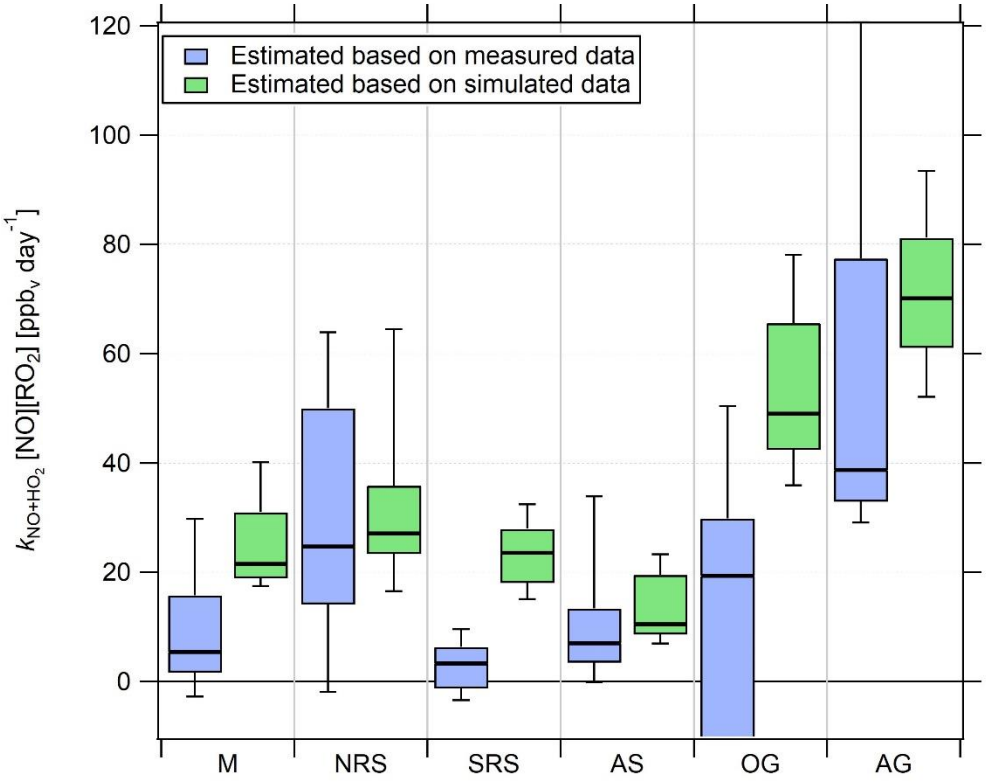

875

Figure S10: Comparison of the regional, absolute contribution of $k_{NO+HO_2}[NO][RO_2]$ to NOPR in the six different regions investigated during AQABA. The horizontal black bar indicates the median value, the box the 25- and 75-percentiles and the whiskers the 10- and 90-percentiles.

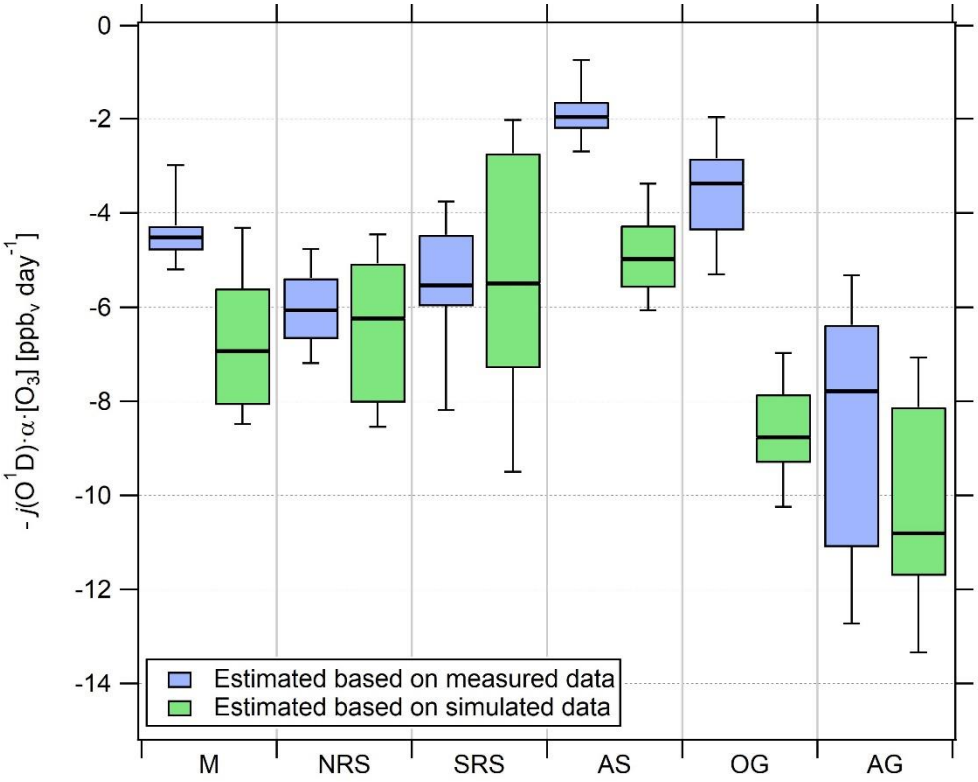

880 **Figure S11: Comparison of the regional, absolute contribution of $-j(O^1D) \cdot \alpha \cdot [O_3]$ to NOPR in the six different regions investigated during AQABA. The horizontal black bar indicates the median value, the box the 25- and 75-percentiles and the whiskers the 10- and 90-percentiles.**

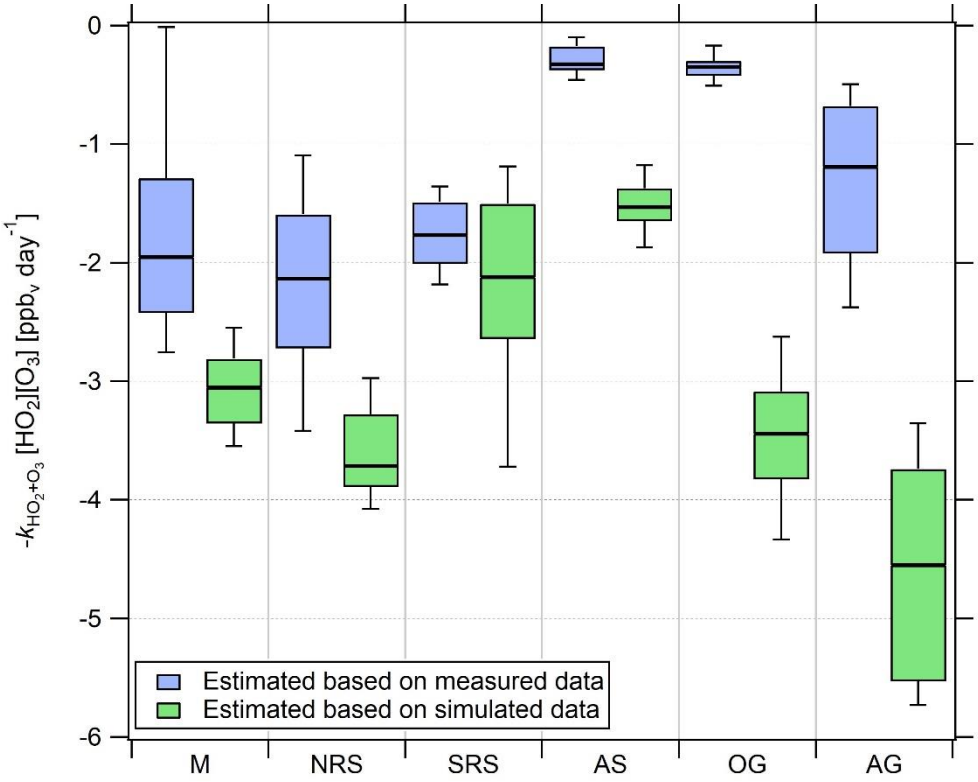

885

Figure S12: Comparison of the regional, absolute contribution of $-k_{HO_2+O_3}[HO_2][O_3]$ to NOPR in the six different regions investigated during AQABA. The horizontal black bar indicates the median value, the box the 25- and 75-percentiles and the whiskers the 10- and 90-percentiles.

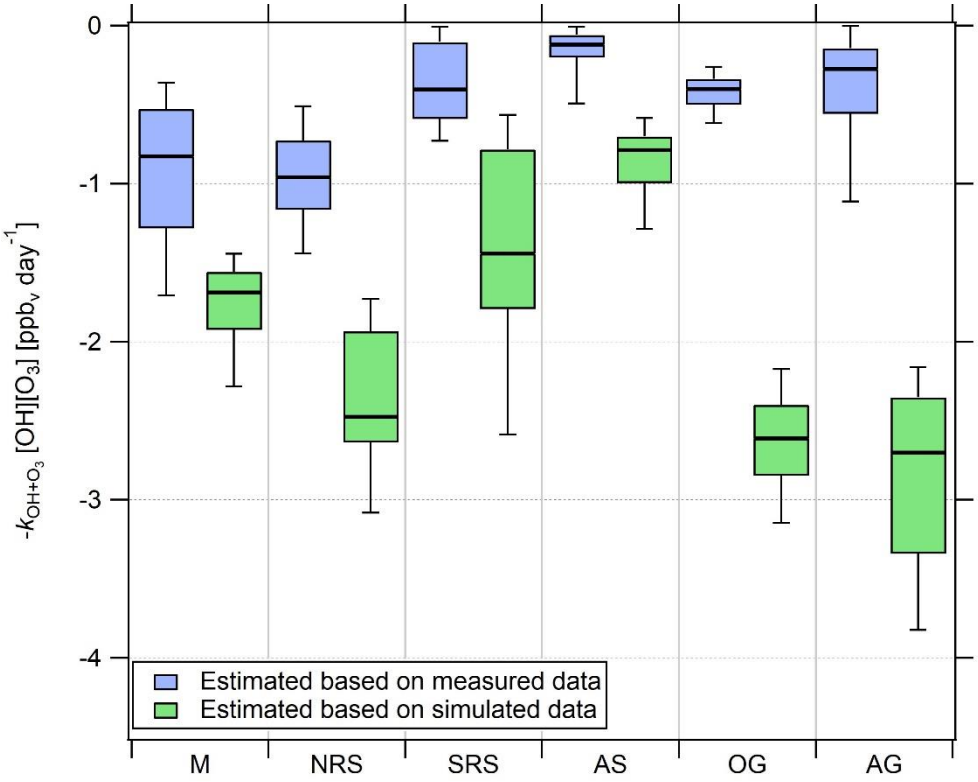

890

Figure S13: Comparison of the regional, absolute contribution of $-k_{OH+O_3}[OH][O_3]$ to NOPR in the six different regions investigated during AQABA. The horizontal black bar indicates the median value, the box the 25- and 75-percentiles and the whiskers the 10- and 90-percentiles.

Table ST1: Range of latitudinal and longitudinal coordinates and dates during both legs of the different regions.

region (abbreviation)	latitudinal range	longitudinal range	Date (1st leg)	Date (2nd leg)
Mediterranean (M)	31.810° N- 39.923° N	12.620° E- 31.850° E	---	25.08.2017 – 31.08.2017
Northern Red Sea (NRS)	23.343° N- 30.986° N	32.305° E- 37.085° E	03.07.2017 – 08.07.2017	21.08.2017 – 24.08.2017
Southern Red Sea (SRS)	12.672° N- 22.494° N	37.411° E- 43.327° E	09.07.2017 – 16.07.2017	17.08.2017 – 20.08.2017
Arabian Sea (AS)	11.797° N- 22.782° N	44.035° E- 60.636° E	18.07.2017 – 24.07.2017	07.08.2017 – 16.08.2017
Oman Gulf (OG)	23.050° N- 25.622° N	56.492° E- 59.913° E	24.07.2017 – 27.07.2017	05.08.2017 – 07.08.2017
Arabian Gulf (AG)	25.396° N- 29.425° N	47.920° E- 56.772° E	27.07.2017 – 31.07.2017	03.08.2017 – 05.08.2017

Table ST2: Overview of the time spent in the particular regions during AQABA. Red color indicates periods with KI at anchor that are not included in the data analysis. Data measured during bunkering at Fujairah City (06 August, 07:00-15:00 UTC) were also not included in the analysis.

Date	Region	Date	Region
03.07.2017	Northern Red Sea	**02.08.2017**	Kuwait port
04.07.2017	Northern Red Sea	**03.08.2017**	Kuwait port/Arabian Gulf
05.07.2017	Northern Red Sea	**04.08.2017**	Arabian Gulf
06.07.2017	Northern Red Sea	**05.08.2017**	Arabian Gulf/Oman Gulf
07.07.2017	Northern Red Sea	**06.08.2017**	Oman Gulf
08.07.2017	Northern Red Sea	**07.08.2017**	Oman Gulf/Arabian Sea
09.07.2017	Southern Red Sea	**08.08.2017**	Arabian Sea
10.07.2017	Southern Red Sea	**09.08.2017**	Arabian Sea
11.07.2017	Southern Red Sea/Jeddah port	**10.08.2017**	Arabian Sea
12.07.2017	Jeddah port	**11.08.2017**	Arabian Sea
13.07.2017	Jeddah port/Southern Red Sea	**12.08.2017**	Arabian Sea
14.07.2017	Southern Red Sea	**13.08.2017**	Arabian Sea
15.07.2017	Southern Red Sea	**14.08.2017**	Arabian Sea
16.07.2017	Southern Red Sea	**15.08.2017**	Arabian Sea
17.07.2017	Djibouti port	**16.08.2017**	Arabian Sea
18.07.2017	Arabian Sea	**17.08.2017**	Southern Red Sea
19.07.2017	Arabian Sea	**18.08.2017**	Southern Red Sea
20.07.2017	Arabian Sea	**19.08.2017**	Southern Red Sea
21.07.2017	Arabian Sea	**20.08.2017**	Southern Red Sea
22.07.2017	Arabian Sea	**21.08.2017**	Northern Red Sea
23.07.2017	Arabian Sea	**22.08.2017**	Northern Red Sea
24.07.2017	Arabian Sea/Oman Gulf	**23.08.2017**	Northern Red Sea
25.07.2017	Oman Gulf	**24.08.2017**	Northern Red Sea
26.07.2017	Oman Gulf	**25.08.2017**	Mediterranean
27.07.2017	Oman Gulf/Arabian Gulf	**26.08.2017**	Mediterranean
28.07.2017	Arabian Gulf	**27.08.2017**	Mediterranean
29.07.2017	Arabian Gulf	**28.08.2017**	Mediterranean
30.07.2017	Arabian Gulf	**29.08.2017**	Mediterranean
31.07.2017	Arabian Gulf/Kuwait port	**30.08.2017**	Mediterranean
01.08.2017	Kuwait port	**31.08.2017**	Mediterranean

900

Table ST3: Overview of measured NO_x (upper table) and measured O_3 (lower table) spatial volume mixing ratio average, standard deviation, 1st quantile, median, 3rd quantile (all in ppb_v) and number of considered data points.

NO_x (upper), O_3 (lower)	Mediterranean	Northern Red Sea	Southern Red Sea	Arabian Sea	Oman Gulf	Arabian Gulf
data points	1767	1694	1755	2656	1056	1539
average	1.24	4.69	1.62	0.95	4.16	3.65
stdev	3.34	7.9	3.7	3.15	4.33	9.24
1st quantile	0.12	0.68	0.18	0.10	1.03	0.52
median	**0.25**	**1.76**	**0.46**	**0.19**	**2.74**	**1.26**
3rd quantile	0.96	5.68	1.6	0.54	5.92	3.47
data points	2010	2717	2307	4130	1249	1809
average	**61.56**	**63.39**	**50.35**	**21.53**	**34.04**	**73.99**
stdev	8.25	18.45	12.96	6.8	11.27	35.68
1st quantile	57.05	53.51	40.68	17.45	26.66	53.08
median	**61.54**	**64.16**	**46.93**	**22.52**	**31.5**	**62.5**
3rd quantile	66.48	75.51	60.28	26.19	38.03	90.42

Table ST4: Overview of simulated NO_x (upper table) and simulated O_3 (lower table) spatial volume mixing ratio average, standard
905 **deviation, 1st quantile, median, 3rd quantile (all in ppb_v) and number of considered data points.**

NO_x (upper), O_3 (lower)	Mediterranean	Northern Red Sea	Southern Red Sea	Arabian Sea	Oman Gulf	Arabian Gulf
data points	2012	2719	2310	4464	1253	1810
average	0.84	1.27	1.13	0.31	1.88	1.91
stdev	0.75	1.97	0.62	0.29	1.47	1.37
1st quantile	0.33	0.43	0.67	0.14	0.82	1.17
median	**0.43**	**0.76**	**0.97**	**0.18**	**1.59**	**1.61**
3rd quantile	1.27	1.08	1.51	0.39	2.05	2.16
data points	2012	2719	2310	4464	1253	1810
average	**65.15**	**64.76**	**49.5**	**36.91**	**55**	**76.85**
stdev	4.99	7.7	7.21	3.87	9.94	12.8
1st quantile	61.35	60.34	43.47	34.12	48.37	65.88
median	**65.53**	**64.6**	**49.33**	**36.54**	**55.01**	**76.39**
3rd quantile	69.33	68.25	54.58	38.85	61.42	86.22

Table ST5: Overview of noontime RO_2 spatial volume mixing ratio average, standard deviation, 1st quantile, median, 3rd quantile (all in ppt_v) estimated based on measured tracer data. Number of considered data points added in the first line.

RO_2	Mediterranean	Northern Red Sea	Southern Red Sea	Arabian Sea	Oman Gulf	Arabian Gulf
data points	288	126	190	338	166	242
average	13	27	7	64	23	94
stdev	24	20	34	83	42	113
1st quantile	1	15	-13	23	-8	11
median	**16**	**28**	**15**	**33**	**22**	**73**
3rd quantile	26	44	27	54	49	176

Table ST6: Overview of simulated noontime RO_2 spatial volume mixing ratio average, standard deviation, 1st quantile, median, 3rd quantile (all in ppt_v). Number of considered data points added in the first line.

RO_2	Mediterranean	Northern Red Sea	Southern Red Sea	Arabian Sea	Oman Gulf	Arabian Gulf
data points	336	192	192	720	203	293
average	41	46	36	40	48	49
stdev	5	4	11	5	6	7
1st quantile	36	43	25	38	44	44
median	**41**	**46**	**38**	**41**	**50**	**49**
3rd quantile	46	49	42	43	53	54

Table ST7: Overview of NOPR average, standard deviation, 1st quantile, median, 3rd quantile (all in $ppb_v\ day^{-1}$) estimated based on measured tracer data. Number of considered data points added in the first line.

NOPR	Mediterranean	Northern Red Sea	Southern Red Sea	Arabian Sea	Oman Gulf	Arabian Gulf
data points	148	114	89	187	84	111
average	-3	16	-5	-67	-105	-24
stdev	43	39	12	576	362	449
1st quantile	-5	6	-9	1	-18	25
median	**-1**	**16**	**-4**	**5**	**16**	**32**
3rd quantile	8	40	-1	11	23	65

Table ST8: Overview of NOPR average, standard deviation, 1st quantile, median, 3rd quantile (all in ppb_v day^{-1}) estimated based on simulated tracer data. Number of considered data points added in the first line.

NOPR	Mediterranean	Northern Red Sea	Southern Red Sea	Arabian Sea	Oman Gulf	Arabian Gulf
data points	336	192	192	720	203	293
average	11	16	12	5	30	38
stdev	8	12	6	6	11	10
1st quantile	5	8	8	1	22	30
median	**8**	**12**	**11**	**2**	**28**	**35**
3rd quantile	17	21	15	10	37	46

920

Table ST9: Overview of measured HCHO/NO_2-ratio average, standard deviation, 1st quantile, median, 3rd quantile and number of considered data points.

Ratio	Mediterranean	Northern Red Sea	Southern Red Sea	Arabian Sea	Oman Gulf	Arabian Gulf
data points	203	79	48	252	108	122
average	5.4	1.5	8.5	11.1	2.7	9
stdev	4.7	0.7	6.5	8.9	2.1	6.4
1st quantile	1.3	0.8	4.4	2.3	1	2.5
median	**5**	**1.4**	**7.7**	**9.4**	**2.2**	**9.3**
3rd quantile	7.4	2.1	9.8	16.1	3.6	12.7

925 **Table ST10: List of included peroxy radicals (with less than four carbon atoms) for the reaction with NO as recommended by Sander et al. (2019).**

Species
HO_2
CH_3O_2
C_2H_5O2
$C_2H_5CO_3$
CH_3CO_3
C3DIALO2 ($C_3H_3O_4$)
CH_3CHOHO_2
$CH_3COCH_2O_2$
CH_3COCO_3
$CHOCOCH_2O_2$
$CO_2H_3CO_3$
$HCOCH_2CO_3$
$HCOCH_2O_2$
$HCOCO_3$
$HCOCOHCO_3$
$HOC_2H_4CO_3$
$HOCH_2CH_2O_2$
$HOCH_2CO_3$
$HOCH_2COCH_2O_2$
$HOCH_2O_2$
$CH_3CHO_2CH_2OH$
IC3H7O2 (isopropylperoxy radical)
NC3H7O2 (propylperoxy radical)
$NCCH_2O_2$
$NO_3CH_2CO_3$
$CH_3CHO_2CH_2ONO_2$